Stratigraphic architecture and characterization of a Neoproterozoic continental slope system, Windermere Supergroup, east-central British Columbia, Canada

Simona Ruso

A thesis submitted to the University of Ottawa
in partial fulfillment of the requirements for the M.Sc. degree in Earth Science

Faculty of Science
University of Ottawa

Abstract

At the Castle Creek study area, exceptionally well exposed strata of the Isaac Formation (Neoproterozoic Windermere Supergroup) crop out over a strike length of 4 km. This ~ 1 km-thick succession of continental slope deposits consist of six channel complexes (ICC1-ICC6) composed of three main architectural elements: mass transport deposits (MTDs), channel, and overbank deposits. Together, these elements stack in a repeating and systematic pattern that illustrates periodic forcing on the system related to the combined effect of long- and short-term changes in relative sea level that controlled the development of the continental shelf, and ultimately, the make up of the sediment resedimented into the deep-marine system. Understanding these stacking patterns in ancient slope systems and the conditions under which they formed, is important for assessing regional and potentially global changes in ancient climate and eustasy.

Résumé

Dans la région d’étude de Castle Creek, des strates exceptionnellement bien exposées de la formation Isaac (supergroup néoprotérozoïque de Windermere) s’étendent sur 4 km parallèlement à l’orientation des strates. Cette succession de dépôts de pente continentale d’environ 1 km d’épaisseur est constituée de six complexes de chenaux (ICC1-ICC6) composes de trois éléments architecturaux principaux: des dépôts de transport de masse (MTD), des chenaux et des dépôts sur berge. Ensemble, ces éléments s’empilent selon un modèle répétitif et systématique qui illustre le forçage périodique du système lié à l’effet combine des changements à long et à court terme du niveau relative de la mer qui ont contrôlé le développement du plateau continental et, en fin de compte, la composition des sediments resédimentés dans le système marin profond. La comprehension de ces modèles d'empilement dans les anciens systems de pente et des conditions dans lesquelles ils se sont formés, est important pour évaluer les changements régionaux et potentiellement globaux dans le climate et l'eustasie anciens.

Extended Abstract

The deep sea is host to the largest depositional elements on earth, termed turbidite systems, that are built up of sediment transported down the continental slope principally by turbidity currents and mass wasting processes. However, the inaccessibility (i.e., extreme water depths), unpredictable timing, and destructive nature of these processes in modern systems has resulted in a poorly developed understanding of internal stratigraphy and how these systems change in time and space. To bridge this gap, ancient turbidite deposits provide valuable insight into the formative processes and stratal architectures that shape these systems. At the Castle Creek study area in the Cariboo Mountains of western Canada, deep-marine rocks of the Neoproterozoic Windermere Supergroup (WSG) are exceptionally well-exposed and comprise an upward-shoaling succession of basin floor terminal fans of the Kaza Group and leveed slope channels of the Isaac Formation. Strata described here are part of the Isaac Formation and show a systematic and repetitive stacking of its composite architectural elements. Detailed analysis of lithology, geochemistry, and stratigraphic architecture aims to identify relationships between architectural elements and the factor(s) that may be forcing these systematic changes in stratigraphy.

Exposed in the Hill Section outcrop are continental slope deposits of the Isaac Formation that exhibit a stacking pattern comprising three main architectural elements: mass transport deposits (MTDs), channels, and overbank deposits. The occurrence of MTDs provides insight into the state of gravitational stability on the slope at the time of deposition, which everywhere

are overlain by channel elements that stratigraphically upward show a change from aggradationally filled to laterally accreting channel fills. Overbank deposits crop out adjacent to or overlie channel fills and are exceptionally well-exposed, allowing for detailed description of both lateral and vertical trends in lithology. The consistent upward change from MTD to aggradational to laterally accreting channel fills, and adjacent levee deposits, reflects systematic and recurring changes in slope stability, sediment supply, and relative sea level, which collectively are integral to understanding the temporal evolution of the system.

Chemostratigraphic units were identified based on trends in the abundance of elemental proxies, namely strontium (Sr) for carbonate and zirconium (Zr) for siliciclastic sediment, which then were used to subdivide the stratigraphic column into systems tracts. The Transgressive Systems Tract (TST) is typically characterized by increasing Sr and decreasing Zr, interpreted to represent growth and expansion of the shelf carbonate factory and reduced siliciclastic input from the hinterland. During the ensuing Highstand, Falling Stage and into the Lowstand Systems Tracts (HST, FSST and LST, respectively), Sr decreases whereas Zr increases, which most likely reflects the progressive shut-down of the carbonate factory and increased siliciclastic sediment input from the hinterland. These elemental trends combined with changes in architectural elements and their stacking pattern are interpreted to be related to changes in relative sea level. MTDs with common stromatolite and oolite fragments, in addition to carbonate cemented sandstone and mudstone clasts, are associated with highstand and falling relative sea level and indicate a period of gravitational instability on the upper slope and outer shelf. During the following LST, aggradational channel complexes dominate as sediment provided directly from the hinterland formed density-stratified turbidity currents and channels that filled from the bottom up. However, as relative sea level begins to rise during the TST, and transported sediment becomes dominated by coarse palimpsest and relict sediment sourced from the shelf, causing turbidity currents to become less stratified and sediment to be deposited on the inner bend margin of laterally migrating channels.

The systematic and recurring occurrence of MTDs overlain by aggradationally filled channels overlain by laterally accreting slope channels, in addition to consistent trends in elemental composition, illustrates periodic forcing on the system that most likely is related to long-term changes in relative sea level and sediment supply to the deep sea. Understanding these systematic patterns is important for assessing regional and potentially global changes in climate and eustasy, and how those changes are manifest in the deep-marine sedimentary record.

Acknowledgements

First and foremost, I'd like to thank my supervisor, Bill. Thank you for giving me the opportunity to work on such a cool project with a great group of people, past and present. I am so thankful to have experienced Castle Creek, horseflies and all. Your enthusiasm for all things geology is inspiring and I hope to carry that through the rest of my academic journey and beyond.

Thank you, Don Cummings and Quentin Gall, for your insight and feedback on this thesis and for serving on my defense committee. I hope you enjoy yet another Windermere project.

Thank you Lilianne Dagenais, for your tireless work in the X-Ray lab. Alex and Rae, we had so many samples to crush and so many plots to make, thank you for not making me do it on my own. I would still be in the crushing lab.

To Celeste, Patty, Jessie, Liam, Mary, and Gillian, for an amazing field season. I had the time of my life and learned so much from all of you. From figuring out how to dig the optimal toilet to hunting for goats at Goat Peak, it was a field season I will never forget. Code Yellow!!

To the rest of the Windy crew: (Celeste and Patty, again) Jag, Omar, Alex, and Mike, your knowledge and feedback has really helped me make this thesis what it is (…hopefully a good one). Thank you to the Windermere Consortium, NSERC, OXY Petroleum, Apache, and Husky Energy for your continued and generous financial support.

Storm, for your endless support while I dealt with moving to a totally new city, making new friends, and imposter syndrome. Thank you.

My best friends, family, and cugini back home, I'd go crazy without you guys. Thank you for always keeping a place for me every time I leave home.

And finally, most importantly, to my parents, Rob and Lisa. None of this would be possible without your unconditional love and support (both emotional and financial). I owe my past, present, and future to you two. No words can really encompass the amount of thanks I want to give you guys, but I'll say it anyway. Thank you. Grazie mille. Vi amo sempre.

Table of Contents

List of Figures

List of Tables

List of Abbreviations

WSG – Windermere Supergroup

CC – Castle Creek study area

CCSED – Castle Creek Southeast Drainage

CCS – Castle Creek South

CCN – Castle Creek North

CCHS- Castle Creek Hill Section

FIC – First Isaac Carbonate

cm – centimetre

dm – decimetre

m – metre

Dm – decametre

km – kilometre

MTD – Mass Transport Deposit

F1 – Facies 1: Structureless Sandstone

F2 – Facies 2: Structured sandstone to mudstone

F3 – Facies 3: Conglomerate

F4 – Facies 4: Deformed Bedded Deposit

T_a –A division of Bouma turbidite sequence

T_b – B division of Bouma turbidite sequence

T_c – C division of Bouma turbidite sequence

T_d – D division of Bouma turbidite sequence

T_e – E division of Bouma turbidite sequence

LAD – Lateral Accretion Deposit

ICC1 – Isaac Channel Complex 1

LC – Isaac Channel Complex 1 Lower Channel Unit

UC1 – Isaac Channel Complex 1 Upper Channel Unit 1

UC2 – Isaac Channel Complex 1 Upper Channel Unit 2

ICC2 – Isaac Channel Complex 2

ICC3 – Isaac Channel Complex Set 3

IC3L-C1 to C4 – Isaac Channel Complex Set 3 Lower Complex Channel Units 1 to 4

IC3U-C1 to C2 – Isaac Channel Complex Set 3 Upper Complex Channel Units 1 to 2

ICC4 – Isaac Channel Complex Set 4

IC4.1 to 4.4 – Isaac Channel Complex Set 4 Complexes 1 to 4

ICC4B – Isaac Channel Complex 4B

ICC5 – Isaac Channel Complex Set 5

IC5.1 to 5.4 – Isaac Channel Complex Set 5 Complexes 1 to 4

Ga – giga-annum (one billion years)

Ma – mega-annum (one million years)

ka – kilo-annum (one thousand years)

ppm – parts per million

XRF – X-Ray Fluorescence

Terr. In. – Terrigenous Input

CIA – Chemical Index of Alteration

CIW – Chemical Index of Weathering

ICV – Index of Compositional Variability

PIA – Plagioclase Index of Alteration

RSL – Relative Sea Level

HST – Highstand Systems Tract

FSST – Falling Stage Systems Tract

LST – Lowstand Systems Tract

TST – Transgressive Systems Tract

SB – Sequence Boundary

MFS – Maximum Flooding Surface

MAJFS – Major Flooding Surface

Chapter 1: Introduction

1.1 Thesis Rationale

Turbidite systems constitute the largest depositional elements on Earth and are built up of sediment deposited principally by turbidity currents. On the continental slope sinuous levee-bound channels convey these currents to the basin floor, but being located in deep water, the destructive nature of turbidity currents, and the fact that modern channels are open geomorphic elements with little accumulated sediment, makes understanding the history of slope channel fills problematic. Accordingly, ancient turbidite systems, like the Neoproterozoic Windermere Supergroup in the southern Canadian Cordillera, provide insight into the internal stratigraphy and architecture of slope channel systems and the opportunity to unravel the autogenic and allogenic parameters that control their temporal evolution.

Leveed slope channel complexes are well exposed in the Castle Creek study area. Over the past ~ 20 years several researchers from the University of Ottawa have studied various parts of the seven exposed channel complexes: ICC0 – Billington (2019); ICC1 – Navarro (2006), Anthony (2011), Dumouchel (2012), Milczarek (2018), Fraino (2020); ICC2 – Arnott (2007); Dumouchel (2015); ICC3 – Navarro (2006); Khan (2012), Huyer (2016); ICC4 – Altosaar (2007); Mussa-Caleca (2008); Davis (2010), Miklovich (2017), Bergen (2017); Dumouchel (2015); ICC5 – Schwarz (2007); ICC6 – Gammon (2007), Tan (2011). These earlier studies were confined to well exposed areas adjacent to the Castle Creek glacier. This study adds a new study site, the Hill Section. Here, like in the previous studies, a detailed sedimentological and stratigraphic analysis was conducted on strata which extend from ICC1 to ICC6. These data were then combined with those from the previous studies to create a single compilation of stratal elements that make up the Isaac Formation in the greater Castle Creek study area. The final objective was to identify any systematic changes in the stratigraphic make up of Isaac channel complexes and attempt to identify the underlying autogenic and/or allogenic sedimentological parameters that consistently and repetitively controlled the depositional history of Isaac leveed-slope channels.

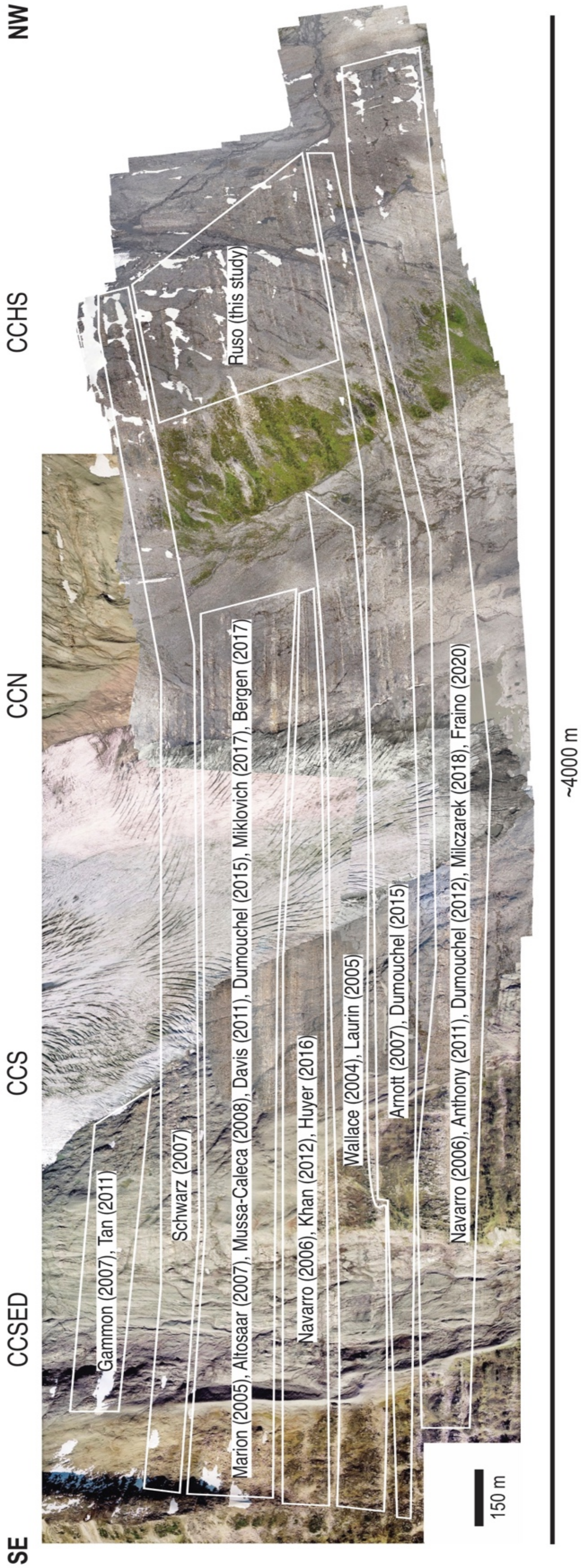

Figure 1.0. White boxes indicate locations of previous studies carried out at Castle Creek by numerous authors over the past two decades.

1.2 Geological Background and Regional Stratigraphy

1.2.1 Overview

The Neoproterozoic (1000-544 Ma) was a time in Earth's history characterized by dramatic global change: the break-up of Rodinia, global glacial events, wide variability in oceanic isotopic composition, and the appearance of the first metazoans (Ross & Arnott, 2007). It is at this time that deposition of the Windermere Supergroup (WSG) took place (Ross & Arnott, 2007). In outcrop the WSG extends from northern Mexico northward to the Yukon-Alaska border – a strike length of over 4000 km (Ross & Arnott, 2007; Ross, 1991). In the southern Canadian Cordillera, metasedimentary rocks of the WSG are exposed over an area of 35,000 km^2 in the western Main Ranges and Omineca Belt. Here the WSG forms an up to 9 km-thick succession of exceptionally well preserved deep-marine siliciclastic and carbonate rocks (Ross & Parrish, 1991).

1.2.2 Tectonic Setting

Strata of the Windermere Supergroup record deposition in a west-facing passive margin basin associated with the breakup of the supercontinent Rodinia during the Neoproterozoic (Ross et al., 1995). The breakup of Rodinia occurred between 780-580 Ma, recording multiple episodes of rifting that eventually led to the disassembly of the supercontinent (Li et al., 2013). Ross (1991) proposed a two-step model for the evolution of the WSG, where in the southern Canadian Cordillera initial sedimentation occurred during early continental rifting within fault-bounded basins and deposited the Irene and Toby formations (see below). Continental separation was followed by post-rift deep-marine sedimentation of the Kaza and Cariboo groups controlled by progressively diminishing rates of thermal subsidence (Ross, 1991). Alternatively, Colpron et al. (2002) suggested that two rift events occurred during WSG deposition, with the first taking place during the early stages of Rodinia break up (~700-750 Ma). This event opened a north-facing passive margin basin in northern Laurentia that further to the south extended into a 2500 km-long intracontinental rift where the deep-water Windermere turbidite system accumulated. This was then followed by a second rifting event at ~ 600-570 Ma (Hamill-Gog extensional event) when a second crustal block separated from the western margin of Laurentia (Colpron et al., 2002). This event was correlated to the unconformity that caps the Windermere sedimentary pile (e.g., Aitken, 1969), and with later subsidence formed the economically important Western Canada Sedimentary Basin (Bond et al., 1984). However recent work by Hadlari et al. (in review) showed that deep-water Windermere strata over much of the southern Canadian Cordillera exhibit a consistent assemblage of Paleoproterozic and Archean detrital zircons that resembles the bimodal distribution reported previously by Ross and Bowring (1990) (Figure 1.1).

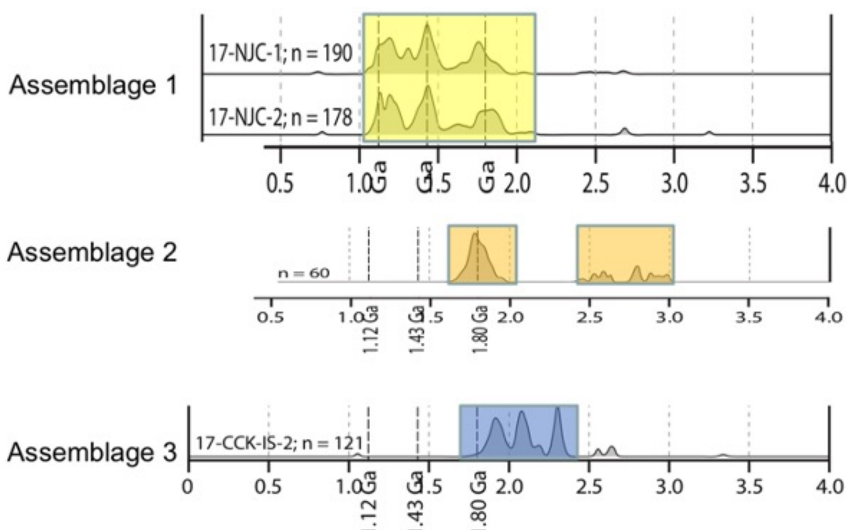

Figure 1.1. U-Pb detrital zircon assemblages in WSG strata of the southern Canadian Cordillera. Note Assemblage 2 represents the archetypal (bimodal) WSG detrital zircon signature (Hadlari et al., in review).

The character of this zircon assemblage indicates the absence of a western sediment source, and therefore the Windermere turbidite system in the southern Canadian Cordillera, like coeval strata in the northern Canadian Cordillera, accumulated along the passive margin of Laurentia. Furthermore, Hadlari et al. report the occurrence of a population of 666 Ma detrital zircons that they attribute to the minimum age of continental separation, which then was followed by thermal subsidence and deep-marine sedimentation after ~ 650 Ma. With time and diminishing rates of thermal subsidence, deposition created the several kilometer-thick, upward-shoaling (basin floor to continental shelf) Windermere turbidite system related to progradation of the Laurentian continental margin into the proto-Pacific Ocean (Ross and Arnott, 2007; Hadlari et al., in review).

1.2.3 Regional Stratigraphy

The Windermere Supergroup crops out discontinuously along western North America (Figure 1.2A). In the western United States, shallow-marine to continental deposits crop out in the Sevier Belt and Basin and Range (Ross & Arnott, 2007). In Canada, WSG strata crop out as upper-slope to shallow-marine deposits in the Mackenzie Mountains of the northern Cordillera, and in the southern Canadian Cordillera (SCC) they comprise a deep-marine turbidite system (Figure 1.2B) (Ross, 1991).

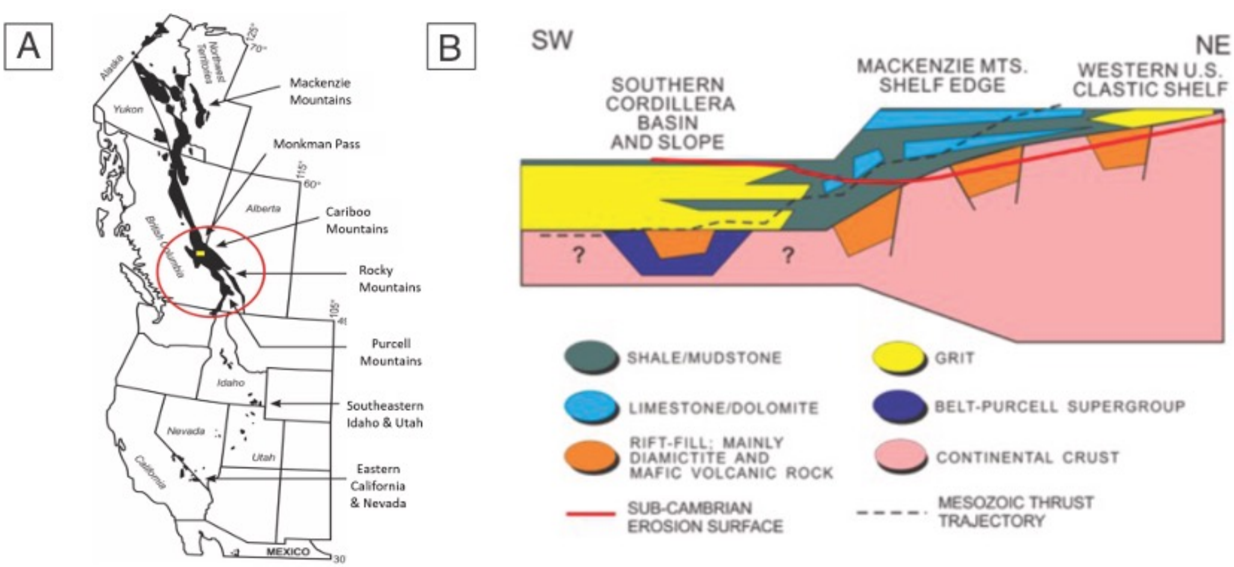

Figure 1.2. A) Distribution of WSG strata throughout western North America (black polygon). Red circle indicates strata of the WSG in the southern Canadian Cordillera and yellow rectangle indicates location of the Castle Creek study area. Deep-marine section located in red square (Ross, 1991). B) Cross section of the WSG. Deep marine strata located in the SCC, shelf strata in the Mackenzie Mountains in the northern Cordillera, shallow marine and continental strata located in western U.S.A. (Fraino, 2020 modified from Ross & Arnott, 2007).

In the southern Canadian Cordillera, the WSG unconformably overlies the Belt-Purcell Supergroup (1.5-1.4 Ga) (Figure 1.3) or crystalline basement (2.2-0.7 Ga) likely associated with the Canadian Shield (Ross & Arnott, 2007; Hadlari et al., in review). The base of the WSG consists of glaciogenic diamictite and mafic volcanic rocks of the Toby and Irene formations, respectively (Ross, 1991). The Toby and Irene formations show evidence of syn-depositional extensional faulting in the form of abrupt lateral facies changes, in addition to major changes in stratal thickness (as much as 1800 m in the Toby), which are attributed to deposition during the early rifting phase of WSG sedimentation (Aalto, 1971; Smith et al., 2014). The Toby Formation consists of diamictite intercalated with beds of argillite, conglomerate, and sandstone, and is interpreted to have been deposited during the Sturtian glaciation between 700-750 Ma (Aalto, 1971; Ross et al., 1995). The Irene Formation is up to 1600 m thick and consists of pillowed volcanic flows and mafic igneous rocks, supporting the interpretation of deposition during a period of extensional tectonism associated with the breakup of Rodinia (Ross et al., 1995).

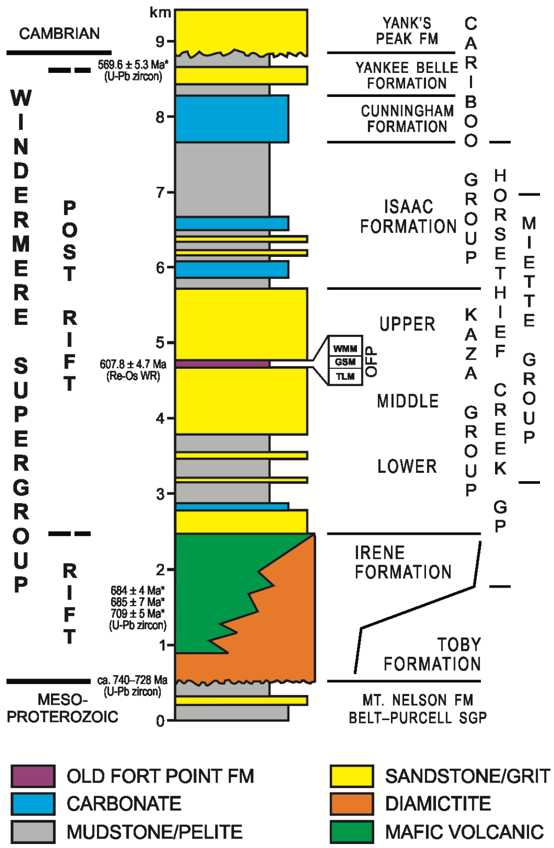

Figure 1.3. Stratigraphic column of the WSG in the southern Canadian Cordillera (Smith et al., 2014 modified from Ross et al., 1995).

Rift-phase strata are then overlain by an up to 5 – 7 km thick, upward-shoaling succession of coarse sandstone, mudstone, conglomerate, and lesser limestone of the Kaza Group (termed Lower Miette Group in the Rocky Mountains and Horsethief Creek Group in the Purcell Mountains) overlain by the Cariboo Group (Ross et al., 1995). The Kaza (~ 3 km thick) is subdivided into the Lower, Middle, and Upper Kaza groups and is dominated by sheet-like sandstones representing basin floor terminal fan deposition (Terlaky et al., 2016). The Kaza is overlain conformably by the Isaac Formation (base of the Cariboo Group), a ~ 2 km-thick section of mudstone-rich strata with up to 200 m-thick, laterally discontinuous sandstone and conglomerate units interpreted to be leveed slope channels, in addition to common mass transport deposits (debris flows, slumps/slides) indicative of (continental) slope instability (Ross & Arnott, 2007; Navarro & Arnott, 2019). Overlying the Isaac Formation are upper slope and shelf strata of the Cunningham (up to 800 m thick) and then Yankee Belle (~ 2 km thick) formations composed of oolitic-intraclastic limestone and mixed siliciclastic-carbonate rocks, respectively (Ross et al., 1995; Reid et al., 2002; Terlaky et al., 2016). In the southern Canadian Cordillera, much of these shallow-water strata have been eroded by the sub-Cambrian unconformity that relates to the second rift event around 570 Ma and caps the WSG (Aitken, 1969). Collectively, these post-rift strata form a 5 – 7 km-thick upward-shoaling succession interpreted to record the westward progradation of the Laurentian continental margin into the proto-Pacific Ocean (Ross & Arnott, 2007).

1.2.4 Geochronology & Provenance

Although sparse, geochronologic data below and above the WSG bounding unconformities indicate a maximum age for WSG deposition between 740 and 723 Ma, and a minimum of 570 Ma, the latter related to the onset of Hamill-Gog extensional volcanism (McDonough & Parrish, 1991; Colpron et al., 2002). Indirect dates provided by detrital zircons in syn-rift volcanic and magmatic rocks at the base of the Windermere sedimentary pile in the southern Canadian Cordillera indicate rift-related volcanism between ~ 700-680 Ma, including the Gataga volcanics in northern British Columbia (696-690 Ma) (Macdonald et al. 2018) and 700-680 Ma rift volcanics in Idaho (e.g., Lund et al., 2003; Keeley et al., 2013). More recently, a zircon peak at approximately 666 Ma provides a minimum age for rift-related volcanism, which is interpreted to be coincident with continental break up, and therefore the maximum age for deposition of the Windermere turbidite system (Hadlari et al., in review). Direct dating within the WSG in the southern Canadian Cordillera is confined to a single Re-Os date of 608 Ma (Kendall et al., 2004) from a black shale in the Old Fort Point Formation (Smith et al., 2014).

Provenance studies reveal a bimodal distribution of detrital zircon ages throughout the WSG: 1950 - 1750 Ma and > 2600 Ma (Ross & Parrish, 1991; Hadlari et al., in review) (Figure

1.1). These ages suggest a source area from the southern Canadian Shield and eastern Belt Basin (Ross & Arnott, 2007; Hadlari et al., in review) and the absence of a 1.6 - 1.5 Ga population eliminates a western source. However, recent U-Pb zircon data show a subpopulation of 2.3 to 1.9 Ga zircons in a single sample from slope channel deposits of the Miette Group near Jasper, Alberta, suggesting a temporary change in provenance from east/southeasterly to northerly and then back to east/southeasterly (Hadlari et al., in review). In addition, limited paleocurrent data in the WSG show general sediment transport toward the northwest, and therefore with the detrital zircon data, suggest a single, continental-scale turbidite system fed almost entirely by a southeasterly sediment source (Terlaky, 2014).

1.2.5 Lithostratigraphic Markers

Due to the lack of direct dating and biostratigraphic control, geochronological constraints for the WSG are generally limited to igneous rocks above and below bounding unconformities. However, within the WSG in the southern Canadian Cordillera is the lithologically and geochemically distinctive Old Fort Point Formation (OFP) which forms an easily recognized stratigraphic marker that extends across the entire Windermere deep-water basin. The OFP ranges from 60 - 450 m thick and comprises three lithologically distinct members: the basal Temple Lake Member (TLM), Geikie Siding Member (GSM), and the Whitehorn Mountain Member (WMM) (Smith, 2009). The OFP is interpreted to relate to a major eustatic rise that effectively reduced siliciclastic input into the WSG system, which then was followed by a eustatic fall that incised channels into the basin slope (Ross & Arnott, 2007; Smith et al., 2014).

The base of the TLM contains fine-grained siliciclastic siltstone overlain by rhythmically bedded limestone-siltstone couplets deposited as sea level transgressed, carbonate production began on the shelf, and sediment supply from the hinterland was reduced (Smith et al., 2014).

Organic-rich mudstones of the GSM gradationally overlie the TLM and record the shutdown of carbonate production as sea level reached highstand conditions (i.e., maximum flooding) (Smith, 2009). In contrast to the TLM and GSM, the WMM records evidence of both high- and lowstand conditions and has been influenced by a number of sedimentary controls. The base of the WMM is sharp and locally deeply scoured, recording the incision of channels into the slope during falling relative sea level (Smith et al., 2014). The fall in sea level has also been attributed to rifting along the continental margin, accounting for an anomalously thick (>200 m) unit at Frances Creek in the Purcell Mountains (Smith et al., 2011). Deposition of turbidites at the onset of sea level rise was followed by siliciclastic input from the hinterland as well as carbonate input, as carbonate production restarted on the shelf (Smith et al., 2014).

The lower two members (TLM and GSM) of the OFP have been associated with transgressive and highstand conditions related to a major deglacial event, whereas the topmost member (WMM) is associated with lowstand conditions related partly to rifting (Smith et al., 2011). The OFP has been correlated to post-glacial strata overlying the glaciogenic Ice Brook Formation (Marinoan glaciation) in the Mackenzie Mountains, thus linking the OFP to the 655-635 Ma Marinoan glaciation (Smith et al., 2014). However, the measured Re-Os date of 607.8 ± 4.7 Ma by Kendall et al. (2004) makes this correlation problematic, although a date of 634 ± 57 Ma by these same authors, but using a different analytical procedure, may be more representative (Smith et al., (2014a)

1.2.6 Metamorphism

The WSG in the southern Canadian Cordillera was subjected to orogenic deformation during the Mesozoic as exotic terranes accreted onto the western margin of Canada between 170 - 55 Ma (mid-Jurassic to Eocene) (Reid et al., 2002; Ross & Arnott, 2007). Here the Cordillera is subdivided into five morphogeographic belts: Foreland Fold and Thrust, Omineca, Intermontane, Coast, and Insular belts (Figure 1.4) (Monger & Price, 1979).

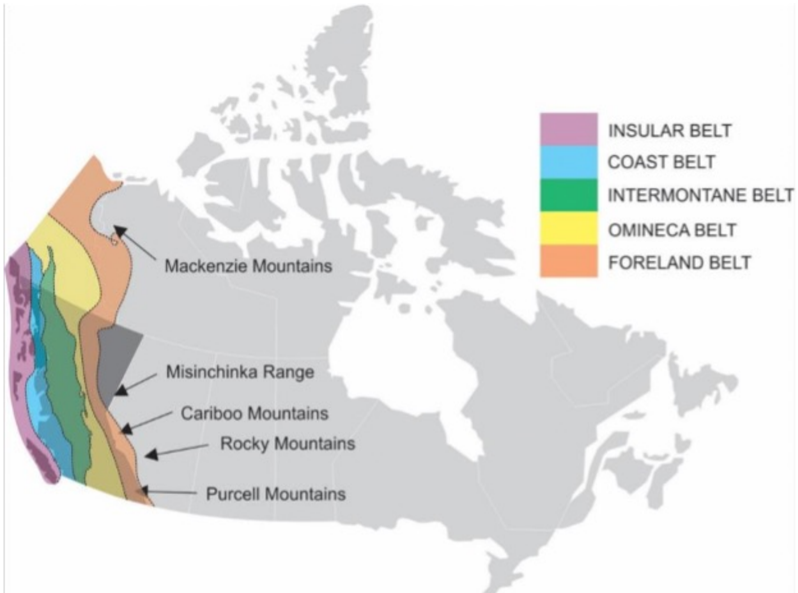

Figure 1.4. Map of the five morphogeographic belts that make up the Canadian Cordillera (Fraino, 2020 modified from Davis, 2011).

In the Omineca Belt metamorphic grade increases from sub-greenschist in the northern Cariboo Mountains to upper amphibolite in the southern Cariboo and western Purcell Mountains (Smith et al., 2011). Variability in metamorphic grade in the southern Canadian Cordillera is due to an overall northwest plunge of Jurassic folds that expose deeper structural levels, and thus higher metamorphic grade toward the southeast (Reid, 2003). Areas of low metamorphic grade, such as the Castle Creek study area in the northern Cariboo Mountains, exhibit exceptionally well-preserved sedimentary structures and textures allowing for detailed mapping and analysis of strata.

The Cariboo Mountains have been affected by four phases of deformation (D1-D4) and two episodes of low-grade metamorphism (M1 and M2) (Murphy 1987). D1 is associated with the mid-Jurassic obduction of a terrane onto western North America, forming east to northeast-verging folds (F1) and cleavage subparallel to bedding (Murphy, 1987; Reid et al., 2002). This event occurred along with the first metamorphic event (M1) characterized by biotite or lower-grade metamorphism (Ross & Arnott, 2007). The second phase (D2) formed centimetre- to kilometre-scale southwest-verging folds (F2) that refolded earlier F1 structures and produced a crenulation cleavage (Reid et al., 2002, Reid, 2003). The second metamorphic event (M2) post-dated this phase based on mineral overgrowths around D2 structures (Murphy, 1987). The main regional structures in the Cariboo Mountains, such as the Isaac Lake Synclinorium where the Castle Creek study area is located on its eastern side, were produced during the D2 phase (Murphy, 1987). Structures of phases D1 and D2 are crosscut by the 174 Ma Hobson Lake Pluton, indicating that they predated the mid-Jurassic (Reid et al., 2002). Phase D3 includes strike-slip faulting and production of kilometre-scale folds (F3) that re-folded D2 structures, followed by the final deformation phase (D4) (Reid et al., 2002). Northeast-verging post-metamorphic D4 structures deform pre-existing D1-D3 structures and occur locally at the centimetre- to metre-scale as kink bands and kink folds (Murphy, 1987; Reid et al., 2002).

1.3 Castle Creek Study Area

The Castle Creek study area is located in the northern Cariboo Mountains in British Columbia, Canada (Figure 1.5A). Here, vertically dipping slope channel-levee deposits of the Neoproterozoic Isaac Formation (Figure 1.5B) crop out and form a 20 km^2 exposure. Due to very recent glaciation (less than about 100 years) surface vegetation is absent, which then allows for detailed mapping and stratigraphic analysis on scales that range from architectural elements (Dm) to sedimentary structures (cm).

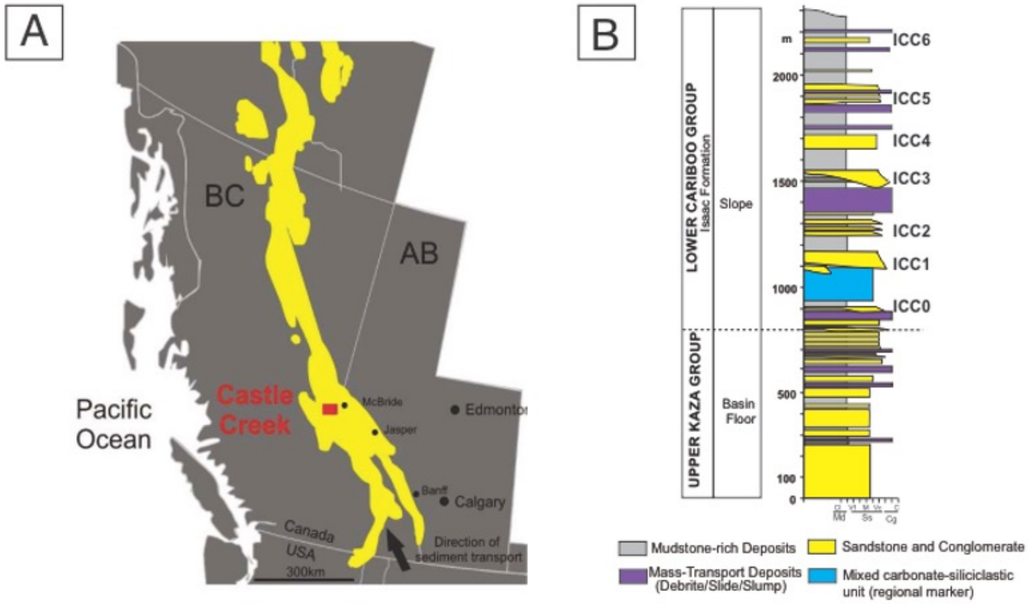

Figure 1.5. A) Location of Castle Creek study area in the SCC (Davis, 2011 modified from Ross et al., 1995). B) Stratigraphic Column of the Upper Kaza Group and Isaac Formation at Castle Creek.

1.4 Methods

Fieldwork was conducted at the Hill Section outcrop (1 km^2) in the Castle Creek study area over the course of 3 weeks. Detailed stratigraphic logs (9-244 m) were measured at 18 locations to describe bed thickness, basal contacts, grain size, lithology, and sedimentary structures at the cm-scale. Paleocurrent was also measured where possible. Prominent beds and surfaces were traced by being “walked out” in the field, and high-resolution aerial photos were used to correlate beds and illustrate lithological trends at the element (km) scale.

A total of 14 samples were obtained for thin section analysis using a rock saw to cut small (~10 cm by ~5 cm) slabs. Thin sections were used to characterize microscale structures, grain size, and composition of key facies identified in the field. Shale samples were taken every 10 m along an ~ 1 km vertical transect in the Hill Section, in addition to the Castle Creek North, and Castle Creek South outcrops, totalling 248 samples. These samples were prepped for X-Ray Fluorescence (XRF) analysis: they were initially crushed into pieces using a rock hammer then pulverized using a TM/SLTX mill. Crushed samples were loaded into the grinding barrel and pulverized for three minutes. The grinding barrel was cleaned between each sample by pulverizing quartz sand for four minutes, then rinsing with distilled water and ethanol. Loss on Ignition (LOI) was then measured for all pulverized samples to individually calibrate each XRF analysis. Approximately 1 g of sample was loaded into a crucible, measured, and heated in an oven at 1050°C for 1 hour. The final measured weight (i.e., post-heating) minus the initial weight indicates the LOI. The portion of sample used for LOI was then discarded and not used for XRF analysis.

XRF analysis was conducted at the University of Ottawa X-Ray Core Facility to assess bulk composition. The international standard GSP-2 (granodiorite from United States Geological Survey) was run as a check sample on day of analysis to calibrate the machine and ensure accuracy. Certified Reference Materials used to calibrate felsic curves were AMH-1, GSP-2, GS-N, AN-G, SY-3, MA-N, OU-3, BCR-032, PC-1016, GPO-16, GPO-17, GPO-18, and MRG-1. Exactly 0.8 g of pulverized sample was mixed with a lithium-borate solution and fused into a disk, which was then exposed to incident X-rays in a WDXRF Rigaku 200 supermini. The amount and type of reflected rays were recorded and graphed using an analytical software; each ray corresponds to a different element, representing the bulk composition of each disk (sample).

Chapter 2: Deep Marine Sedimentation Processes & Deposits

2.1 Introduction

Mass movements and sediment-gravity flows are important gravity-driven processes for transporting sediment and organic matter into the deep sea. These subaqueous flows are responsible for building up some of the thickest and largest sediment accumulations on Earth (e.g., modern Bengal Fan), which in some places form important oil and gas reservoirs (Kneller & Buckee, 2000; Talling et al., 2012). However, these flows, which can be triggered by a number of mechanisms including, but not limited to, earthquakes (e.g., 1929 Grand Banks event, eastern Canada), slope instability, and high sedimentation rates (Shanmugam, 2006), also represent economic and environmental hazards, such as the destruction of submarine cables and transport of terrestrial pollutants into the deep ocean (Kneller & Buckee, 2000).

This thesis adopts the simplified classification system of Mulder and Alexander (2001) for subaqueous sediment transport based on particle cohesivity, particle support mechanisms, and sediment concentration (Figure 2.1A). Sediment-gravity flows are subdivided into two end-member types: cohesive and non-cohesive (frictional) flows, where cohesive flows are dominated by matrix strength due to particle-particle bonding and non-cohesive flows where particles are dispersed in a fluid (Mulder & Alexander, 2001).

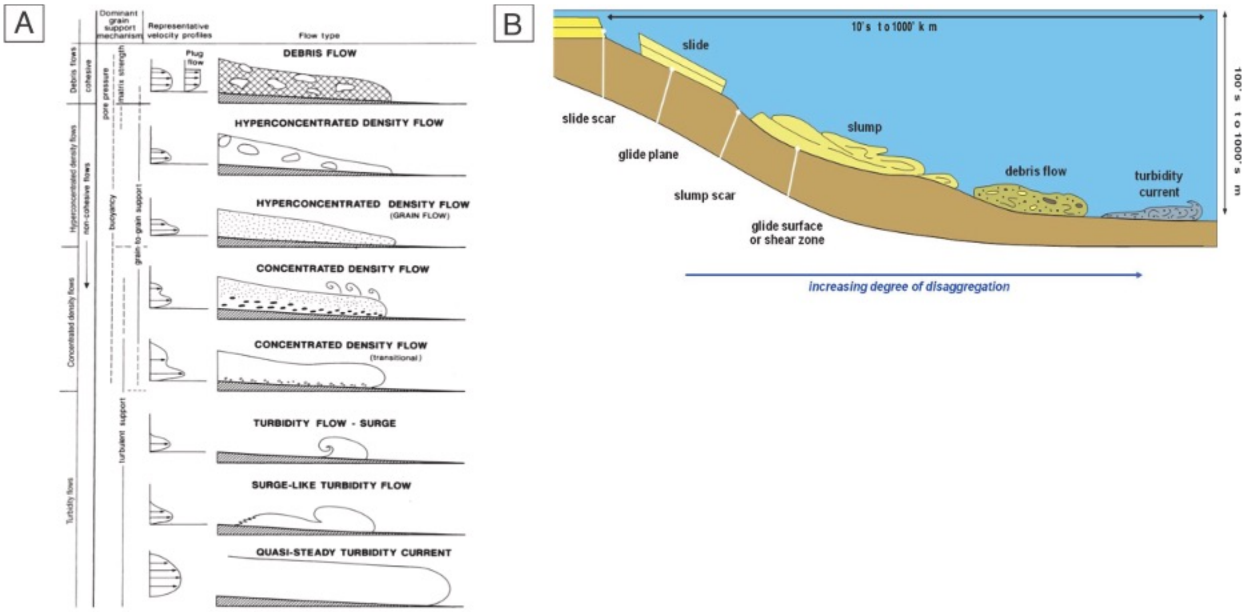

Figure 2.1. A) Classification scheme for sub-aqueous sediment transport by Mulder and Alexander (2001) based on the dominant particle support mechanism, particle cohesivity, and sediment concentration. B) Illustrations of subaqueous sediment gravity flows (modified from Shanmugam, 1994).

2.1.1 Mass Movements

Mass movement is the gravity-driven displacement of a sediment volume when gravity exceeds the tensile strength of the sediment pile, causing it to move along internal failure planes (Figure 2.1B) (Arnott, 2010). Mass movements are subdivided into slides and slumps based on the nature of movement and amount of internal deformation, which in slides is typically confined to listric faults that fragment the sediment mass into a number of coherent blocks and movement is translational. Slumps, on the other hand, exhibit more ductile deformation with common folds and evidence of rotational movement (Shanmugam, 2006). Both deposit *en masse* when friction at the base of the moving sediment mass overcomes the gravitational driving force.

2.1.1 Sediment-Gravity Flows

Sediment-gravity flows, as defined by Middleton and Hampton (1973), are sediment-laden flows in which the interstitial fluid is driven downslope due to gravitational forces acting on suspended sediment particles. They are commonly subdivided into four types based on dominant particle support mechanism: turbidity currents, fluidized sediment flows, grain flows, and debris flows (Shanmugam, 2006). In a simpler classification model, Mulder and Alexander (2001) identified two end-member types of sediment-gravity flows: cohesive and non-cohesive (frictional) flows. Cohesive flows contain a cohesive matrix that helps to resist dilution by deposition or fluid entrainment (Mulder & Alexander, 2001; Arnott, 2010). Non-cohesive flows form a continuum from mass movements to turbidity currents and are subdivided based on dominant particle support mechanisms, including buoyancy, matrix strength, pore pressure, grain-to-grain interaction and fluid turbulence (Mulder & Alexander, 2001).

2.1.3 Cohesive Flows

2.1.3.1 Debris Flows

Based on sediment characteristics, cohesive flows are divided into debris flows and mud flows: mud flows contain < 5% gravel by volume and their deposits consist mostly of fine-grained sediment, with in some cases rare, isolated blocks composed of coarse sediment (Mulder & Alexander, 2001). Debris flows contain > 5% gravel by volume that commonly range up to boulders and olistoliths (Mulder & Alexander, 2001). Matrix strength, created by the chemical bonding of adjacent clay-size clay minerals, is the dominant particle support mechanism in debris flows and imparts a pseudoplastic rheology to the flow and will deform only after a critical yield stress has been exceeded (Mulder & Alexander, 2001; Shanmugam, 2006).

Deposition from debris flows occurs by cohesive freezing when the internal shear resistance (fluid viscosity and grain-to-grain friction) overcomes the driving gravitational force and causes the flow to freeze *en masse* when the downward thickening of a non-deforming plug region intersects the base of the flow (Arnott, 2010). Deposits of debris flows, termed “debrites”, are sheet-like to lobate shaped and can be up to kilometres in length and > 100 m thick: deposit thickness approximating the thickness of the parent flow (neglecting post-depositional compaction) (Arnott, 2010). Debrites are characteristically very poorly sorted with a chaotic arrangement of variably sized clasts ranging from sand to boulders.

2.1.4 Non-cohesive (frictional) Flows

2.1.4.1 Hyperconcentrated Density Flows

Hyperconcentrated density flows are similar to cohesive flows in that they are gravity-driven and contain similar proportions of sediment and fluid; however they do not behave plastically but instead are friction-dominated (Mulder & Alexander, 2001; Arnott, 2010). In contrast to cohesive flows, hyperconcentrated density flows have interconnected pore spaces allowing for dilution and expansion of the flow into a less concentrated density flow (Mulder & Alexander, 2001). Hyperconcentrated density flows contain > 25% sediment concentration by volume and the dominant particle support mechanism is grain-to-grain interaction (Mulder & Alexander, 2001). Frictional freezing due to grain interlocking is the main depositional mechanism and deposits are typically coarse-grained (e.g., and massive with little to no grading, although local inverse grading may occur through the development of traction carpets or kinetic sieving (Mulder & Alexander, 2001; Talling et al., 2012).

2.1.4.2 Concentrated Density Flows

Concentrated density flows are more dilute than hyperconcentrated density flows due to the entrainment of ambient fluid, typically seawater, which effectively reduces sediment concentration and particle interaction. The transition from hyperconcentrated to concentrated density flow depends on grain size, sorting, and thickness of the flow, and according to Mulder and Alexander (2001), occurs when flow dilution allows the upper part of the flow to become fully turbulent and hence sufficiently dilute to allow differential particle settling, and thus effects sorting during transport. The near-bed region in concentrated density flows behaves similar to hyperconcentrated density flows (high sediment concentration) with grain-to-grain interaction being the dominant particle support mechanism, whereas the more dilute top of the flow is dominated by turbulent particle support (Mulder & Alexander, 2001). Buoyancy may also play a role in particle support in the lower part of the flow (Talling et al., 2012).

Deposits of concentrated density flows are characterized by an erosional base overlain by a normally graded or massive sandstone (Bouma Ta, see below) (Mulder & Alexander, 2001). Traction carpets may develop due to the presence of a thick, hyperconcentrated near-bed layer in which sediment, and energy, is supplied by the overlying turbulent suspension. Turbulence in this layer is damped by the concentration gradient (i.e., stratification effect) and also consumed by particle suspension (concentration effect), resulting in the deposition of massive or upward-thinning- or -thickening beds (Sohn, 1997). Inverse grading is common in traction carpet deposits and was interpreted by Sohn to be a consequence of dispersive pressure related to grain-grain interaction, whereby fine-grained sediment migrated preferentially into the area of higher velocity gradient near the bed and coarser sediment moved upward. Furthermore, Sohn reported that traction carpets were composed of two parts: a basal frictional layer where grain concentration is high and grains are constantly in contact, and an upper collisional layer where grain concentration is sufficiently low that grains are separated and therefore collide. Later, Le Roux (2003) described the collisional layer as a zone of flow expansion and the frictional layer as an area of compaction where kinetic sieving causes fine grains to percolate between larger grains which in turn are displaced upward (Sohn, 1997; Le Roux, 2003).

2.1.4.3 Turbidity Currents

Turbidity currents are the most common non-cohesive flows and are defined as sediment-gravity flows where the upward component of fluid turbulence is the dominant particle support mechanism. Their deposits make up much of the deep-marine sedimentary record, but due to their destructive and unpredictable nature, observing turbidity currents *in situ* has proven to be difficult (Arnott, 2010). Pioneering lab experiments on turbidity currents by Kuenen and Migliorini (1950) noted a characteristic upward-fining in the deposits of these flows. These experiments were then followed by many other flume experiments and papers describing the mechanics of turbidity currents, the factors that influence them, and the make-up of their deposits (e.g., Kuenen, 1957; Middleton 1966a, b, 1967; Mutti & Ricci Lucchi 1972, 1975, 1978; Middleton & Hampton 1973, 1976; Stow & Shanmugam, 1980).

Traditionally, turbidity currents are considered to consist of three distinct parts: head, body, and tail. The head is sediment-rich and continuously supplied with sediment by the faster-moving body, whereas the tail of the flow is sediment poor and slow moving (Arnott, 2010). The head is characterized by a sharp, overhanging nose and contains the coarsest sediment, whereas finer-grained sediment is swept upward and then back into the body of the current (Arnott, 2010). In this way, turbidity currents are highly longitudinally stratified in terms of grain size and idealistically would deposit an upward fining bed. Further, Sumner et al. (2008) suggested that decelerating flows could be subdivided vertically into three layers: 1) high-concentration, non-turbulent basal layer dominated by grain-to-grain interaction, 2) high-concentration turbulent suspension, and 3) a low-concentration turbulent suspension. Their experiments showed that the rate of flow deceleration, in addition to flow stratification, influence the characteristics in the deposit (Sumner et al., 2008). For example, a high sediment concentration gradient in the near-bed region effectively damps turbulence and allows for rapid deposition with minimal reworking or resuspension (i.e., massive) until flow speed and sediment concentration are sufficiently reduced to allow for bedload traction and individual particle suspension settling (Sumner, et al., 2008; Cantero et al., 2011).

Lowe (1982) subdivided turbidity currents into low- and high-density end members, where low-density currents contain < 9% by volume sediment concentration, termed the Bagnold limit, and particles are fully supported by fluid turbulence. Above this threshold additional particle support mechanisms like dispersive pressure, hindered settling, and buoyancy must also operate to counteract grain-to-grain collisions that damp turbulence. These high-density turbidity currents (and associated deposits) were then further subdivided into sandy (S1-S3) and gravelly (R1-R3) types (Figure 2.2A). The “S” beds consist of clay- to small pebble-sized sediment and represent three stages of deposition: 1) traction sedimentation, 2) traction carpet sedimentation, and 3) suspension sedimentation (Lowe, 1982). Gravelly high-density turbidity currents deposit traction structured (R1), inversely graded (R2), and normally graded (R3) gravel beds (Lowe, 1982).

In contrast, (decelerating) low-density turbidity currents deposit, in whole or in part, a classical Bouma Ta-e turbidite; an upward-fining succession with a characteristic suite of sedimentary features that was first described by Bouma (1962) (Figure 2.2B). The Bouma Ta division is characterized by structureless and normally graded sandstone deposited rapidly from suspension and is analogous to Lowe's (1982) S3 bed. The Tb division is composed of medium- to fine-grained, planar-laminated sandstone deposited as a featureless bed on which sediment transport was more or less spatially uniform, either because of high flow speed (i.e., upper regime plane bed) or near-bed sediment and hydraulic conditions inhibited the inception and amplification of bed-surface defects (Arnott, 2012). The Tc division typically consists of fine-grained, ripple cross-stratified sandstone; cross-stratification being the manifestation of an initial bed defect that amplified and eventually evolved into a bedform; in this case, a ripple (Arnott, 2012). The Td division consists of planar-laminated mudstone deposited by a rhythmic alternation of bed-load traction and suspension-load fallout (Stow and Bowen, 1980); specifically, as silt settles to the bed from a clay-silt suspension the near-bed clay concentration increases and eventually leads to flocculation and rapid deposition of an overlying clay-rich layer once a critical concentration, termed the gelling concentration, is reached. Finally, the uppermost Te division is composed of massive mudstone deposited by suspension-load fallout.

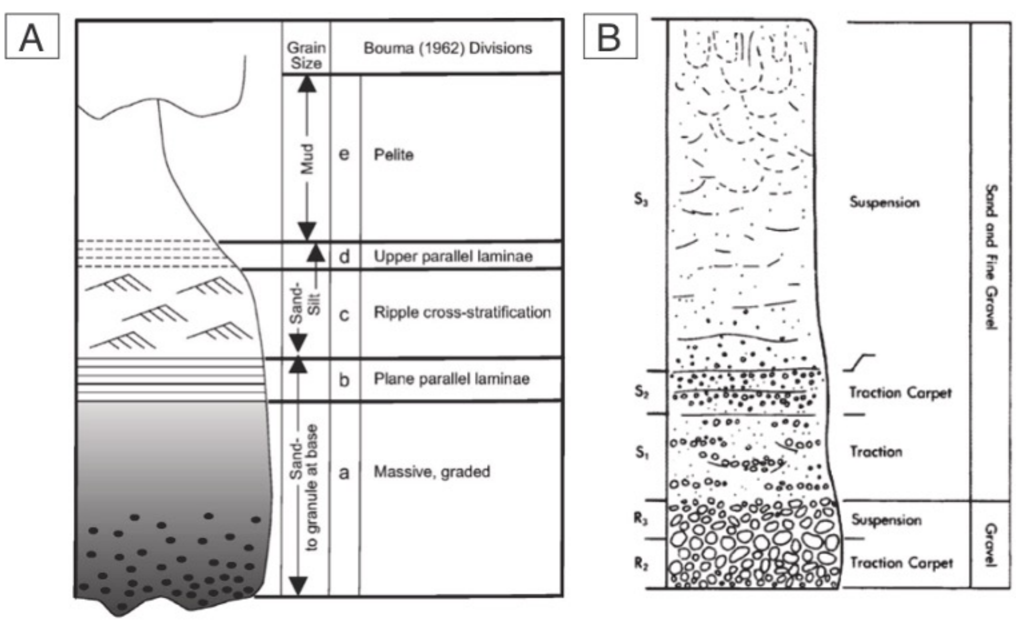

Figure 2.2. A) Cartoon of classical Bouma T_a to T_e division turbidite structures as described by Bouma (1962) (Arnott, 2012). B) R and S parts deposited by gravelly and sandy high-density turbidity currents (Lowe, 1982).

Interestingly, dune-scale cross-stratification is rarely observed in the deep-marine sedimentary record and is nearly absent in classical turbidites. Several hypotheses have been proposed, such as turbidity current deceleration was too rapid (Walker, 1965), sediment on the bed was too fine (Allen, 1970), or sediment fallout exceeded bedload transport (Arnott and Hand, 1989). Another consequence of high sediment fallout rate is the maintenance of a high near-bed concentration that sustains a stable interface between the concentrated near-bed layer and the bedload (i.e., reduces the density gradient). However, as the near-bed sediment concentration decreases (i.e., less fallout) an increasingly higher density gradient gives rise to an unstable interface that is able to generate bedforms (Figure 2.3) (Arnott, 2012). This hypothesis was tested recently by Tilston et al. (2015), who confirmed that a steep near-bed density gradient is required to generate a hydrodynamic instability of sufficient strength to imprint the bed and thus initiate angular bedform development. However, by the time a sufficiently steep density gradient is generated, the flow speed is likely in the ripple stability field and therefore unable to produce dunes (Arnott, 2012). In addition, Venditti et al. (2006) describe the near-bed layer as analogous to the viscous sublayer, implying that the hydraulically rough conditions required for dune formation cannot be met when generating bedforms in this manner (Liu, 1957; Venditti et al., 2006).

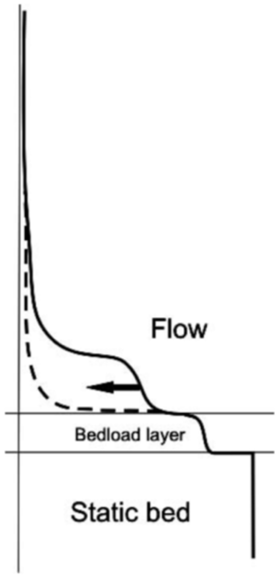

Figure 2.3. Sediment concentration profile of a clear water flow (dashed line) and a turbidity current (solid line). The initial high concentration bedload layer results in the generation of a stable interface between the turbidity current and the static bed until sediment concentration decreases sufficiently (arrow) to develop hydrodynamic instabilities to initiate the formation and propagation of bed defects (Arnott, 2012).

Chapter 3: Facies Descriptions and Interpretations

3.1 Facies F1 – Structureless Sandstone

3.1.1 Description

F1 consists of structureless, normally graded to ungraded sandstone typically overlain sharply by a mudstone layer that ranges from 0.5-2 cm thick (average ~ 1 cm). Normally graded beds (79%; Figure 3.1A) range between 13-252 cm and average about 85 cm thick. Massive beds (21%; Figure 3.1B) range between 17-94 cm thick and average ~ 40 cm. Basal contacts are usually sharp and planar (51%), though some are loaded (33%) scoured (7.0%), undulatory (3.0%), or wavy (6.0%); scours being of the order of ~ 2-5 cm deep. Mudstone clasts are observed in many F1 beds (25%) and range in thickness from 0.5-10 cm (average about 2 cm) and 5-80 cm (average about 8 cm) in length. Clasts are oriented subparallel to bedding and typically are confined to the basal 3-45 cm of the bed, but in some cases are distributed throughout the entire bed.

Based on field observations grain size generally ranges from lower medium- to upper coarse-grained sandstone, but typically is upper coarse-grained sandstone at the base grading upward to lower/upper medium-grained sandstone. Nevertheless, some beds consist of lower very coarse-grained sandstone with dispersed granules at the base and upper fine-grained sandstone at the top. Few beds contain dispersed very coarse sand grains in an upper medium- to coarse-grained sandstone matrix. Massive beds are typically lower medium- to lower coarse-grained sandstone.

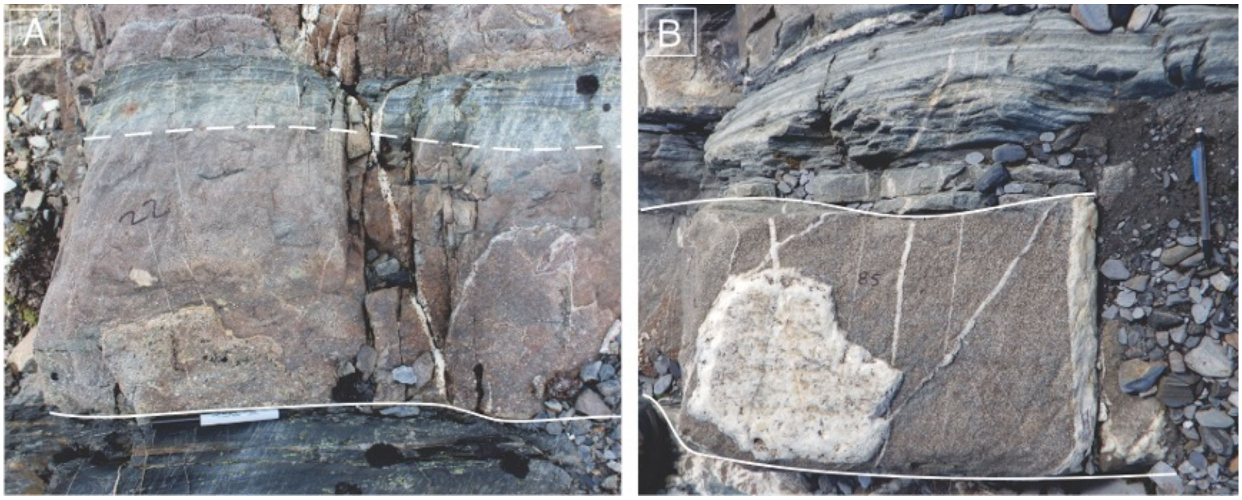

Figure 3.1. Facies F1. A) Normally graded F1 bed (granule conglomerate (see F3B description below) to fine-grained sandstone and overlain by graded mud-rich F2 bed (see F2 description below)). Sharpie is 14 cm long. B) Massive F1 bed, coarse-grained sandstone. Mechanical pencil is ~15 cm long.

3.1.2 Interpretation

Structureless F1 strata are interpreted to be equivalent to the Bouma (1962) Ta division turbidites or the Lowe (1982) S3 division deposited by sandy high-density turbidity currents, whereby grains are deposited directly from suspension. Similarly, Mulder & Alexander (2001) attribute the structureless nature of these beds to deposition by frictional flows with a thick hyperconcentrated near-bed layer. More specifically, near-bed sediment concentration was not only high but decreased rapidly upward and stably stratified the flow. This condition damped the upward diffusion of bed-generated turbulence, and therein one of the principal mechanisms maintaining sediment in suspension (Cantero et al., 2011, 2012). Additionally, turbulent kinetic energy is further damped in high concentration flows as kinetic energy is necessarily converted to potential energy to maintain the sediment suspension (Bennett et al., 2014). Together these effects result in a damping of fluid turbulence, including the important upward-directed component, and as a consequence deposition directly from suspension. Additionally, the absence of traction-transport structures suggests that the high rate of sediment fallout inhibited bed-surface sorting and therefore the development of stratification (e.g., Arnott and Hand, 1989) and/or near-bed density conditions that inhibited the initiation and amplification of bed-surface defects that otherwise would evolve into angular bed forms like ripples and dunes (Tilston et al. 2015; see Interpretation of facies F2 for more details). The presence of mudstone clasts indicates up-flow scouring of the muddy seafloor.

3.2 Facies F2 – Structured sandstone to mudstone

3.2.1 Description

Strata of F2 exhibit traction-transport sedimentary structures and form two end-member types: sand-rich and mud-rich.

Sand-rich beds are planar laminated (11.5%), ripple cross-stratified (64.5%), or planar laminated overlain gradationally by ripple cross-stratification (24%). Basal contacts are typically sharp and planar (80%), but wavy (9.5%), loaded (7.0%), scoured (3.0%), and gradational (0.5%) contacts are also observed. Planar-laminated sandstone beds are commonly ungraded, composed of upper medium- to upper fine-grained sandstone and range from 4-58 cm thick. Ripple cross-stratified sandstone beds are typically 1-6 cm thick, but rarely range up to 25 cm thick, and are composed of ungraded lower medium- to lower fine-grained sandstone. Beds consist of multi-set (32%; Figure 3.2A), single-set (43%; Figure 3.2B), or starved ripple formsets (25%). Sets range from 0.2-5 cm thick, but usually are 1 cm thick. Beds consisting of planar lamination overlain by ripple cross-stratification range from 26-256 cm thick and typically grade from upper medium- to very fine-grained sandstone (Figure 3.2C). Rare beds of lower coarse-grained, dune cross-stratified sandstone is observed and range in thickness from 6-80 cm, averaging 25 cm. The bases of dune cross-stratified beds are distinctively scoured (50%) and less commonly planar (40%) or wavy (10%). Most sand-rich beds are overlain sharply or gradationally by a planar-laminated or massive mudstone layer. Layers range in thickness from 0.5-10 cm but average around 1-2 cm, and where laminated, laminae are typically 0.1 cm thick or thinner.

Mud-rich F2 strata consist of planar-laminated siltstone overlain gradationally by massive mudstone. Basal contacts are dominantly sharp and planar (82.1%), although uncommon wavy (9.7%), loaded (6.0%), scoured (1.6%), gradational (0.6%) contacts are observed. Bed thickness ranges between 0.1-12 cm, averaging 1 cm.

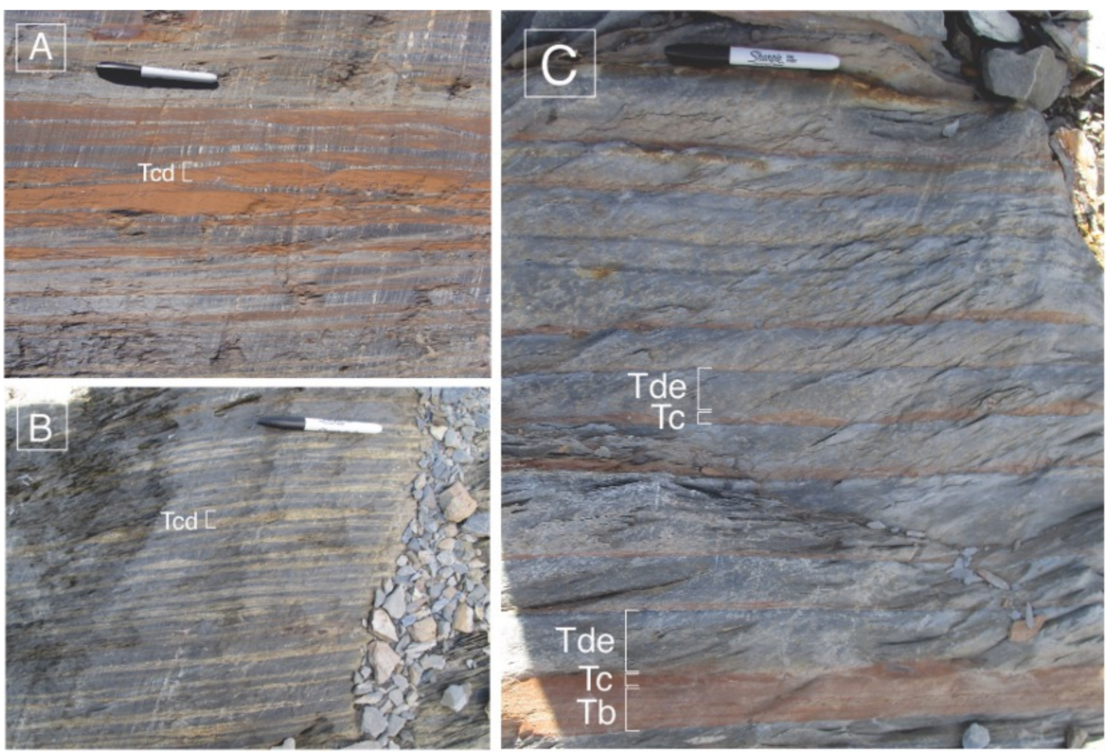

Figure 3.2. Facies F2. A) Multi-set ripple cross-stratified sandstone (T_c) sharply overlain bymudstone (T_{de}). B) Single-set ripple cross-stratified sandstone overlain by mudstone (T_{de}). C) Thinning upward succession of F2 strata; basal bedset consists of planar-laminated sandstone (T_b) sharply overlain by 1-2 sets of ripple cross-stratified sandstone (T_c) overlain by diffusely planar-laminated siltstone followed by a thin (<1 cm) bed of massive mudstone (T_e). Sharpie is 14 cm long.

3.2.2 Interpretation

F2 beds are interpreted to represent incomplete upper division Bouma turbidites deposited by decelerating turbidity flows (Lowe, 1982). Sand-rich, planar-laminated and ripple cross-stratified beds represent the Tb and Tc divisions, respectively, and the overlying mudstone layers and mud-rich F2 strata represent the Td/e divisions. Planar lamination (Tb) indicates that near-bed density conditions and/or flow speeds were unfavourable, at least initially, for the development of angular bed forms like ripples or dunes. Unlike the development of planar stratification in open channel flows, like rivers, planar stratification formed by turbidity currents indicates reduced rates of fallout compared to those that deposit graded, structureless sand (i.e., Ta) and the lamination to episodic deposition from laminar shear layers (*sensu* Vrolijk and Southard, 1997; see also Sumner et al., 2008). As deposition continued and planar-laminated sand (Tb) was succeeded by ripple cross-stratification (Tc), indicates an evolution of flow conditions that promoted the development of angular bed forms. However, these features require an initial bed-surface defect that modifies the pattern of near-bed fluid and sediment movement; more specifically, fluid flow lines to converge along the upflow side of the bed defect and then diverge as the flow separates from the bed on the downflow side, resulting in erosion and deposition, respectively (Figure 3.3).

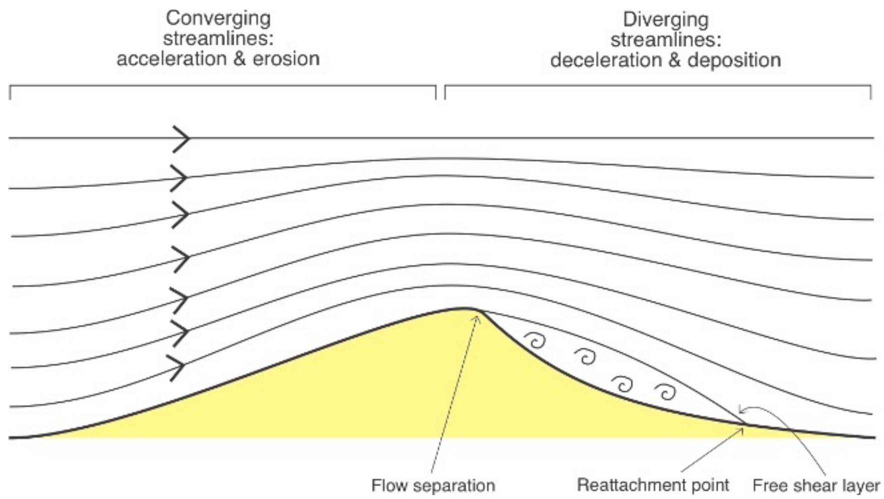

Figure 3.3. Flow streamlines over a topographical high (bed defect); streamlines converge and accelerate up the stoss side, causing erosion, and then separate from the bed near the crest. On the lee side streamlines diverge forming a separation bubble with sediment deposition.

A requisite condition for the development of angular bed forms is an initial bed defect. Traditionally such features are taken to be isolated negative or positive topographical features on the bed surface and then whose effect on local flow conditions spreads in an ever-widening area downflow (Williams & Kemp, 1971; Best, 1992). However, the common occurrence of ripple cross-stratified (Tc) sharply overlying planar stratified (Tb) sandstone indicates that ripples developed on a nominally flat-bed surface with negligible topographical relief. Experiments by Venditti et al. (2005) showed that bed defects can develop spontaneously and also everywhere on a flat bed. The origin of this spontaneous initiation was interpreted to be related to a hydrodynamic instability at the interface between the dense bed-load layer and the overlying, less dense and faster moving near-bed layer (Figure 3.4) (Venditti et al., 2006). The waveform instability organizes sediment transport patterns on the bed into a spatially regular pattern of erosion and deposition. Areas of deposition form the requisite bed defects that with the onset of flow separation causes the defect to amplify and ultimately evolve into a downflow-migrating angular bed form (Venditti et al., 2006, Tilston et al., 2015).

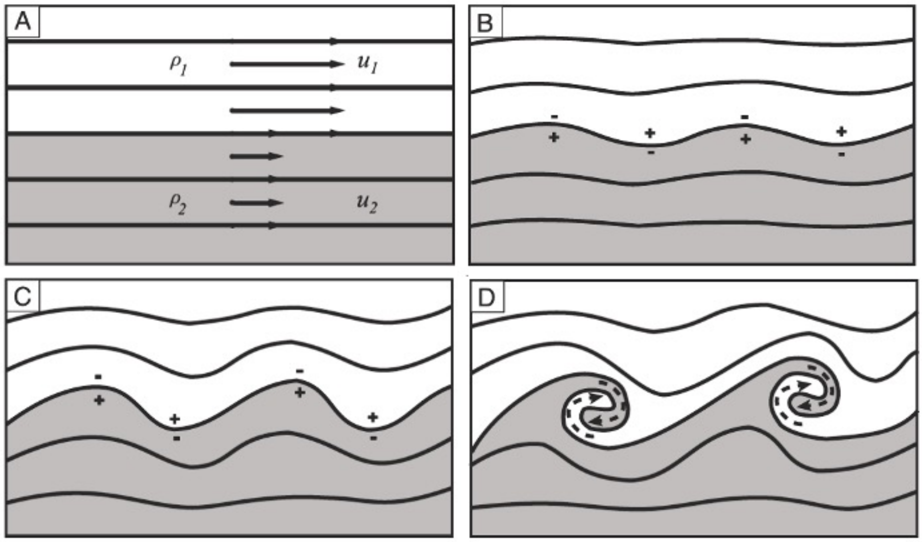

Figure 3.4. Development of a hydrodynamic Kelvin-Helmholtz instability at a density interface: velocity differences (A) between the less dense layer (white) and the denser layer (grey) causes convergence (acceleration) and divergence (deceleration) of streamlines, which in turn causes variations in pressure along the density interface (+ and – in B and C), ultimately resulting in the generation of waveforms (D) (Venditti et al., 2006).

Typically, planar laminated sandstone (Tb) is overlain by ripples (Tc) rather than dunes, though dunes are observed, albeit rare, in the study area. Explanations for the general lack of dune cross-stratification in the ancient and modern deep-marine record has long been debated by sedimentologists. Walker (1965), for example, proposed that turbidity current deceleration was too rapid for form dunes, whereas Allen (1970) attributed it to grain size of sediment on the bed being too fine. More recently, Arnott (2012) theorized and Tilston et al. (2015) showed experimentally that the development of the requisite near-bed hydrodynamic instability for the inception and amplification of incipient bed defects and development of ripples under a sediment-gravity flow (i.e., turbidity current) does not generally occur until flow speeds are within the ripple stability field. Moreover, Venditti et al. (2006) postulated that even when bed defects could be generated high sediment concentration in the near-bed layer caused the flow to remain hydraulically smooth and therefore favourable for the development of ripples rather than dunes.

Planar laminated and massive mud-rich strata of F2 are interpreted to be Bouma Td and Te division turbidites, deposited by rhythmically alternating bed-load traction and suspension-load fallout at the terminal stages of a decelerating turbidity flow and subsequent hemipelagic fallout (Stow & Bowen, 1980; Mulder & Alexander, 2001). Td and Te divisions typically occur together, or are undifferentiated, and commonly overlie the Tc division, though they have been observed to overlie Tb and Ta divisions indicating bypass conditions whereby the fine-grained Td and Te beds are deposited by the dilute tail of a highly efficient turbidity flow.

3.3 Facies F3 – Conglomerate

3.3.1 Description

3.3.1.1 F3A – Matrix-supported Conglomerate

F3A consists of poorly sorted, matrix-supported conglomerate (Figure 3.5A). Beds range from 11.5-1100 cm thick, but generally are between 300-832 cm thick. Basal contacts are erosive. Clasts consist of quartz granules and pebbles and up to boulder-size clasts of carbonate-cemented lower medium-grained sandstone dispersed in a dark-grey mudstone matrix. Rare sandy mudstone intraclasts are observed and are internally planar stratified. Clasts make up about 10% of the bed volume and are evenly distributed throughout the bed.

3.3.1.2 F3B – Clast-supported Conglomerate

F3B is a clast-supported, moderately to poorly sorted conglomerate separated into two end-member types based on matrix composition.

Clast-supported conglomerate with a mudstone to sandy mudstone matrix (Figure 3.5B) range between 8.5-217 cm thick, and average 100-200 cm. Basal contacts are sharp and erosive.

Strata consist of abundant quartz granules and granule- to pebble-sized clasts of carbonate-cemented, coarse- to medium-grained sandstone. Rarely, beds contain mudstone clasts that range from 2-10 cm long and 0.2-2 cm thick. Some ~ 10 cm-long sandy mudstone intraclasts are internally planar stratified.

F3B conglomerates with a sandstone matrix are composed of upper coarse- to medium-grained sandstone and range from 20-230 cm in thickness, averaging ~ 65 cm. Basal contacts are loaded (47%), planar (28%), or scoured (25%). Beds typically fine upwards to lower coarse- or medium-grained sandstone (Figure 3.5C), although ungraded beds are also observed (16%). Clasts are mostly quartz granules, but some beds (9.3%) contain abundant pebble quartz clasts. Mudstone clasts are common in 40% of F3B beds ranging 2-50 cm long, 0.5-6 cm thick, and typically are concentrated in the lower 11-44% of the bed, although in some beds mudstone clasts occur throughout.

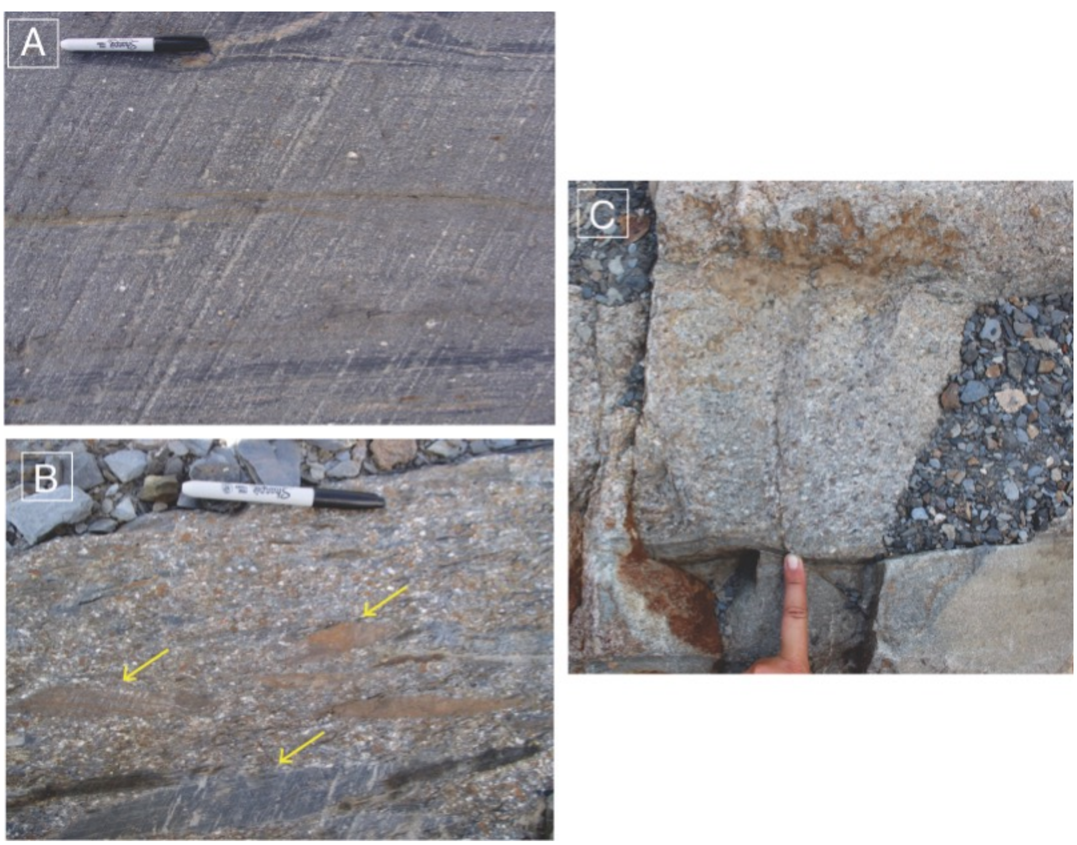

Figure 3.5. Facies F3. A) Matrix-supported F3A bed. Note silty mudstone matrix, dispersed granules, and elongated mudstone clast (bottom of photo). B) F3B bed with a silty mudstone matrix. From left to right yellow arrows indicate a planar-stratified intraclasts, mudstone clast, and a carbonate-cemented sandstone clast. C) Normally graded F3B bed with a sandstone matrix, granule conglomerate.

3.3.2 Interpretation

Due to the lack of internal structures, matrix-rich, and poorly sorted nature, F3A strata are interpreted to be deposits of cohesive sediment-gravity flows termed debris flows. Up to boulder-sized clasts were supported by cohesive strength provided by chemical bonding of clay-sized minerals in the fine-grained matrix, in addition to the effects of buoyancy, elevated pore pressure, and clast-to-clast interaction (Mulder & Alexander, 2001). Like F3A strata, clast-supported F3B strata with a mud matrix are also interpreted to be deposits of debris flows, and differ only in the abundance of clasts. Debris flows deposit *en masse* as shear resistance, controlled by fluid viscosity and grain-to-grain friction within the flow, overcomes the gravitational driving force and the flow freezes. More specifically, deposition results from the downward thickening of a negligibly sheared rigid plug that eventually comes to intersect the bed. Matrix strength maintains the plug-like structure by limiting mixing, and therefore dilution with the ambient fluid, and as a result the thickness of the deposit closely approximates the thickness of the parent flow (Mulder & Alexander, 2001; Arnott, 2010).

F3B strata with a sand matrix represent the deposits of hyperconcentrated density flows of Mulder & Alexander (2001). Hyperconcentrated flows are similar to cohesive flows; however the main particle support mechanism is grain-to-grain interaction rather than matrix strength, and their massive structure indicating frictional freezing as grains interlock (Mulder & Alexander, 2001). Lowe (1982) describes a similar deposit whereby gravelly high-density turbidity currents deposit gravel- to sand-size grains from suspension to form a graded conglomerate bed (R3). These flows may transform into low-density turbidity currents down-flow (Figure 3.6), indicating that R3 beds are deposited during bypass conditions (Lowe, 1982). Therefore, F3B conglomerates were likely deposited by a highly efficient, bypassing flow. Additionally, the common presence of mudstone clast breccias in the lower parts of F3B conglomerates suggests localized erosion of underlying fine-grained strata during bypass.

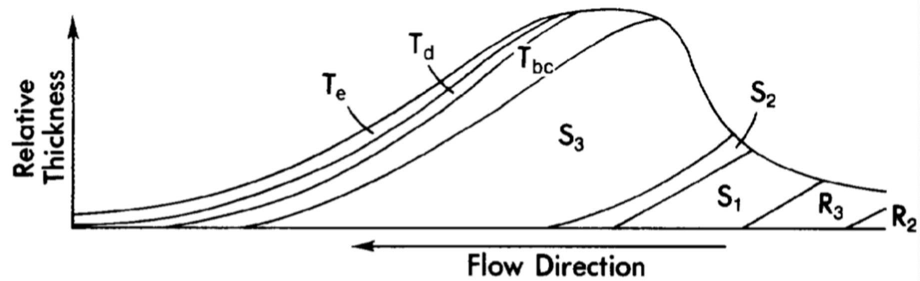

Figure 3.6. Schematic illustrating change in bed type (from gravelly, high density turbidity currents (R beds) to low-density turbidity currents (T beds)) and thickness as flow travels down slope (Lowe, 1982).

3.4 Facies F4 – Deformed Bedded Deposit

3.4.1 Description

Strata of F4 have sharp, erosive basal contacts and range from 0.79 - 7.5 m thick, but generally of the order of 3 – 7.5 m; three exceptionally thick units are 43, 47, and 79 m thick. In some cases, truncation of underlying beds is observed (Figure 3.7). F4 deposits can be laterally extensive (up to 1 km) and are characterized by the presence of large, sharply bounded blocks of coherent strata. Strata within these blocks exhibit minimal to no internal deformation and are recognized by their angular discordance compared to stratification in adjacent strata.

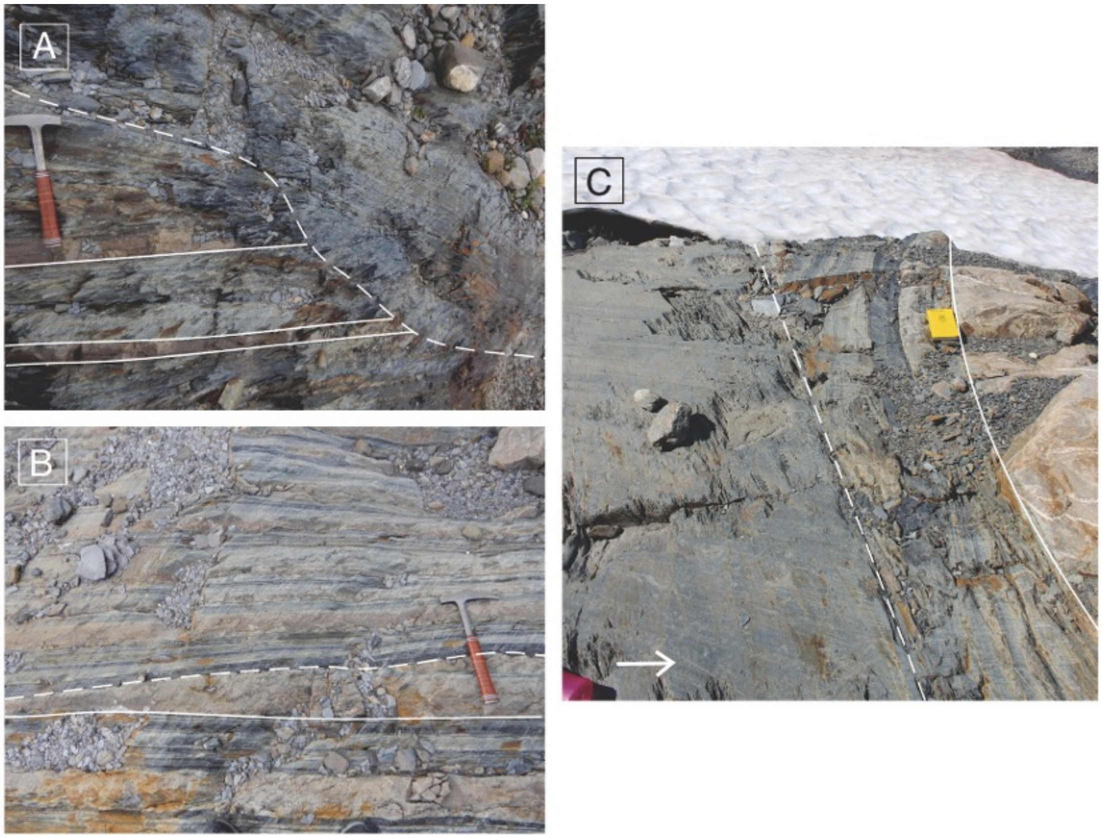

Figure 3.7. Erosion surface at the base of mass movement deposits (slide scars). Strata replaced by semi-coherent strata from upslope that exhibit minimal brittle and ductile deformation. A) Irregular-shaped slide scar (dashed line), solid lines indicate bedding plane of underlying strata. B) Planar slide scar (dashed lines) truncating underlying strata at an angle to bedding plane (solid line). C) Planar slide scar (dashed line) underlying minimally ductile-deformed slide block (note curved solid line); way-up indicated by arrow.

3.4.2 Interpretation

The scoured base and assemblage of discordant blocks in F4 deposits are interpreted to represent submarine slides: packages of semi-coherent strata that have been translated downslope resulting from an upslope failure of the seabed. Slide deposits are typically characterized by a mélange of discordant blocks bounded by failure planes that internally exhibit only minor internal deformation, and deposit *en masse* when friction at the base exceeds the gravitational driving force (Arnott, 2010). Regardless of where they originate, including at the shelf-slope break, on the slope, or on steep channel walls, slides are the result of slope-related gravitational instability triggered by one or more of a myriad of initiating mechanisms (Figure 3.8). For example, Moscardelli & Wood (2008) describe the emplacement of several Mass Transport Complexes (MTCs) in offshore Trinidad: high sedimentation rates from the shelf-edge delta overloaded the shelf and ultimately caused the failure that deposited MTC1, and the deposition of MTC2.1 was the result of tectonic activity that caused the upper slope to fail. They also note MTCs triggered by localized gravitational instabilities on the flanks of mud diapirs (Moscardelli & Wood, 2008). In addition, Haflidason et al. (2004) describe mass failure associated with the Storegga slide in Norway as a result of earthquake activity combined with increased pore pressure of a large volume of glacigenic sediments on the upper slope.

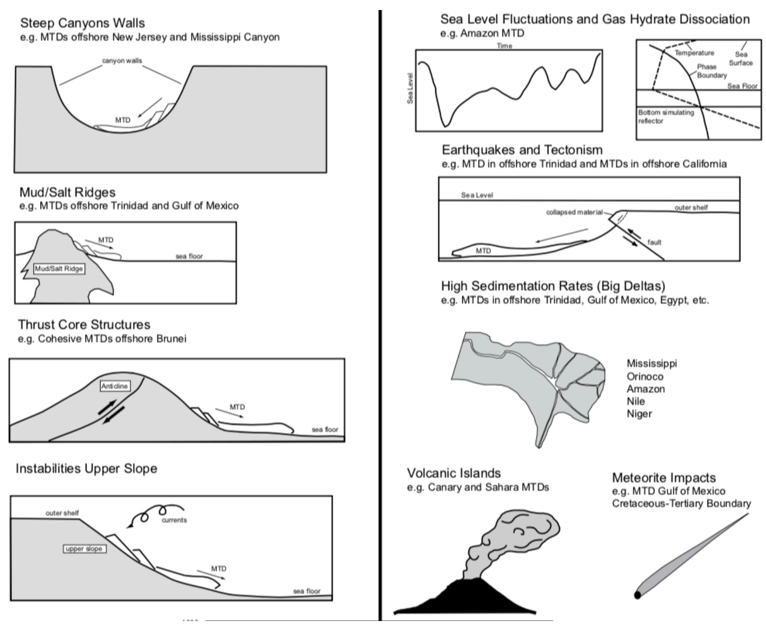

Figure 3.8. Cartoon of possible triggering mechanisms of detached (left pane) and attached (right pane) mass transport deposits following the classification scheme of Moscardelli & Wood, 2016.

Chapter 4: Architectural Elements

4.1 Overview

Architectural elements are defined as basic mappable geomorphic features that can be recognized in both modern and ancient outcrop and subsurface studies (Mutti & Normark, 1991). Identification of architectural elements allows for analysis and further understanding of depositional processes and changes in environmental parameters such as slope gradient and flow discharge (Posamentier & Kolla, 2003). In deep-marine turbidite systems, common elements include channels, levees, frontal splays, crevasse splays, and debris flows (Figure 4.0; Posamentier & Kolla, 2003).

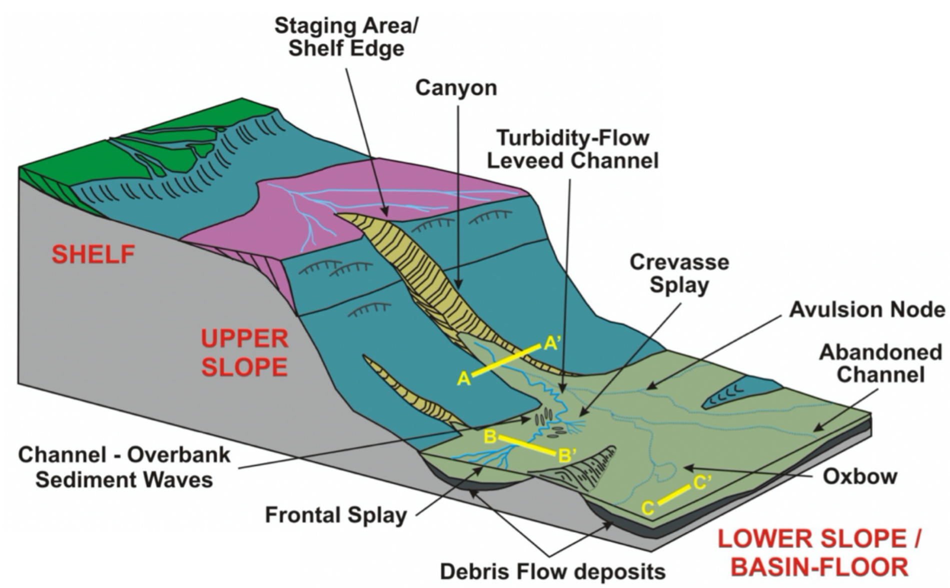

Figure 4.0. Spatial distribution of deep-marine architectural elements (modified from Posamentier & Kolla, 2003).

At the Castle Creek study area, three main architectural elements have been identified based on geometry and lithological composition: Channel, Overbank, and Mass Transport elements (Figure 4.1). Channel elements can be further subdivided into aggradational and laterally accreting elements; overbank into proximal levee, distal levee, and abandonment; mass transport elements into attached and detached. These elements comprise a ~ 4 km-wide and ~1 km thick succession and are described in the following sections.

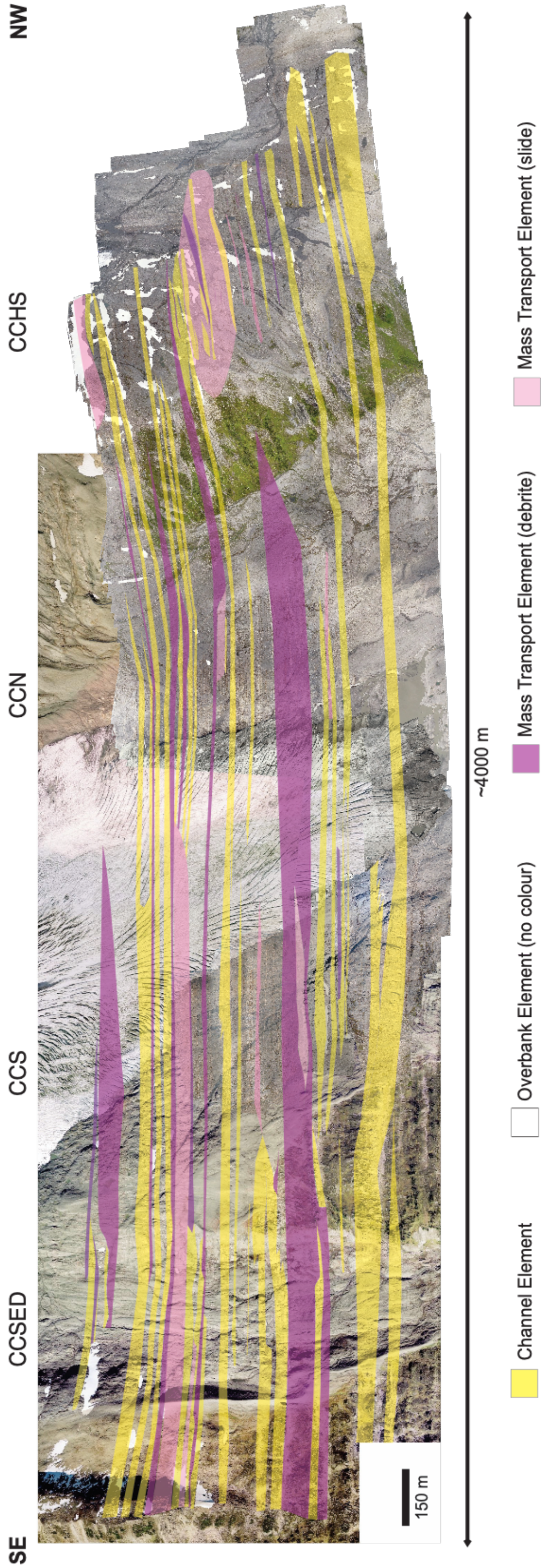

Figure 4.1. Correlation of architectural elements across the Castle Creek the study area.

4.2 Channel Element

4.2.1 Overview

Submarine channels act as conduits for sediment, nutrient, and organic carbon transfer from the continent to the basin. An equilibrium profile exists for a given set of flow conditions for a downslope-trending channel. Channel architecture is governed by accommodation (Figure 4.2A), defined as the space between the channel floor, or slope surface, and the equilibrium profile (i.e., the elevation to which sediment can aggrade; Kneller, 2003). Essentially, the equilibrium profile represents the amount of accommodation at a point in time for a given set of flow conditions and base level position, the lowest point to which a turbidity current can flow along a particular pathway (Kneller, 2003; McHargue et al., 2011).

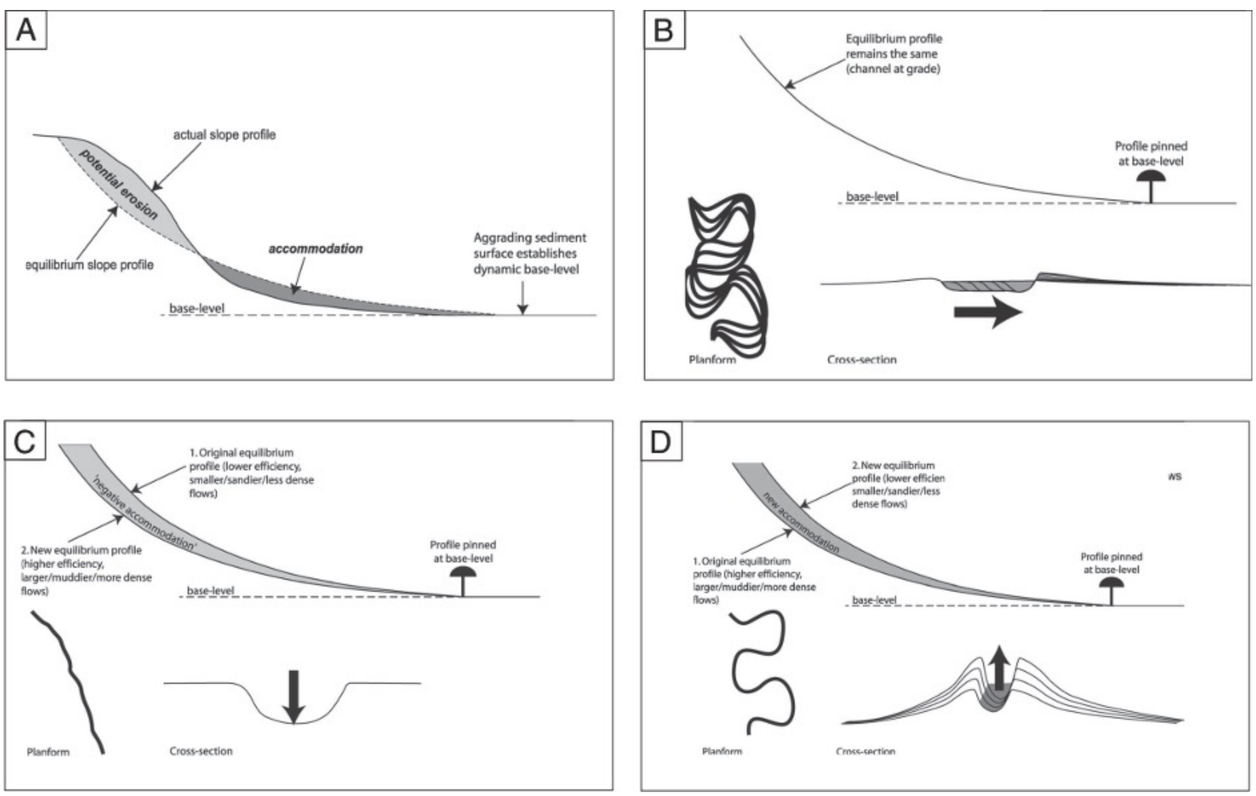

Figure 4.2. Equilibrium profiles for three sets of flow conditions with associated channel planform and cross-sections. A) General equilibrium profile showing potential erosion and accommodation on slope. B) Equilibrium profile is equal to the channel gradient, the channel is at grade. C) Channel gradient lies above equilibrium profile creating "negative" accommodation, that results in erosion occurs. D) Channel gradient lies below equilibrium profile creating accommodation, and therefore, deposition occurs (Kneller, 2003 modified by Fraino, 2020).

Where the channel gradient (actual slope profile) and equilibrium profile are similar the channel is considered at grade, with neither erosion nor deposition as sediment bypasses further downslope (Figure 4.2B). These channels are considered graded or neutral and no accommodation is created (Kneller, 2003). Graded channels are typically initially straight but then evolve toward a steady-state sinuosity, forming a series of laterally migrating channels that resemble those in continental meandering fluvial systems (Kneller, 2003). When flow conditions are such that the equilibrium profile flattens below the channel gradient (increase in flow size or density, or reduction in grain size), "negative" accommodation is created on the slope resulting in erosion until the channel gradient is once again at grade (Figure 4.2C). These erosional channels are commonly straight or low sinuosity negative features (Kneller, 2003; Arnott, 2010). Aggradational channels form when the equilibrium profile steepens (i.e., accommodation is created) in response to an increase in grain size or a reduction in flow magnitude such that the channel must deposit sediment to increase the slope gradient and maintain sediment in suspension (Figure 4.2D). Deposition on channel-bounding levees is required to maintain confinement of the channel, and the channel itself is characterized by a "cut and fill" morphology with a steep angle of climb reflecting rates of aggradation that exceed lateral migration (Kneller, 2003). Mixed channels exhibit erosion in the channel axis and aggradation on the levees (Arnott, 2010). Overall channel architecture, therefore, is determined by changes in flow conditions that typically are reflected by the long-term evolution of an erosive straight conduit to a sinuous laterally migrating channel to an aggradational channel (Mayall et al., 2006). Channel evolution from erosive to aggradational is commonly interpreted to be a consequence of relative sea level rise and changes in flow competence and granulometric properties that can be described in a sequence stratigraphic context. During relative sea level fall (falling stage systems tract, FSST) sand:mud ratio is initially low and the flow is highly efficient, dense, and fine-grained. Here, the equilibrium profile is relatively flat and the channel is erosive. As relative sea level reaches its minimum (lowstand systems tract, LST) sand:mud ratio and grain size increase and reduces flow efficiency. At this point, reduced flow efficiency promotes net deposition and a steepening of the equilibrium profile. During transgression (transgressive systems tract, TST), sand:mud ratio progressively decreases as coarse sediment becomes increasingly sequestered on the expanding shelf and in more landward environments. These changes result in enhanced levee growth and aggradation of the channel, which persists until relative sea level reaches is highest during the highstand systems tract and turbidity current activity effectively ceases and the channel is deactivated.

Fluvial and submarine channels are geomorphologically similar in planform however submarine channels are an order of magnitude wider and deeper than their fluvial counterparts (Konsoer et al., 2013). Additionally, differences in channel migration and aggradation rates are related to fundamental differences between fluid-gravity flows (i.e., rivers) and sediment-gravity flows (i.e, submarine channels) (Wynn et al., 2007). The reduced density difference in submarine systems (between the flow and the ambient fluid) enhances superelevation of the flow as it travels around a bend, resulting in more significant overbank deposition than in rivers (Piper & Normark, 1983; Wynn et al., 2007). This can result in submarine channels being highly confined by levees that hinder lateral migration but encourage channel aggradation – a condition very different compared to meandering river systems. In the fluvial realm, sinuous channels are commonly associated with lateral point-bar accretion on the inner bend of the channel (scroll bars). In a series of flume and modelling experiments, Van de Lageweg et al. (2014) showed that scroll bar formation is a result of channel widening through outer bank erosion and consequent deposition of the inner bank. They posit that point bar deposits are built up by multiple scroll bars as the river continuously erodes the outer bank and migrates down flow, creating the characteristic “swing and sweep” morphology (a combination of lateral and down-flow migration) of meandering rivers that is much less commonly observed in deep-marine channels (Figure 4.3, Van de Lageweg et al., 2014).

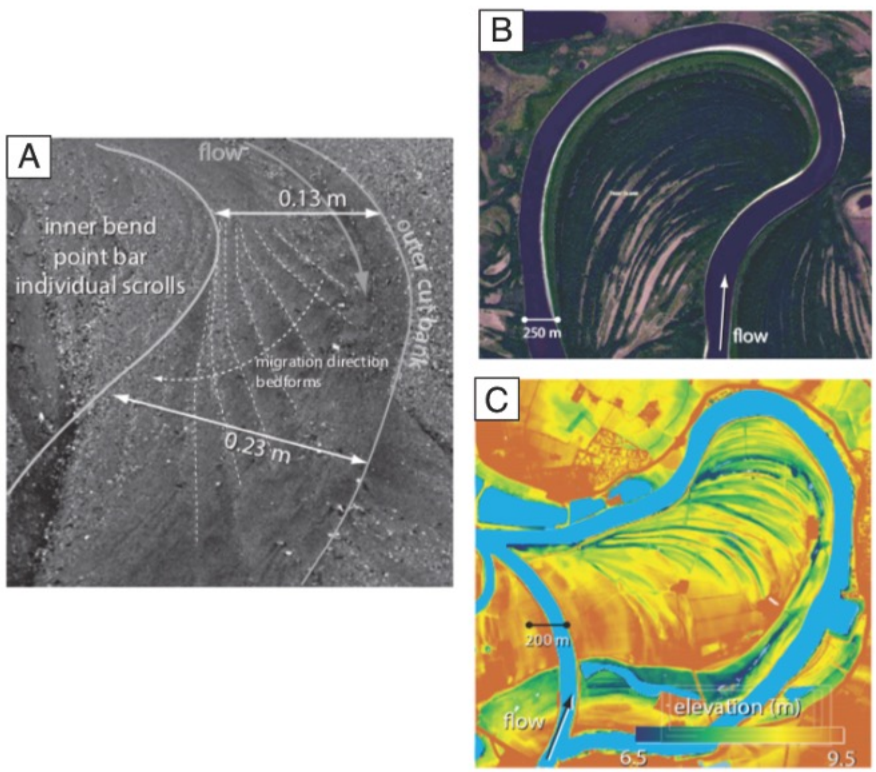

Figure 4.3. A) Scroll bar formation in a flume. Obliquely migrating sheets shoal onto the point bar surface as flow rounds the bend; a single scroll is composed of several migrating sheets (van de Lageweg et al., 2014). B) and C) Scroll bars of meandering rivers (Koyukuk River, Alaska, and Ijssel River, Netherlands; van de Lageweg et al., 2014).

Although submarine channels commonly exhibit a sinuous planform, examples of laterally accreting channel fills are rare compared aggradationally filled channels (Arnott, 2007).

In the Green Channel Complex in offshore Angola, Abreu et al. (2003) interpreted shingled seismic reflections to represent lateral and downdip migration of channels. These discrete, accretionary bodies were termed Lateral Accretion Packages (LAPs) and interpreted to have been deposited on the inner bend of the channel (Abreu et al., 2003). However, Arnott (2007) pointed out that the scale of LAPs are more than an order of magnitude larger than those observed in his end-member types of inner bend deposits, termed coarse- and fine-grained Lateral Accretion Deposits (LADs), and that LAPs record successive, laterally offset channel fills rather than the lateral migration of single channels. LADs, as described by Arnott (2007), are on the scale of metres in thickness and in lateral spacing, and therefore below the seismic resolution of LAPs. Fine-grained LADs are interpreted to be deposited when the channel is at grade and bypass conditions prevail. Disruption of the system such as failure of cut bank creates positive accommodation and, as the flow expands through the widened channel, flow capacity decreases and deposition of coarse-grained LADs occurs on the lateral-accretion surface (Figure 4.4; Arnott, 2007). Thus, Arnott (2007) postulated that lateral accretion is a result of repeated periods of bypass followed by deposition, demonstrated by consistent interfingering of fine- and coarse-grained LADs in outcrop.

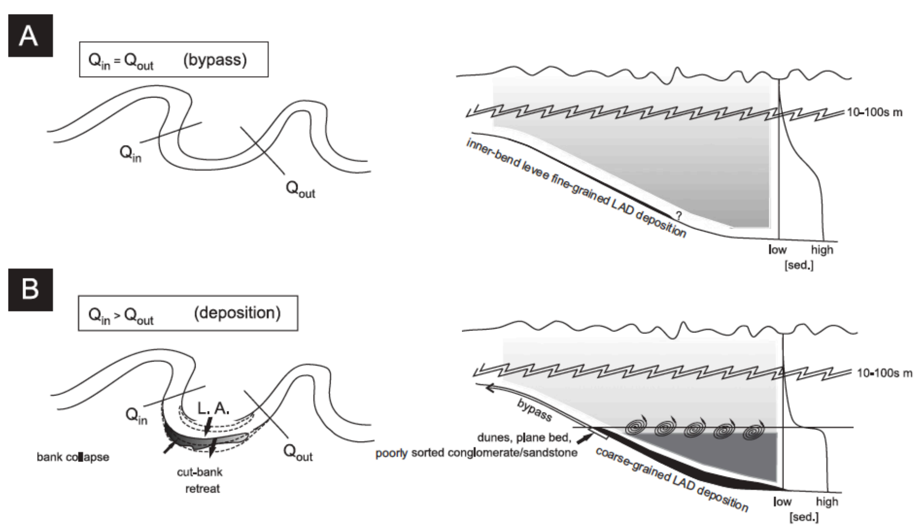

Figure 4.4. Deposition on inner bend of laterally accreting channels (LADs). A) Bypass conditions, fine-grained LADs deposit on inner bend. B) failure of cut bank widens channel and flow expansion results in deposition of coarse-grained LADs on inner bend (Arnott, 2007).

Channel complexes typically exhibit a two-phase evolution of channel trajectory beginning with lateral migration followed by aggradation and reduced lateral migration (Figure 4.5; McHargue et al., 2011; Jobe et al., 2016). McHargue et al. (2011) argued that channel organization is controlled by remnant channel element relief, whereby poorly confined (low relief) channels that fill or almost fill the channel element result in a disorganized stacking pattern, as the small amount of remnant relief has little effect on the pathway of subsequent flows. Underfilled channels, on the other hand, are confined by high rates of levee aggradation that outpaces channel aggradation. This results in an organized channel stacking pattern whereby significant remnant channel relief guides the path of later flows and results in a systematic lateral-offset architecture of successive channels. In their model, McHargue et al. (2011) predict that as flow wanes at the complex-set scale there will be a tendency to develop an organized stacking pattern as the flow becomes more mud-rich and levee growth is enhanced. Thus, a transition from a disorganized to organized stacking pattern is expected in the temporal evolution of a channel complex set.

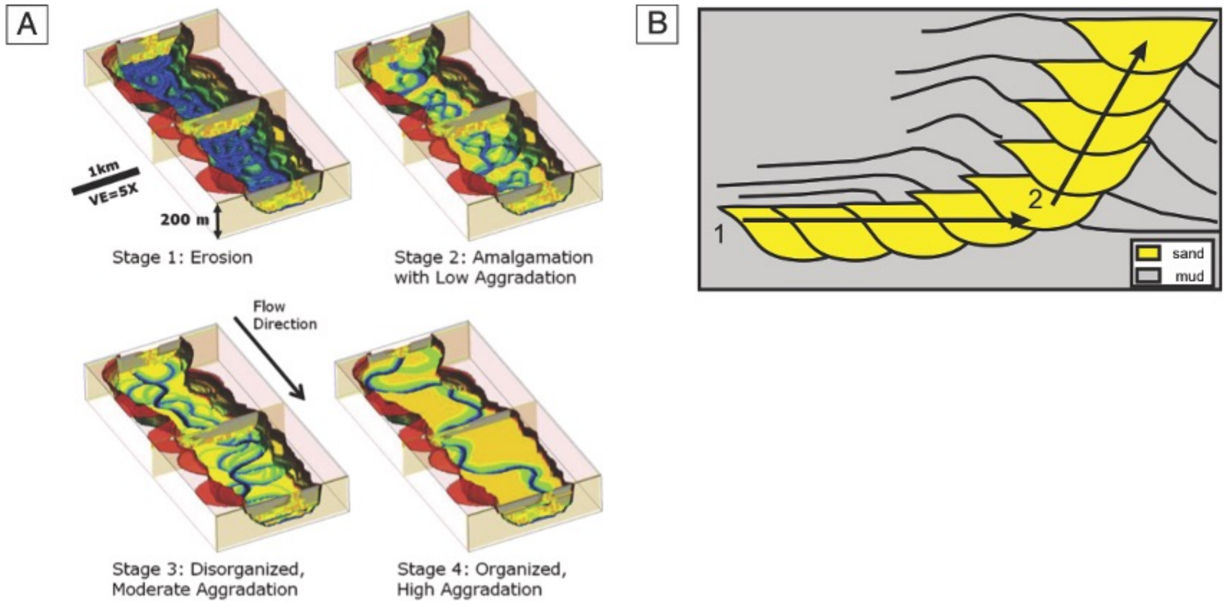

Figure 4.5. Evolution of submarine channel architecture and stacking patterns. A) Stage 1 illustrates point of maximum valley erosion (blue represents deepest areas). Stage 2: low rates of aggradation and channel amalgamation. Stage 3: moderate rates of aggradation leads to a disorganized stacking pattern. Stage 4: high rates of aggradation with an organized stacking pattern (McHargue et al., 2011). B) Evolutionary model of channel architecture from an initial stage of lateral migration followed by significant aggradation with minor lateral migration (Jobe et al., 2016 modified by Fraino, 2020).

This paper uses the channel classification hierarchy of Navarro (2006) (Figure 4.6) that describes the make-up of a channel system in terms of a set of two-dimensional physical parameters. An individual *channel fill* is typically < 10 m deep with a preserved length up to 200 m long. Channel fills are defined as negative relief geomorphic features in which turbidity currents are mostly confined and move downslope (Mutti et al., 2000). Two or more channel fills comprise a *channel unit*, and two or more channel units make up a *channel complex*. A *channel complex set* comprises two or more channel complexes, and accordingly a *channel system* consists of two or more genetically related channel complex sets.

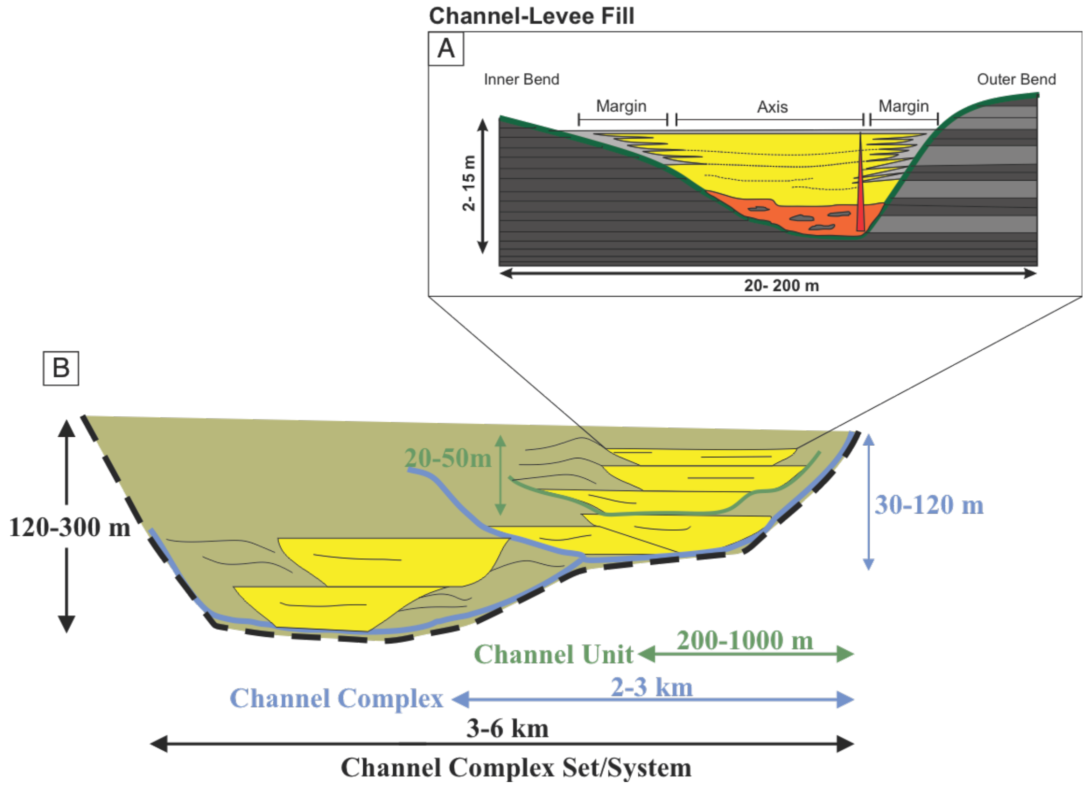

Figure 4.6. Channel hierarchy classification of Navarro 2005 (modified by Fraino 2020).

4.2.2 Aggradational Channel Elements

Table 4.1. Aggradational Channel Elements at Castle Creek were described in detail by the following authors whose descriptions are used herein.

AGGRADATIONAL CHANNEL ELEMENT(S)	AUTHOR(S) AND YEAR PUBLISHED/COMPLETED
ICC1 LC, UC1, UC2	- Navarro (2006) - Fraino (2020)
IC3L-C1 TO C3, IC3U-C1	- Navarro (2006) - Navarro, Khan, & Arnott (2006) - Huyer (2016)
IC4.1 TO 4.3	- Mussa-Caleca (2008) - Ruso (this study)
ICC4B	- Ruso (this study)
ICC4.5.1 TO 4.5.5	- Bergen (2017)
IC5.1, 5.2, 5.3-1 TO 5.3-3	- Schwarz & Arnott (2007a,b)

4.2.2.1 Aggradational Channel Elements – Descriptions

4.2.2.1.1 Isaac Channel Complex 1 – LC, UC1, UC2

Isaac Channel Complex 1 comprises four vertically stacked channel units termed the Lower (LC) and three Upper channel units (UC1, UC2, UC3) (Figure 4.7A). ICC1 is up to 220 m thick and LC and UC are 30 and 90 m thick, respectively. LC is composed of three erosively based channel fills (LC-C1 to 3) that are 10-15 m thick. Notably, LC-C1 consists of quartz pebbles and abundant carbonate-cemented sandstone and mudstone clasts; these strata are not observed in LC-C2, LC-C3, UC1, or UC2. Channel fills in LC are amalgamated, thick-bedded, coarse-grained sandstones that, stratigraphically upwards and laterally, fine and thin and are progressively more interbedded with thin- to medium-bedded upper division turbidites.

UC1 is up to 62 m thick and sharply overlies thin-bedded, fine-grained upper division turbidites that separates LC from UC. Channel fills exhibit scoured bases and are composed of amalgamated, thick-bedded, coarse- to very-coarse grained sandstone and minor granule conglomerate. Strata of UC1 exhibit a lateral transition into medium-bedded, medium-grained upper division turbidites but show negligible upwards change in facies (Figure 4.7B-C). UC2 is 25 m thick and is comprised of at least four channel fills (5-10 m thick) with scoured basal contacts. Channel fills in UC2 are composed of coarse-grained sandstone that fine and thin upwards and laterally, and are capped with medium-bedded, fine-grained upper division (Tbde) turbidites.

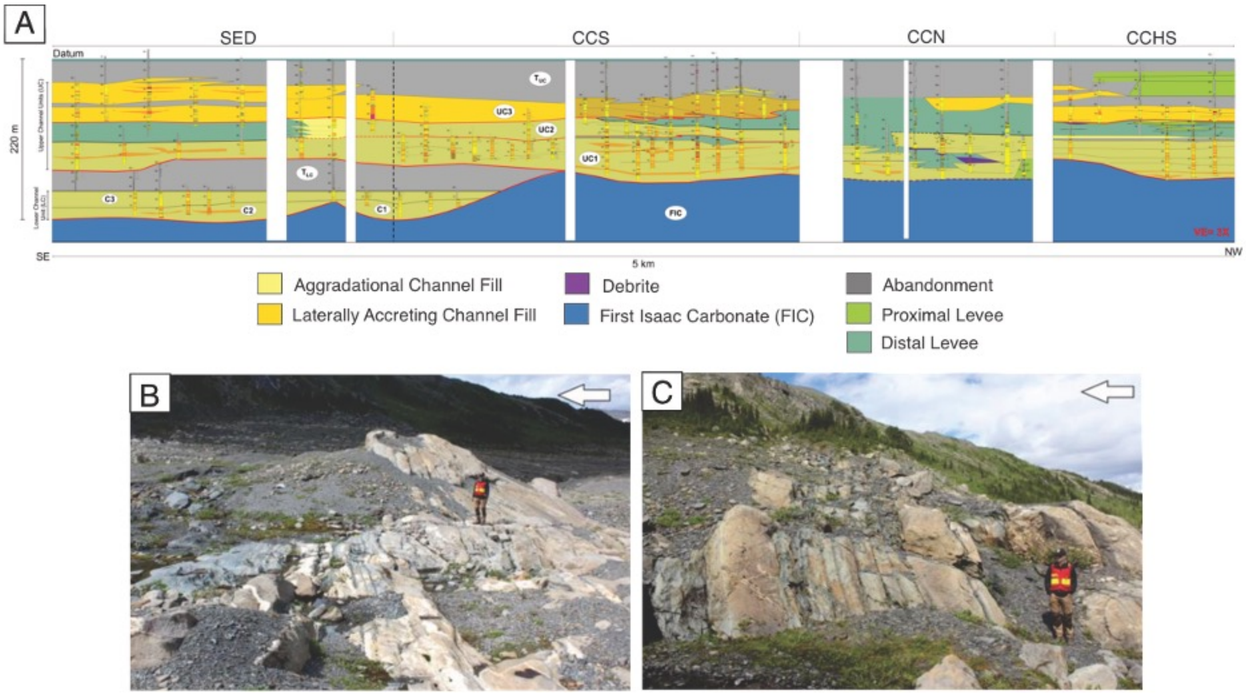

Figure 4.7. A) Correlation panel of Isaac Channel Complex 1. Channel and associated overbank units are labelled in white circles (modified from Fraino, 2020). B-C) Example of the lateral transition of amalgamated, thick-bedded, coarse-grained sandstone (B) to non-amalgamated, thick-bedded coarse-grained sandstone and medium-bedded, fine-grained upper division turbidites (C). Photos from Fraino (2020).

4.2.2.1.2 Isaac Channel Complex Set 3 – IC3L-C1 to C3 and IC3U-C1

Isaac Channel Complex Set 3 comprises an upper and lower channel complex termed IC3L and IC3U (Figure 4.8). IC3L is then subdivided further into four channel units (IC3L-C1 to C4) and IC3U into two (IC3U-C1 to C2).

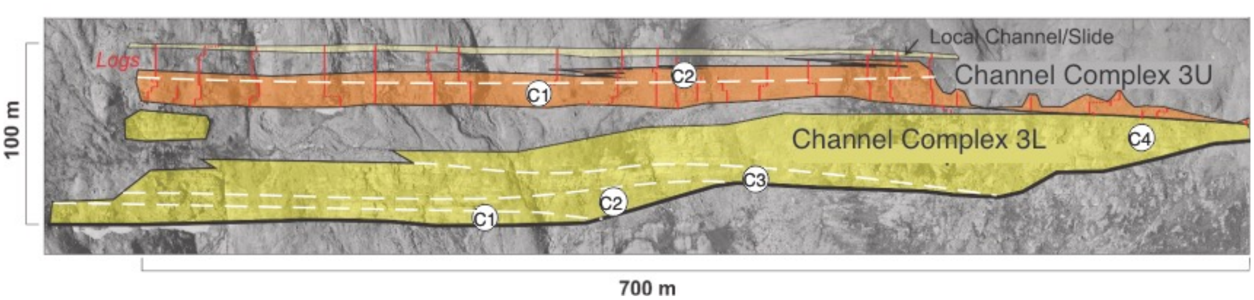

Figure 4.8. Architecture of Isaac Channel Complex 3 (modified from Huyer, 2011). IC3L is shaded in yellow and IC3U in orange. Channel units within each complex are labelled in white circles.

IC3L and IC3U-C1 make up an ~ 100 m-thick and 1 km-wide succession of vertically stacked channel complexes. IC3L overlies, and in some places incises into, an up to 90 m-thick, carbonate-rich debrite, and on both sides is bound by genetically related levees (Khan, 2012). The base of IC3L is more or less horizontal but on its northwest margin forms a "stepped" geometry characterized by a flat-riser profile. Channel unit bases are erosive with local deep scours (up to 12 m). A pebble conglomerate with dispersed carbonate clasts makes up C1 and is locally overlain by mudstone-clast breccia. An up to 8 m-thick mudstone-clast breccia overlies the base of C2 and locally C3. There is an axis-to-margin transition from amalgamated sandstone that fine and thin to thin- to thick-bedded, lower division turbidites and then to thin- to medium-bedded upper division turbidites. The uppermost channel unit (C4) is characterized by an extensive erosional surface that scours into C3 towards the channel axis. Notably, the base of C4 is marked by a 3 m thick inclined succession of partially amalgamated massive sandstone and mudstone clast breccia interbeds, however towards the margins the channel fills interfinger with adjacent fine-grained strata like the majority of channel fills in IC3L.

IC3U-C1 is an ~ 20 - 25 m-thick channel unit at the base of IC3U and is exposed over ~ 500 m. The basal 3 - 5 m of C1 consists of amalgamated, coarse- to very coarse-grained, thick- and medium-bedded sandstone that upwards become progressively more interstratified with thin- to very thin-bedded fine-grained turbidites. Channel fills consist of amalgamated, thick-bedded, normally graded granule to medium-grained sandstone. Mudstone clasts are common at the base of individual channel fills, whereas at the top strata are commonly planar stratified. Local interbeds of thin-bedded, fine-grained, upper division turbidites are common and are up to tens of cm thick. Rare occurrences of dune-scale cross-stratified and matrix-rich sandstone are observed.

4.2.2.1.3 Isaac Channel Complex Set 4 – IC4.1, 4.2, 4.3

Isaac Channel Complex Set 4 (ICC4) is composed of four channel complexes (IC4.1 to 4.4). In Castle Creek South (CCS), IC4.1, 4.2, and 4.3 crop out in the lower part of ICC4 and is ~ 84 m thick. IC4.1 thins from 32 m to ~ 5 m towards the northwest due to erosion at the base of IC4.3. Channel fills in IC4.1 have erosive bases and are dominated by amalgamated, thick-bedded coarse-grained sandstone and conglomerate but stratigraphically upwards interbeds of fine-grained sandstone and silty mudstone become more common. IC4.2 erosively overlies IC4.1 and is 25 m thick. In outcrop it extends for ~ 600 m along strike before being truncated by IC4.3. Channel fill lithology is similar to that of IC4.1, however mudstone-clast breccia is common at the base of individual channel fills. IC4.3 is 27 m thick and in its lower part channels are dominantly amalgamated, thick-bedded quartz pebble conglomerate and mudstone-clast breccia. Stratigraphically upward through IC4.3, interbeds of thin-bedded, coarse- to medium-grained sandstone and silty mudstone become increasingly more common.

In the Hill Section (CCHS) ICC4 is made up of a single ~17 m thick channel unit (HS-IC4.1, Figure 4.9), sharply overlies an up to 170 m-thick mass transport deposit (MTD 3; see MTD Element discussion below). HS-IC4.1 spans the entire width of the outcrop (~ 600 m) and varies little in thickness (+/- 5 m) before being covered by moraine on both sides. HS-IC4.1 comprises three channel fills (2 - 4 m thick) and thins from ~ 17 m to ~ 13 m towards the northwest. In the northwest, an ~ 5 m thick unit of planar laminated sandstone overlain by fine-grained, thin- to medium-bedded upper division turbidites sharply overlies the slide; the contact is covered in the southeast. It is composed of very thick-bedded, massive and normally graded, granule conglomerate and very coarse-grained sandstone that laterally (towards the northwest) fine and thin to thick-bedded, normally graded, coarse- to medium-grained sandstone interbedded with thin-bedded, traction-structured sandstone and mudstone beds (Tabcd turbidites).

Figure 4.9. Three channel fills (dashed lines indicate basal contacts) of HS-IC4.1. Top and bottom contacts of channel unit indicated by solid line (arrow indicates stratigraphic up). Channel fills amalgamate towards the southeast (top of photo) and fine and thin towards the northwest (bottom of photo). Field assistant for scale.

4.2.2.1.4 Isaac Channel Complex 4B

Isaac Channel Complex 4B (ICC4B) is ~ 30 m thick and crops out only in SED and CCHS. In SED, ICC4B erosively overlies a 10 m-thick succession of thin-bedded, fine-grained, upper division turbidites and comprises two channel fills that range from 7-13 m in thickness. The base of ICC4B is characterized by coarse-grained sandstone with abundant quartz and feldspar pebbles and carbonate-cemented sandstone and mudstone clasts (Figure 4.10). Channel fills are composed of amalgamated, thin- to very thick-bedded, medium- to coarse-grained sandstone with granules and pebbles. To the northwest, ICC4B is bound by genetically related levees.

Figure 4.10. Base of ICC4B in SED containing abundant quartz pebbles, carbonate-cemented sandstone and limestone clasts. Photo from Terlaky (2016).

In CCHS, ICC4B comprises three channel units termed IC4B.1 to IC4B.3 that range in thickness from 1.72 m to ~ 18 m. The base of ICC4B is characterized by a pebble conglomerate horizon that onlaps positive topography created by the slide to the northwest and sharply overlies ICC4 to the southeast (Figure 4.11A). IC4B.1 ranges between ~ 6.5 m to ~ 2 m in thickness and comprises two channel fills of thick-bedded, massive granule conglomerate to coarse-grained sandstone beds. Bases are loaded and overlain by abundant mudstone clasts (Figure 4.11B). Laterally towards the northwest, beds are composed of thick-bedded, normally graded, granule conglomerate and medium-grained sandstone that grade upwards to fine-grained, planar-laminated sandstone and thin-bedded mudstone caps. IC4B.2 is up to ~ 8 m thick and onlaps a 4 m-thick debrite in the northwest before pinching out. Two channel fills (~ 3.5 m thick) are identified in this unit and consist of thick- to very thick-bedded, normally graded, granule conglomerate to coarse-grained sandstone and subordinate medium-grained, planar-laminated sandstone. Towards the northwest, medium-grained, planar-laminated sandstone and mudstone interbeds become more common. Further along strike (to the northwest) and beyond the debrite, strata are dominated by thin-bedded, upper division turbidites (Tcd) that likely represent levee deposits related to ICC4B. The uppermost channel unit (IC4B.3) comprises at least two channel fills that pinch out towards the northwest. The bases of the channel fills are composed of granule conglomerate with mudstone intraclasts, and the fills consist primarily of thick bedded, very coarse-grained to medium-grained, normally graded sandstone. Mudstone-clast breccia units are common at the bases of beds. No prominent upward change in grain size is observed, however towards the northwest coarse-grained beds interfinger with thin-bedded, fine-grained, planar laminated and ripple cross-stratified sandstone and mudstone beds. Overall, in ICC4B mudstone-clast breccia and granule conglomerate are common in the southeast but become progressively less so towards the northwest where interbeds of medium- to thick-bedded, medium- to fine-grained, parallel- and ripple cross-stratified sandstone and mudstone are more abundant (Figure 4.11C-D).

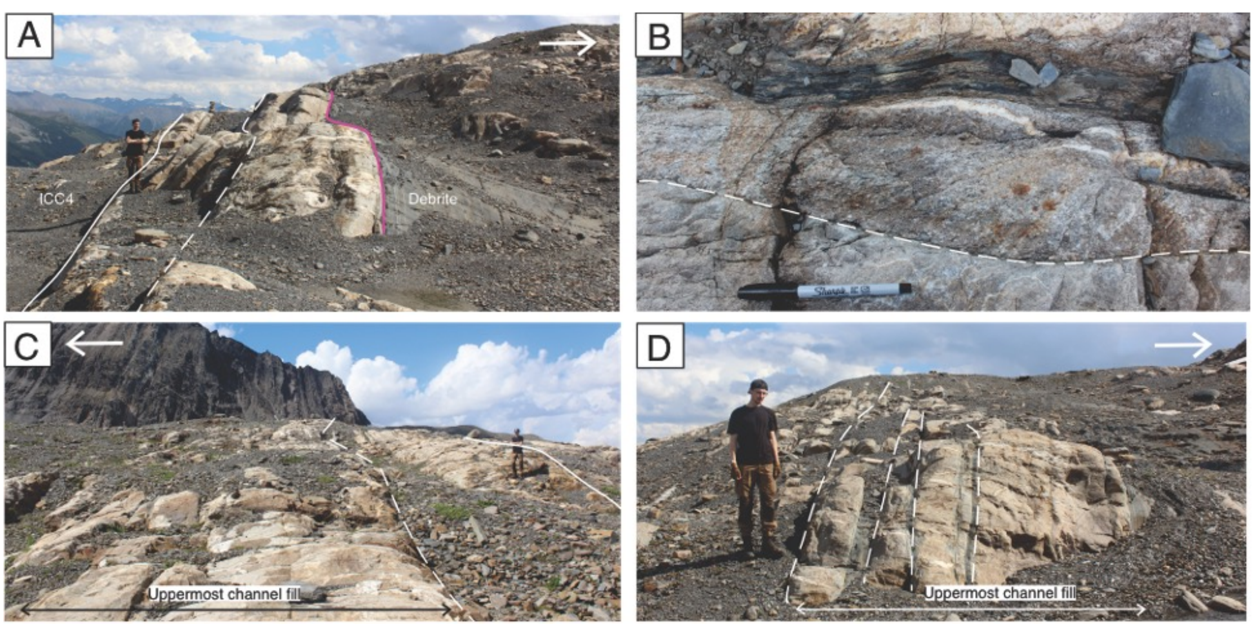

Figure 4.11. Isaac Channel Complex 4B. A) Base of ICC4B.1 and contact of ICC4B with ICC4 (solid white line). Thick purple line indicates contact with overlying debrite onto which IC4B.2 onlaps. B) Granule conglomerate and mudstone clast breccia that characterizes bases of channel fills. Sharpie is 13 cm. C-D) Uppermost channel fill of ICC4B.3 looking towards the northwest (C) and southeast (D). Channel fills exhibit a lateral transition from mostly amalgamated, thick-bedded structureless sandstone beds (T_a) to non-amalgamated, medium-bedded traction structured sandstone and siltstone beds (T_a, T_{bcde}). Field assistant for scale.

4.2.2.1.5 Isaac Channel Complex 4.5

Isaac Channel Complex 4.5 (ICC4.5) is approximately 110 m thick and extends along strike for ~ 900 m in the southeasternmost part of Castle Creek (SED) (Figure 4.12). ICC4.5 erosively overlies a 0.5-12.6 m-thick debrite (D1 of MTD 4, see Mass Transport Elements discussion below) and comprises three channel units (IC4.5.1 to IC4.5.3) that range from 8 - 25 m thick. To the north of SED, all three channel units are bound by genetically related levee deposits. The channel units are each made up of two channel fills that at their base consist of amalgamated, thick-bedded, upper coarse- to medium-grained, lower division turbidites (Ta) with local mudstone-clast breccia that then grade upward to thin-bedded, fine-grained, upper division turbidites. Overall, ICC4.5 exhibits a general upward and lateral (towards the northwest) fining trend.

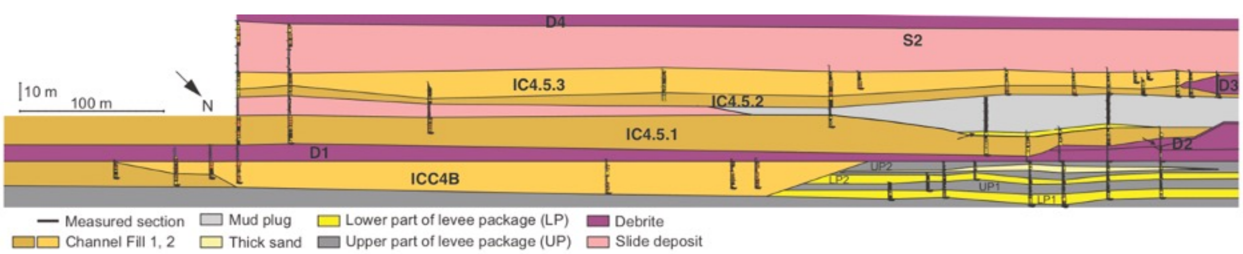

Figure 4.12. Correlation panel of ICC4.5 in SED modified from Bergen et al. (accepted).

4.2.2.1.6 Isaac Channel Complex Set 5 – IC5.1, 5.2, 5.3-1 to 5.3-3

Isaac Channel Complex Set 5 (ICC5) is exposed across 3.5 km and thins from 100 m to 75 m towards the northwest. It comprises three channel complexes (IC5.1-5.3, Figure 4.13A) that range from 8 - 30 m thick. ICC5 is bound above and below by > 25 m-thick mudstone units, and each channel complex is separated by units of thin-bedded, fine-grained strata. Channel fills of IC5.1, IC5.2 and IC5.3-1 to 5.3-3 are 3 - 12 m thick, sharp-based, and dominated by amalgamated, thick-bedded, coarse-grained, normally graded sandstone (Figure 4.13B) and pebbly conglomerate with uncommon thin-bedded, fine-grained interbeds. Some beds are parallel laminated in their uppermost part with mudstone clasts near their base, but both are uncommon. Towards the channel margin beds typically thin and onlap onto a basal erosion surface.

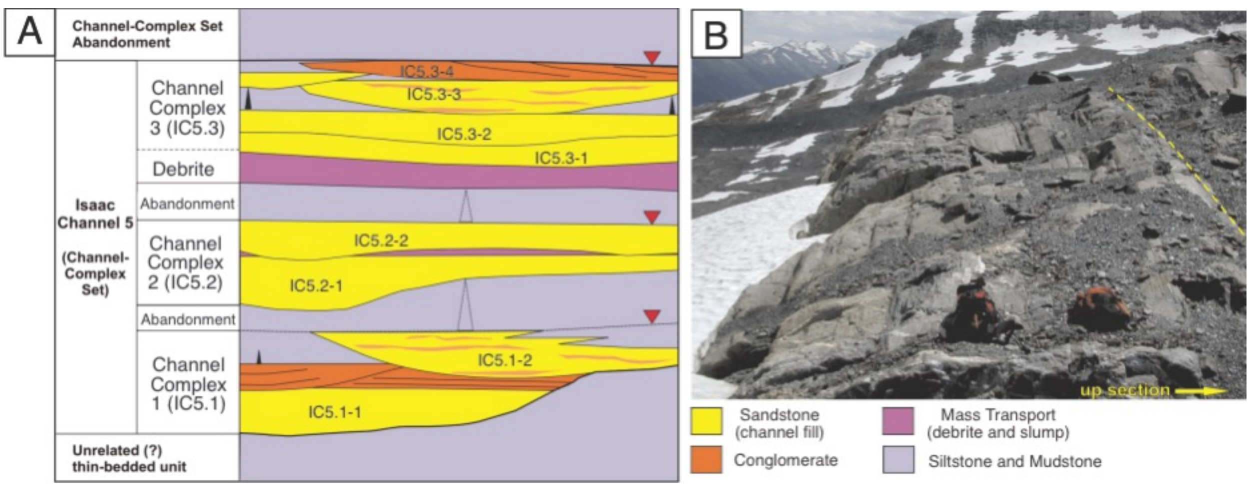

Figure 4.13. A) Architecture of ICC5 (modified from Schwarz and Arnott, 2007a,b). B) Amalgamated, thick-bedded, coarse-grained sandstone channel fills of IC5.1-1. Backpacks for scale, photo from Schwarz and Arnott (2007a,b).

4.2.2.2 Aggradational Channel Elements – Interpretation

The commonality of erosive basal contacts combined with overlying mudstone-clast breccia units are interpreted to represent repeated phases of channel incision and bypass from high-energy turbidity currents. Thick beds of amalgamated, coarse-grained sandstone and conglomerate at the base of fills suggests deposition in the channel axis by highly efficient, sand-rich flows. Mudstone clasts are commonly observed in these coarse-grained deposits and are interpreted to be rip-up clasts, as flows eroded fine-grained sediments deposited from the dilute tails of previous flows or during channel inception as erosive flows carved out a channel-form. Stratigraphically upwards grain size and bed thickness typically fine and thin and traction sedimentary structures become increasingly more common suggesting a progressive decrease in flow magnitude and competence. The axis-to-margin trend of amalgamated, thick-bedded, coarse-grained sandstone into thin- to thick-bedded, coarse-grained sandstone interbedded with thin- to medium-bedded, upper division turbidites is interpreted to represent the lateral transition from channel axis (thalweg) to channel margin (Figure 4.14). In a synthesis of key turbidite facies Mayall et al. (2006) described a similar trend where channel axis deposits are dominated by thick, amalgamated sandstone beds and towards the channel margins more thinly interbedded sandstone and mudstone beds dominate (Figure 4.14). Eventually channel abandonment results in a channel that is partly or completely filled with fine-grained sediment either from the dilute tail of the final flow through the channel before upstream avulsion or as relative sea level rises and coarse clastic sediment input is reduced (Clark & Pickering, 1996; Mayall et al., 2006).

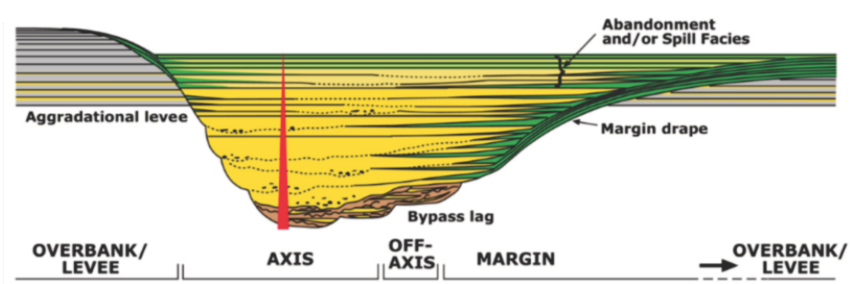

Figure 4.14. Cartoon illustrating lateral facies change characteristic of aggradational channel elements: axial deposits are amalgamated, thick-bedded, and coarse-grained and become increasingly interbedded with medium- to thin-bedded sandstone and mudstone towards the channel margin (McHargue et al., 2011).

Similar aggradational channel elements are described by Macauley and Hubbard (2012) in their Channel Complex 2, Tres Pasos Formation, Chile. Channel Complex 2 is composed of amalgamated, thick-bedded, coarse-grained sandstone interpreted to represent vertically stacked channel axis deposits that also exhibit the least amount of lateral offset of channel units in the complex set. The authors suggest that the degree of lateral offset of channel element is controlled by either lateral confinement or abandonment relief (following the model by McHargue et al. (2011) discussed above). As the channel complex evolves and flows become finer grained, vertical stacking (i.e., minimal lateral offset) of channel fill is promoted by levee aggradation which progressively confines the channel or by the focussing of flows through an underfilled channel (high abandonment relief) (McHargue et al., 2011; Macauley & Hubbard, 2012). Additionally, Hodgson et al. (2011) describe a 40 m-thick unit dominated by amalgamated sand-prone deposits that transition laterally to thin-bedded, traction-structured sandstone and siltstone. This unit is interpreted to be levee-confined comprising vertically stacked channel axis deposits preserved during channel aggradation, deposited adjacent to proximal levees that fine and thin away from the channel.

4.2.3 Laterally Accreting Channel Elements

Table 4.2. Laterally Accreting Channel Elements at Castle Creek were described in detail by the following authors whose descriptions are used herein.

LATERALLY ACCRETING CHANNEL ELEMENT(S)	AUTHOR(S) AND YEAR PUBLISHED/COMPLETED
ICC1 UC3	- Navarro (2006) - Fraino (2020)
IC2.2, 2.3	- Arnott (2007) - Dumouchel (2015)
IC3U-C2	- Navarro (2006) - Navarro, Khan, & Arnott (2006) - Huyer (2016)
IC4.4	- Mussa-Caleca (2008) - Davis (2011) - Miklovich (2018) - Dumouchel (2015)
IC5.3-4	- Schwarz & Arnott (2007a,b)

4.2.3.1 Laterally Accreting Channel Elements – Descriptions

4.2.3.1.1 Isaac Channel Complex 1 – UC3

UC3 is the uppermost channel unit in ICC1 and is 30 m thick, comprising at least six channel fills (Figure 4.15). The base of UC3 exhibits a distinct stepped morphology and the channel fills are stacked in a laterally offset pattern. Individual channel fills are erosively based and 8-10 m in thickness. Fills are composed of thick- to very thick-bedded, coarse- to very coarse-grained sandstone, granule and minor pebble conglomerate, and uncommon mudstone-clast conglomerate. Upwards and laterally channel fills exhibit negligible change however obliquely upwards they pinch out and interfinger with thin-bedded, fine-grained, upper division turbidites.

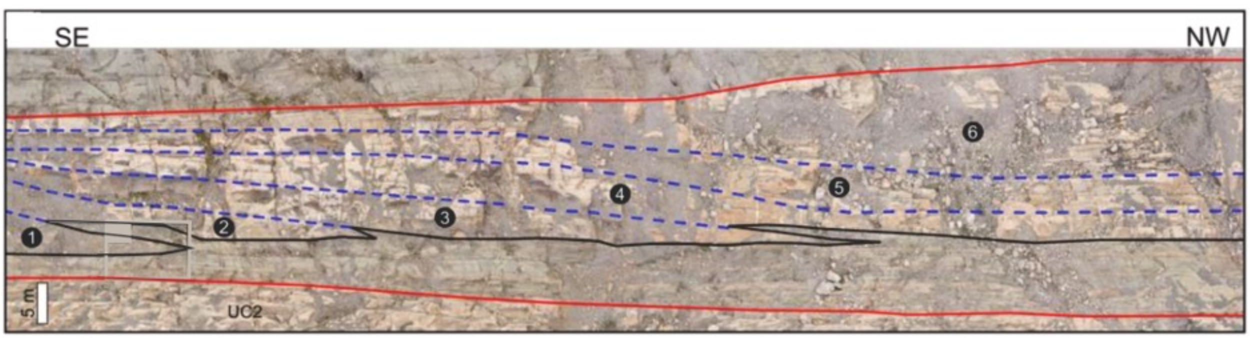

Figure 4.15. Aerial photograph of six laterally accreting channel elements in ICC1 UC3 (CCS). Channel bases are indicated by the dashed blue lines; note the dip of the channel fills relative to the bedding plane (solid red line) and the distinct stepped morphology of the base (solid black line). Photo from Fraino (2020).

4.2.3.1.2 Isaac Channel Complex 2

Isaac Channel Complex 2 (ICC2) consists of four channel units (IC2.1-2.4), although only IC2.2 and IC2.3 (Figure 4.16A) have been described in some detail by Arnott (2007) and Dumouchel (2015), respectively. In CCS, IC2.2 is exposed over a strike length of ~ 400 m, varies from 9.5 - 12.5 m in thickness, and sharply overlies a planar (though locally scoured) basal contact above IC2.1. Distinctively, strata dip at about 7-12° with respect to the channel base over distances of 120-140 m. The lower part of the unit is composed mostly of thick-bedded (1-2 m), normally graded, upper very coarse- to upper medium-grained sandstone with dispersed granules and local pebble conglomerate. Beds are sharp-based and commonly scoured, amalgamated, and show little upward change in grain size but thin to 0.4 - 0.8 m thick. Obliquely upward, coarse beds abruptly pinch out where they become poorly sorted and interfinger with adjacent fine-grained, thin-bedded turbidites (Figure 4.16B).

In the upper part of IC2.2 fine-grained strata interfingers with the underlying, coarse-grained strata. Obliquely downward fine-grained strata are truncated by the coarse amalgamated beds of the lower part (Figure 4.16C). Near this contact, fine-grained strata consist of medium- to thick-bedded nearly complete upper division turbidites (Tbcd). Obliquely upwards and over several metres, turbidites fine and thin towards the termini of the coarse-grained strata described above (Figure 4.16D). Here, they are composed mostly of thin- to medium-bedded, upper division turbidites (Tcd and Tbcd). 50 - 100 m beyond the termini of the coarse-grained strata, fine-grained strata are mostly Tcd and Td turbidites, and further laterally (> 100 m from coarse-grained pinch out), consist only of Td turbidites.

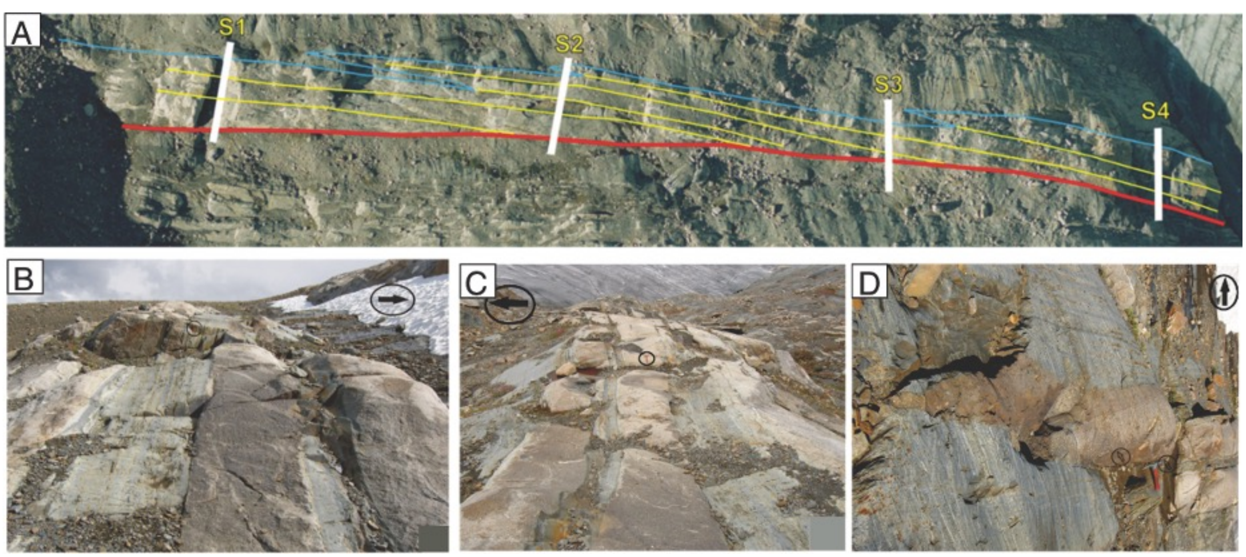

Figure 4.16. A) Interpreted aerial photo of IC2.2. Base of IC2.2 indicated by solid red line, note angle of dip of individual channel fills (solid yellow lines) relative to the planar basal contact. Blue lines illustrate the interfingering relationship between coarse- and fine-grained obliquely-dipping strata. B) Coarse-grained bed pinching out obliquely upward. C) Coarse-grained beds amalgamate obliquely downwards and erode fine-grained intercalated beds. D) Terminus of a coarse-grained "finger." All photos from Arnott (2007).

IC2.3 is 370 m wide and approximately 33 m thick and comprises 5 channel fills (IC2.3-1 to 5) that thicken to the northwest as a result of erosion along its basal contact (Figure 4.17). Similar to IC2.2, beds dip approximately at 8 - 12° with respect to the base of the channel unit and thin obliquely upward. The basal contact is sharp and characterized by a terraced "step" geometry. Channel fills are 5 - 15 m thick and 98 - 330 m in length and composed primarily of amalgamated, medium to very thick-bedded, coarse to very coarse sandstone and conglomerate. Interbeds of medium- to very thick-bedded, very coarse-grained sandstone and conglomerate with mudstone intraclasts are common only in IC2.3-2 but are observed locally throughout the channel unit. Thin- to very thin-bedded, fine-grained strata become more common towards the top of IC2.3-1 and IC2.3-3, and obliquely interfinger with coarse-grained strata in all channel fill elements.

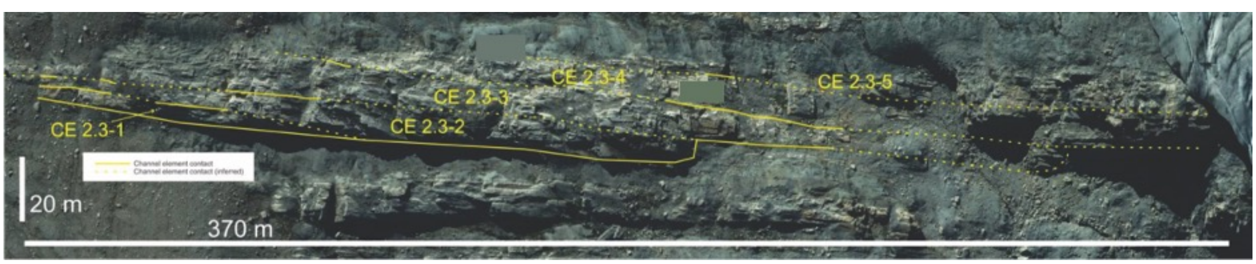

Figure 4.17. Aerial photo of IC2.3. Basal contact is characterized by a "step" morphology (solid yellow line). Channel fills dip at an angle of up to 12° to the bedding plane. From Dumouchel (2015).

4.2.3.1.3 Isaac Channel Complex 3 – IC3U-C2

IC3U-C2 is the uppermost channel unit in ICC3; it extends for 1.1 km along strike and thickens from 3 m to 15 m towards the northwest. It sharply overlies the lower channel unit and locally incises IC3L. Individual channel fills are 2 - 10 m thick and dip shallowly towards the northwest and are sharp-based, with localized steep erosion surfaces and rare mudstone intraclasts. Channel fills are dominantly coarse- to very coarse-grained, thick-bedded, lower division turbidites that towards the top of IC3U rapidly pinch out and interfinger with fine-grained thin-bedded turbidites.

4.2.3.1.4 Isaac Channel Complex 4 – IC4.4

IC4.4 crops out in three study areas, spanning a distance of ~ 3 km. In CCS it thickens from 1 m to 15 m towards the northwest and erosively overlies IC4.3. Across the glacier in Castle Creek North (CCN), IC4.1-4.3 are not observed and IC4.4 reaches a maximum thickness of 22 m. In CCHS IC4.4 thins from ~ 18 m to 10 m towards the northwest.

In CCS and CCN two channel fills are observed in IC4.4 and separated by a thick, laterally continuous mudstone-clast breccia unit. Fills are composed of amalgamated medium- to thick-bedded, very coarse- to medium-grained sandstone with common mudstone-clast breccia units overlying a sharp base. In both outcrops there is little upward change in grain size, however beds pinch out obliquely upward and interfinger with thin-bedded, fine-grained, upper division turbidites toward the southeast.

4.2.3.1.5 Isaac Channel Complex 5 – IC5.3-4

IC5.3-4 is the uppermost channel fill of Isaac Channel Complex 5; it is characterized by inclined (4-8°) strata exposed over a strike length of 250 m (Figure 4.18). The basal surface of IC5.3-4 is erosive and overlain by a mudstone-clast breccia and the fill is dominated by medium- to thick-bedded, coarse-grained, normally graded sandstone and pebbly conglomerate interbedded with thin-bedded, fine-grained upper division turbidites (Figure 4.18B). Inclined strata partially amalgamate down-dip but up-dip rapidly pinch out where they interfinger with finer-grained strata. The top of IC5.3-4 is draped by a laterally continuous (2.5 km) thin-bedded, fine-grained unit.

Figure 4.18. A) Aerial photo of IC5.3-4. B) Inclined beds of IC5.3-4 overlain by a unit of thin-bedded, fine-grained strata (right). Geologist for scale. Photos from Schwarz and Arnott (2007a,b).

4.2.3.2 Laterally Accreting Channel Elements – Interpretation

Inclined strata are interpreted to be lateral-accretion deposits (LADs) that accumulated on the inner bend margin of sinuous, laterally migrating deep-marine channels. The moderately well sorted and ubiquitous upper coarse, very coarse sandstone composition, which also changes change little upward or laterally, contrasts the upward-fining character of aggradational channel elements. Laterally accreting channels are common in the modern and ancient continental fluvial sedimentary record. In these systems lateral accretion is related to the development of a hydrostatic pressure gradient related to superelevation along the outer bank. Superelevation causes flow in the lower part to be directed inward near the bed and outward near the water surface generating the well-known secondary circulation cell in river bends. In this way, the cut bank is eroded while deposition occurs on the point bar. In submarine systems the flow is a *sediment*- rather than fluid-gravity flow, and gravity acts on suspended sediment in the flow rather than the fluid. As the flow rounds a channel bend coarse sediment becomes concentrated along the outer bank (cut bank) and generates a density gradient directed toward the inner bank (Figure 4.19), which mimics the effect of the hydrostatic pressure gradient in rivers (Arnott et al., in press). For the strength of the density gradient to be sufficiently well developed and overcome the outward-directed centrifugal acceleration, the basal part of the flow must remain confined to the channel (i.e., experience negligible overspill), which because of particle weight is enhanced in coarse-grained flows. Additionally, the flow consists of an essentially bimodal grain size distribution where the coarse-grained fraction forms a basal unstratified plug overlain sharply by finer-grained, lower density suspension. The elevated position of the density interface between the coarse, dense, lower part of the suspension and finer, less dense part causes the velocity maximum to be located far above the bed (Umax, Figure 4.19, in addition to inhibiting mixing of the two parts, thereby conserving flow momentum. Collectively, these morphologic, hydraulic and density conditions resemble those in the bends of fluvial channels with a secondary circulation pattern with near-bed flow directed toward inner bank and deposition on the point bar.

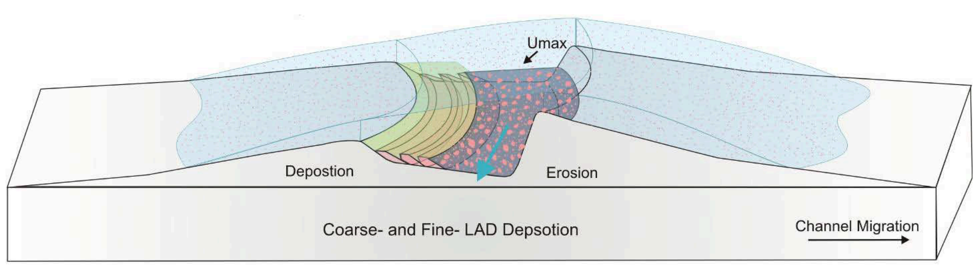

Figure 4.19. Cartoon illustrating LAD deposition. Coarse-grained fraction of the flow is concentrated along the outer bend forming a density gradient directed towards the inner bend, where deposition occurs. Sediment accumulates on the inner bend as the channel migrates laterally (Davis, 2011).

At Castle Creek, lateral-accretion elements are observed at the top of channel complexes and overlie aggradational channel elements in all cases except ICC2, where the entire complex is interpreted to consist of laterally accreting channel fills. The consistent superposition of laterally accreting fills above aggradationally filled channel complexes is consistent with the waxing-waning cycles of McHargue et al. (2011) whereby channel fill stacking pattern gradually changes from primarily disorganized (aggradational) to organized (laterally accreting) (Figure 4.20). McHargue et al. argue that this upward change is a result of waning flow that transports increasingly finer-grained sediments and promotes the building of levees that causes increasing flow confinement. Alternatively, Fraino (2020) and Fraino et al. (accepted) suggest that the upward change reflects systematic and recurring changes in the coarse-grained fraction of the sediment supply. Specifically, during episodes of rising relative sea level increased shelf accommodation preferentially sequesters coarse-grained sediment that then becomes available for transport to the shelf-edge during short-term episodes of lowered relative sea level. This enrichment of coarse sediment results in a bimodal sediment supply that promotes riverine-like patterns of lateral channel migration (cutbank erosion) and point-bar deposition.

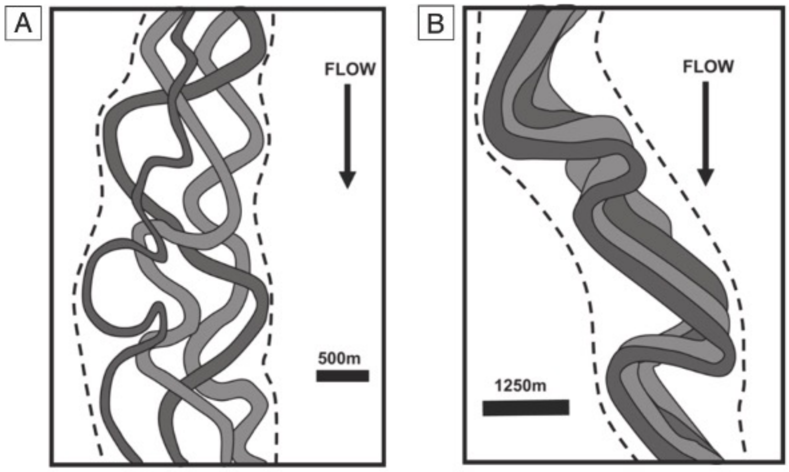

Figure 4.20. A) Disorganized stacking pattern associated with aggradational channel elements. B) Organized stacking pattern associated with laterally accreting channel elements (McHargue et al., 2011).

4.3 Overbank Element

4.3.1 Levees - Overview

Submarine levees make up a significant portion of deep-marine turbidite systems where they can be up to a few hundred metres thick and tens of kilometres wide (Birman et al., 2009). Levees are depositional features built of sediment that spills out of the adjacent channel. Overspill occurs by three main processes: flow stripping, inertial overspill, and continuous overspill. Flow stripping and inertial overspill occur preferentially along the outer banks of sinuous channels (Arnott, 2010). Flow stripping is related to the detachment of the dilute, fine-grained upper part of the flow from the more dense, coarse-grained lower part of the flow that remains confined to the channel (Figure 4.21A). Inertial overspill occurs where sufficient kinetic energy of the channelized flow can be converted to particle suspension (i.e., potential energy) that allows particles to be uplifted and overspilled over the levee surface at a bend (Figure 4.21B). Continuous overspill is the most common and occurs everywhere the thickness of the current exceeds the height of the levees. However, irrespective of overspilling mechanism, upon leaving the confines of the channel the flow rapidly wanes, resulting in a rapid loss of (sediment transport) capacity and competence that becomes manifest as a progressive fining and thinning of strata away from the channel (Figure 4.21C). This lateral thinning of beds away from the channel axis gives levee deposits the characteristic "gull-wing" morphology in seismic cross-sections (Clark & Pickering, 1996).

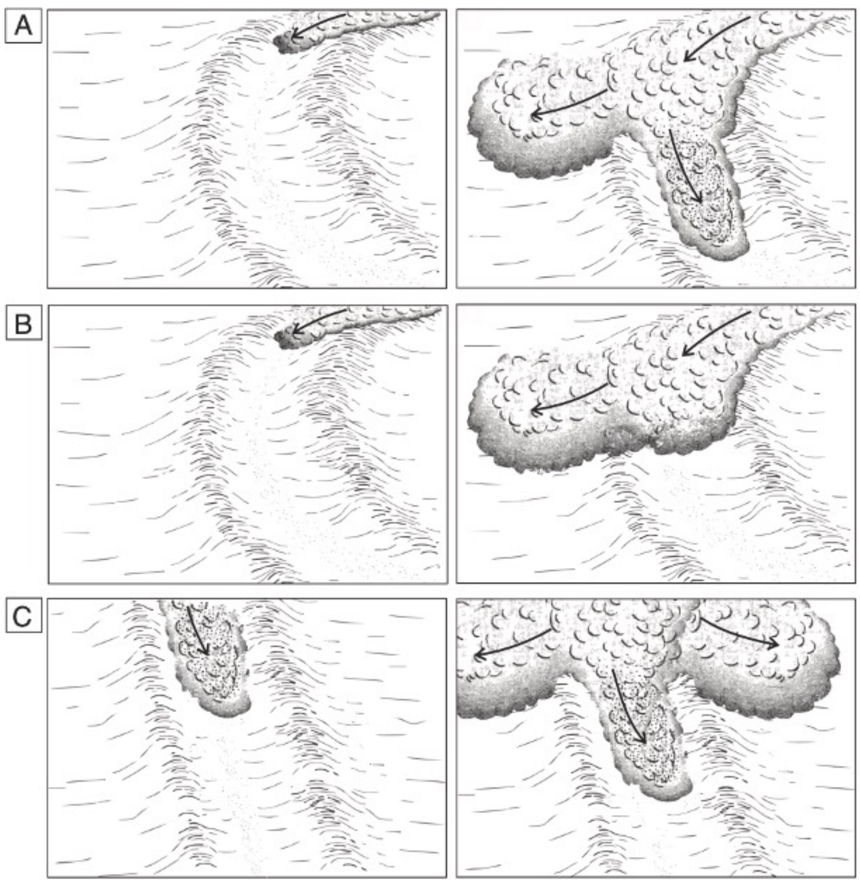

Figure 4.21. Cartoons illustrating overspill processes. A) Flow stripping; Dilute, fine-grained upper part of the flow preferentially overtops the outer bend levee crest. The lower, denser part of the flow remains confined in the channel B) Inertial overspill; Entire flow is able to run up the outer bend levee and escape the channel if energy of the flow is sufficient. C) Continuous overspill; the dilute, fine-grained upper part of the flow becomes unconfined as it breaches the levee crest and rapidly decelerates, depositing sediment that progressively fines and thins away from the adjacent channel (Khan, 2012 modified from Peakall et al., 2000 and Kane, 2007).

4.3.2 Proximal Levees

4.3.2.1 Description

Table 4.3. Proximal Levee Overbank Elements at Castle Creek have been described in detail by the following authors whose descriptions are used herein.

ASSOCIATED CHANNEL COMPLEX	AUTHOR(S) AND YEAR PUBLISHED
ICC1	- Fraino (2020)
ICC2	- Arnott (2007) - Dumouchel (2015)
ICC3	- Khan & Arnott (2010) - Khan (2012)
ICC4	- Ruso (this study)
ICC4.5	- Bergen (2017)
ICC5	- Schwarz & Arnott (2007a,b)

Proximal levees have been reported to be associated with ICC1, ICC2, ICC3, ICC4, ICC4.5, and ICC5, and are subdivided into two types: outer bend and inner bend proximal levees. Proximal outer bend levees are observed in ICC3 and ICC4.5, and typically comprise 5 - 28 m-thick packages that generally fine and thin upward (Figure 4.22). Packages commonly consist of two parts: coarse-grained lower part overlain sharply by a finer grained upper part. The lower part is 3 - 11 m thick and composed of medium- to thick-bedded, coarse- to fine-grained, lower division (Tb/Tc/Tbc, less common Ta) turbidites interbedded with very thin- to thin-bedded, fine-grained sandstone to siltstone upper division turbidites. The upper part ranges from 2 - 18 m thick and is dominated by very thin- to thin-bedded, fine-grained upper division turbidites with rare medium- to thick-bedded, lower division turbidite interbeds. Notably, coarse-grained beds in the lower part show a lateral thickening then thinning trend away from channel whereas the upper part initially thins then thickens in the same direction. Ripple cross-stratified beds (Tc) in proximal levee deposits are commonly multiset (3-4) and single set (1-2).

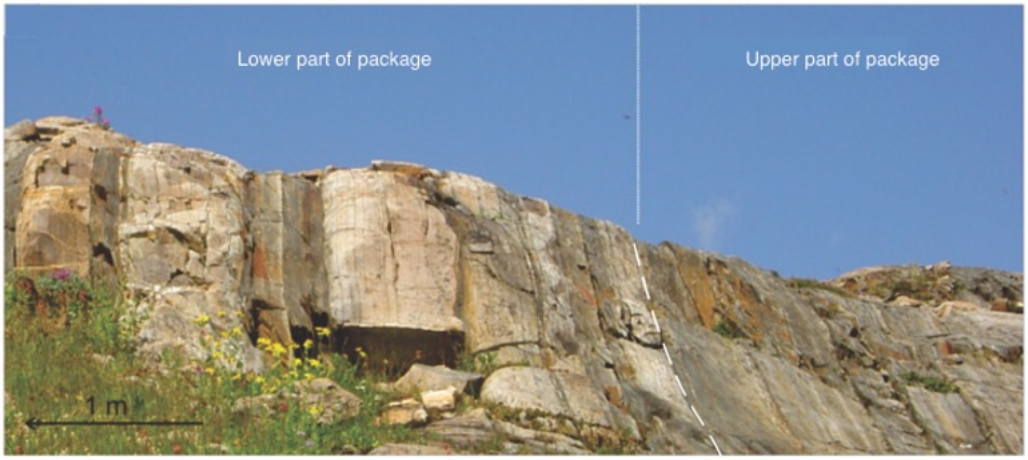

Figure 4.22. Outer bend levee package. The coarse-grained lower part is abruptly overlain by the fine-grained upper part of the package (modified from Khan & Arnott, 2011).

Inner-bend levee deposits are observed in all channel complexes discussed in this paper. In ICC1, ICC2, ICC4, ICC5, and the uppermost channel unit in ICC3, thin-bedded, fine-grained, mostly upper division turbidites exhibit a complex interfingering with coarse-grained LADs (see discussion above) – the fine-grained units being the inner-bend levees onto which the coarse-grained LADs onlapped (Figure 4.23). In the lower part of ICC3, inner-bend levee deposits can be divided into lower and upper units 17 m and 40 m thick, respectively. Both units are similarly composed of very thin- to thin-bedded, fine-grained sandstone to siltstone (Tcd division turbidites). The lower unit gradually thins upward but laterally there is negligible change in grain size or bed thickness. In contrast, the upper unit is characterized by a distinct interfingering relationship with thin-bedded fine-grained turbidites associated with the lateral transition from coarse-grained amalgamated channel axis that fine and interfinger with inner bend levee strata.

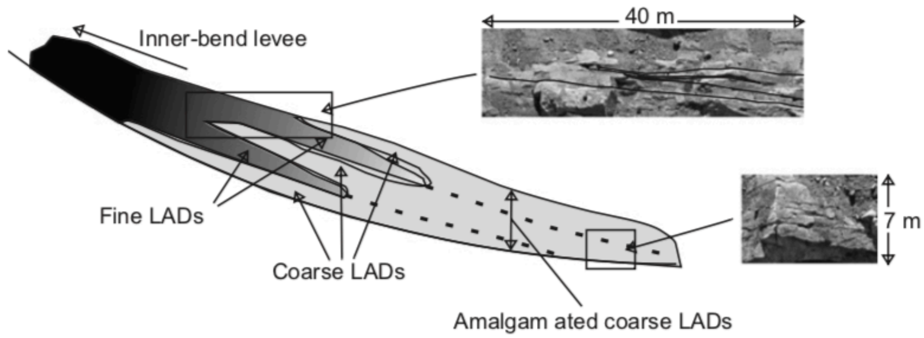

Figure 4.23. Oblique interfingering of coarse-grained LADs with fine-grained LADs that rapidly transition to inner bend levee deposits (see upper inset for outcrop photo). Coarse-grained LADs amalgamate obliquely downwards (see lower inset for outcrop photo) (Arnott, 2007).

4.3.2.2 Proximal Levees – Interpretation

Proximal levee deposits consisting of a sand-rich basal part overlain abruptly by finer, thin strata are interpreted to reflect evolution of the levee deposition and conditions in the channel-bound flows (Figure 4.24E). According to Bergen (2017) and Bergen et al. (accepted), the lower part of each levee package is interpreted to correspond to channel inception and the early stages of channel fill when low levee relief allowed the coarse-grained basal part of flows to easily overtop the levee crest (Figure 4.24A-B). Moreover, flows at this time had a two-part structure consisting of a dense basal part exhibiting a plug-like density structure, and therefore negligible vertical stratification, that then was overlain sharply by a low-density upper part with density decreasing exponentially upward. The interface separating the two parts coincided closely with the height of the flow's point of velocity maximum, which during the early stages of channel evolution was located above the levee crest (Figure 4.24B). As the levee aggraded the height of the levee crest eventually matched the height of the velocity maximum, after which generally only the low-density upper part of the channel-bound currents overspilled (dashed line, Figure 4.24C), resulting in an abrupt fining and thinning of levee deposits. Bergen (2017) also suggested that some time thereafter a dramatic change in the granulometric make-up of the sediment supply altered the density structure of the flow and resulted in a lowering of the velocity maximum toward the bed. On the levee fine-grained sediment continued to be deposited, but because of newly developed stratification and (sediment) concentration effects, sediment, and in particular coarse sediment, became increasingly sequestered and deposited in the channel (Figure 4.24D).

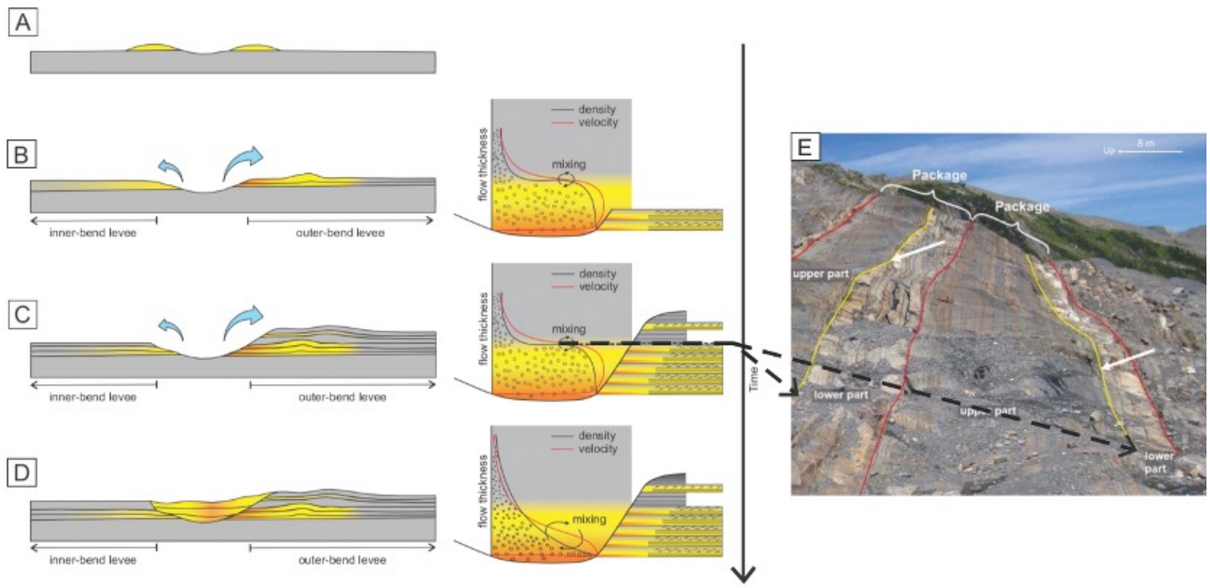

Figure 4.24. Evolution of channel-bound flows and proximal levee development with time. A) Incipient conditions; initial overspill deposits ridges immediately adjacent to channel. B) Channelized flow adopts a plug-like density structure (coarse-grained, well sorted); dense, coarse-grained lower part of the flow is able to overspill and deposit coarse-grained, thick-bedded, lower division turbidites (e.g., lower package, E). C) Height of the levee crest exceeds the height of the velocity maximum of the flow; only the dilute, fine-grained upper part of the flow overspills and deposits fine-grained, thin-bedded, upper division turbidites (e.g., upper package, E). This transition is marked by the sharp contact between the lower and upper package (dashed black line; C, E). D) Change in sediment supply causes the flow to become more poorly sorted and adopt a vertically stratified density structure; height of the velocity maximum moves closer to the bed resulting in upwards fining and thinning of beds deposited by overspilling flows. Coarse-grained deposition occurs within the channel as the flow loses energy due to mixing (modified from Bergen, 2017; Bergen et al., accepted).

The initial thickening and then thinning trend of thick, coarse-grained deposits in the lower part of proximal levee packages is a consequence of flow inertia and the outward displacement of the point of maximum sedimentation from the channel margin. Specifically, owing to their greater inertia, high-concentration, high-energy flows begin to first wane, and accordingly, the rate of sedimentation to increase, further from the channel margin compared to finer-grained, low-energy flows (Khan & Arnott, 2011). Beyond this point, the rate of deposition decreases rapidly, and flows deposit progressively finer and thinner beds that are little different from those deposited by the finer, lower-energy flows.

In the lower part of ICC3, inner bend levees are interpreted to be deposited by flows that are lower in energy and magnitude compared to those that deposited the outer-bend proximal levees discussed above. The lateral interfingering of the upper inner bend levee unit suggests low levee relief which allowed channelized flows to expand laterally and progressively fine and thin.

4.3.3 Distal Levees

4.3.3.1 Description

Table 4.4. Distal Levee Overbank Elements at Castle Creek have been described in detail by the following authors whose descriptions are used herein.

ASSOCIATED CHANNEL COMPLEX	AUTHOR(S) AND YEAR PUBLISHED
ICC1	- Fraino (2020)
ICC3	- Khan & Arnott (2011) - Khan (2012)
ICC4.5	- Bergen (2017) - Ruso (this study)

Distal levee deposits are observed on the distal margins of ICC1, ICC3, and ICC4.5 (observed in CCS to CCHS and CCN to CCHS, respectively) where they are up to 80 m thick and dominated by very thin- to thin-bedded, fine-grained upper division turbidites interbedded with rare thick-bedded, coarse-grained lower division turbidites (Figure 4.25). Notably, fine-grained distal levee strata exhibit little lateral and vertical change in both grain size and bed thickness. Coarse-grained interbeds, on the other hand, typically thin away from the channel, but uncommonly, thin and pinch out towards the channel. In addition, small-scale (up to 3 m thick) mass transport deposits are commonly observed in distal levee strata.

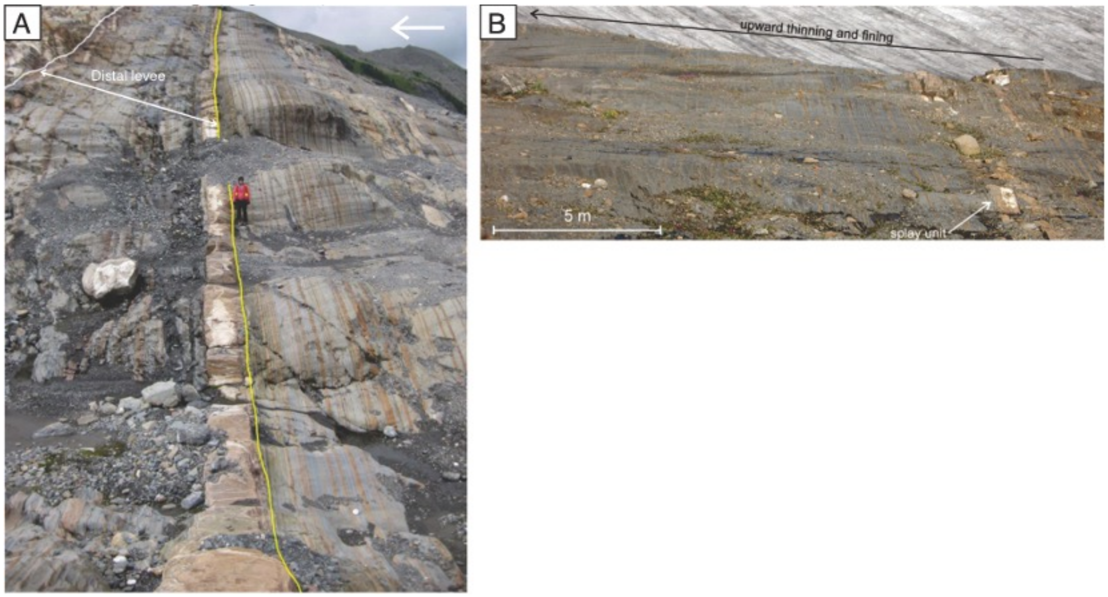

Figure 4.25. A) Distal levee deposit in ICC4.5. Thick-bedded, medium-grained T_{bcde} turbidite is located at the base of the levee and is overlain by very thin- to thin-bedded fine-grained T_{cde} turbidites that make up the bulk of the deposit (yellow line indiactes basal contact). Stratigraphic up is indicated by white arrow, field assistant for scale (Bergen, 2017). B) Characteristic upward fining and thinning of a distal levee associated with ICC3 (Khan & Arnott, 2011).

4.3.3.2 Distal Levees – Interpretation

Thin-bedded, fine-grained distal levee deposits are interpreted to represent deposition by low- and moderate-energy flows that progressively waned with increasing distance from the channel. Thick-bedded, coarse-grained interbeds, on the other hand, are interpreted to be the product of anomalously high-energy overbank flows that allowed coarse sediment to bypass the proximal levee. Enhanced mobility of coarse-grained sediment and deposition on the distal levee may also reflect the development of steep slopes on the backside of the levee; a condition that is also suggested by the common occurrence of thin (cm to a few m) mass transport deposits in distal levee strata (Figure 4.26) (Khan & Arnott, 2011)

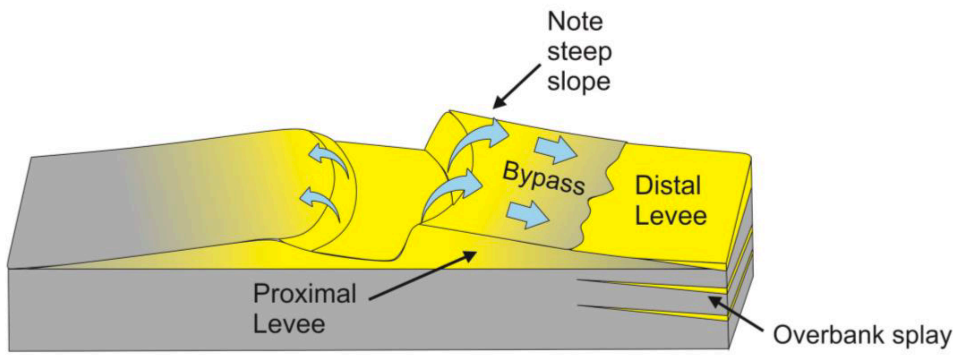

Figure 4.26. Depositional model of thick-bedded, coarse-grained interbeds. High-energy overspilling flows deposit coarse-grained sediment distal to adjacent channel as flow is able to bypass the proximal levee before rapidly decelerating (Bergen 2017 modified from Davis 2011).

4.3.4 Abandonment

4.3.4.1 Description

Table 4.5. Abandonment Overbank Elements at Castle Creek have been described in detail by the following authors whose descriptions are used herein.

ASSOCIATED CHANNEL COMPLEX	AUTHOR(S) AND YEAR PUBLISHED/COMPLETED
ICC1	- Fraino (2020)
ICC4	- Mussa-Caleca (2005)
ICC5	- Schwarz & Arnott (2007a,b)

Abandonment elements are associated with ICC1, ICC4, and ICC5. In ICC1, abandonment strata are associated with individual channel fills (10 – 30 cm thick units) and channel units (8 – 12 m thick units). Channel fill abandonment strata are laterally discontinuous and are composed of very thin- to thin-bedded, fine-grained, upper division turbidites that fine and thin upwards (Figure 4.27). Channel unit abandonment strata comprise successions of thin- to medium-bedded, fine- to medium-grained T_{bcde} turbidites than fine and thin upward into fine-grained upper division (T_{cde}) turbidites. ICC4 abandonment strata overlie the channel complex in CCS and comprise an ~ 30 m-thick unit of 0.1 - 2 m-thick packages of thin-bedded, medium- to very fine-grained sandstone (Tbcde) turbidites interbedded with silty mudstone that become more common and increase in thickness upwards. In ICC5, abandonment elements are ~ 11 m thick and overlie each channel complex. They are lithologically similar to those in ICC4, being composed of Tbcde turbidites that stratigraphically upwards are increasingly intercalated with finer and thinner Tcde turbidites. Tc divisions are typically single set and starved ripples. In both cases, sandstone-to-mudstone ratio decreases significantly upwards.

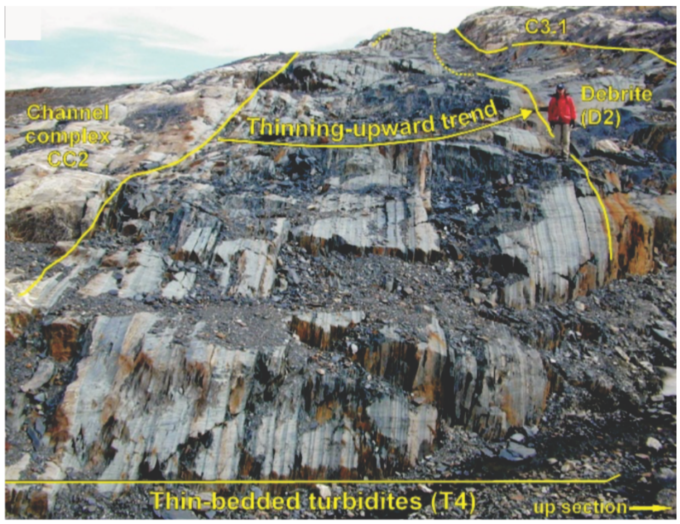

Figure 4.27. Medium- to thin-bedded turbidites comprise thinning-upward successions that overlie each channel complex in ICC5. Fine-grained sandstone beds thin upwards as silty mudstone beds become more common (from Schwarz and Arnott, 2007). Geologist for scale.

4.3.4.2 Abandonment – Interpretation

The progressive upward-fining and -thinning of turbidite beds, in addition to the thickening and increased abundance of silty mudstone interbeds, is interpreted to represent the partial or complete infilling of deactivated channels by progressively more dilute, lower energy turbidity currents. Deactivation of the channel complex is likely the result of a relative sea level rise or an up-flow avulsion (Posamentier & Kolla, 2003).

4.4 Mass Transport Element

4.4.1 Overview

Mass transport deposits (MTDs) are significant elements of modern and ancient deep-marine systems, forming kilometre-scale features that can make up over half of the thickness of the stratigraphic section (Posamentier & Martinsen, 2010). Due to their areal extent and thickness these elements form excellent stratigraphic markers. Mass transport events are gravity-driven processes associated with failure of an upslope sediment pile, and their deposits can be subdivided into three kinds: slides, slumps, and debrites based on the nature of movement (Table 4.6; see Deep-Marine Sedimentation Processes discussion above). Slides are primarily translational and characterized by an array of listric faults that fragment the sediment pile into a mélange of coherent blocks, whereas slumps experience a rotational component during movement as evidenced by more ductile deformation (e.g., folding). Debrites are the deposits of debris flows, which are sediment-gravity flows wherein sediment is maintained in suspension principally by matrix strength, and characteristically are poorly sorted and mud-prone.

Table 4.6. Classification of gravity-driven mass transport deposits. Slides are minimally deformed blocks of coherent sediment that are translated along a failure plane whereas slumps exhibit ductile internal deformation as a result of rotational movement along a curved failure plane. Debris flows deform plastically as a result of clay-clay bonding (i.e., matrix strength) and deposit en masse as the flow freezes from the top down (Mulder and Alexander, 2001; table from Moscardelli and Wood, 2008).

GRAVITY INDUCED DEPOSITS			Genetic Classification Transport Mechanism	Descriptive Classification Sedimentary Structures	Seismically Recognizable Features (Moscardelli et al., 2006; this work)
Mass Transport Complex	Slide	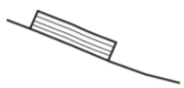	Shear failure along discrete shear planes with little or no internal deformation or rotation	Essentially undeformed, continuous bedding	Continuous blocks without apparent internal deformation. High-amplitude, continuous reflections.
	Slump		Shear failure accompanied by rotation along discrete shear surfaces with various degrees of internal deformation	Plastic deformation particularly at the toe or base. Plow structures, folds, tension faults, joints, slickensides, grooves, rotational blocks	Compressional ridges, imbricate slides, irregular upper bedding contacts, duplex structures, contorted layers. Low- and high-amplitude reflections geometrically arranged as though deformed through compressive stresses.
	Debris Flow		Shear distributed throughout the sediment mass. Strength is principally from cohesion due to clay content. Additional matrix support may come from buoyancy. Plastic rheology and laminar state.	Matrix supported, random fabric, clast size variable, matrix variable. Rip ups, rafts, inverse grading and flow structures possible.	Mega rafted and/or detached blocks, irregular upper bedding contacts, lateral pinch-out geometries, oriented ridges and scours. Low-amplitude, semitransparent chaotic reflections.

Gravitational instability and related MTD emplacement commonly correlate with changes of relative sea level, and therefore position in a depositional sequence (Figure 4.28). During the falling stage and early part of the lowstand systems tracts, reduced weight of the overlying water column causes pore pressures within the sediment pile to become locally elevated above hydrostatic, which then leads to gravitational instability and ultimately failure of the outer shelf and/or upper slope. Additionally, at the onset of the transgressive systems tract, transgressive conditions load the outer shelf with sediment and a thickening water column causes another period of instability and MTD emplacement.

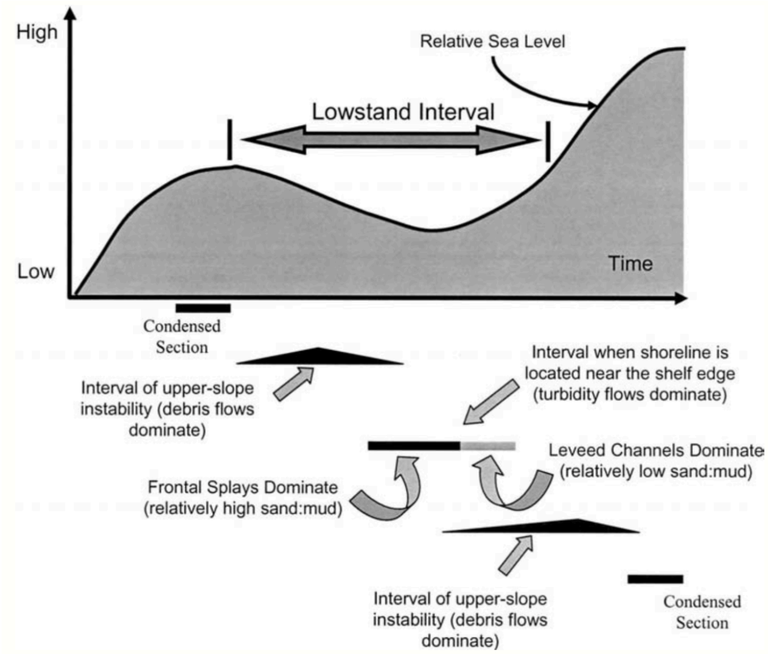

Figure 4.28. Schematic illustrating the succession of architectural elements associated with changes in RSL (Posamentier and Kolla, 2003). The base of the succession consists of a condensed section overlain by MTDs at the onset fo RSL fall. Frontal splays are the dominant architetural element during late RSL fall and lowstand, while leveed channels dominate at late lowstand and early RSL rise. Another period of instability during late RSL rise is associated with MTD deposition, and RSL highstand is characterized by another condesned section.

4.4.2 Descriptions

Table 4.7. Mass Transport Elements at Castle Creek were described in detail by the following authors whose descriptions are used herein.

MASS TRANSPORT ELEMENT	AUTHOR(S) AND YEAR PUBLISHED
MTD 2	- Laurin (2005) - Laurin et al. (2005)
MTD 3	- Ruso (this study)
MTD 4	- Marion (2005) - Bergen (2017) - Ruso (this study)

4.4.2.1 MTD 2

MTD 2 is situated between ICC2 and ICC3 and overlies a sharp and locally erosive base. It consists of a 60 - 130 m-thick mixed succession of slide/slump and debrite units that can be traced from CCS to CCN (2.2 km). In CCN, MTD 2 comprises a 55 m-thick slide/slump made-up of deformed, fault-bounded blocks consisting mostly of interbedded sandstone and mudstone, overlain by a 16 m-thick debrite with dispersed quartz pebbles, carbonate-cemented mudstone clasts, and common stromatolite and oolite fragments. In CCS, an ~ 15 m-thick quartz pebble conglomerate unit (red unit, Figure 4.29A) makes up the base of the succession and is overlain by a 20 m-thick slide. A 30 m-thick, mud-rich debrite with dispersed shallow-water carbonate clasts marks the top of the succession, and the base of the debrite contains an 18 m-thick clast of thin- to medium-bedded turbidites (UDFD and TBT units, Figure 4.29A). Along strike to the southeast the MTD reaches its maximum thickness (130 m) and incises strata in the upper part of ICC2 (Figure 4.29B). Here, MTD 2 is dominated by units of mud-rich (unit 3, Figure 4.29) and sand-rich (units 1, 2, 5, 6; Figure 4.29) debrites with common quartz pebble and carbonate clasts. Notably, shallow-water carbonate clasts become increasingly more common stratigraphically upward whereas carbonate cemented-sandstone and mudstone clasts are more common at the base of the MTD. An isolated channel filled with amalgamated, pebble to granule conglomerate and medium-grained, normally graded sandstone forms a < 15 m-thick interbed (unit 4) that infills topography on an underlying debrite (unit 3), and in turn is overlain by a younger debrite (unit 5).

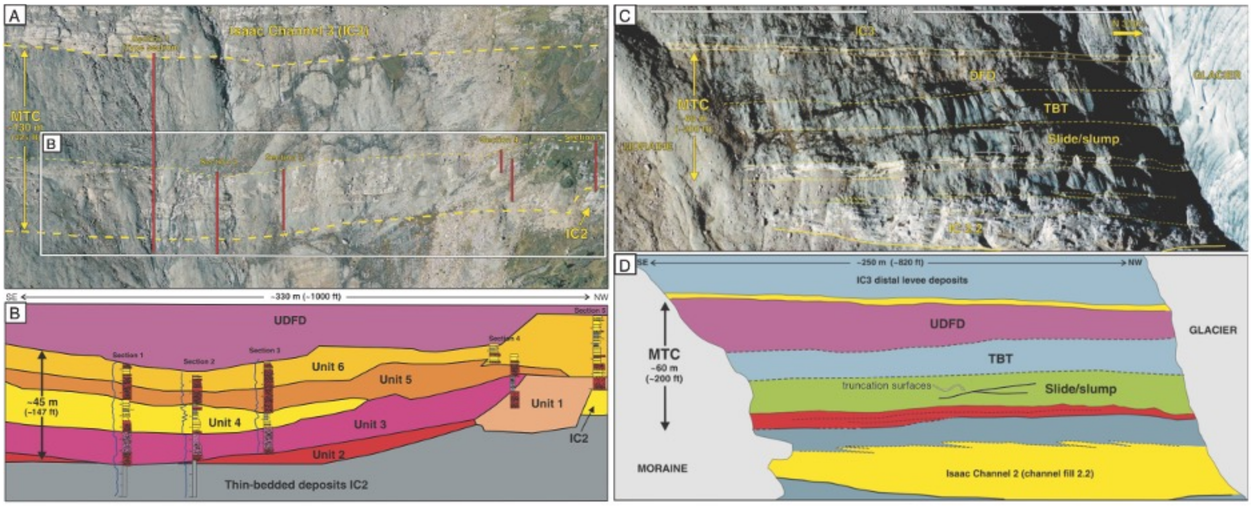

Figure 4.29. A) Aerial photo of MTD 2 in SED, inset shows location of B. B) Interpretation of aerial photo of MTD 2 in SED. Note truncation of ICC2 (right). C) Aerial photo of MTD 2 in CCS. D) Interpretation of aerial photo of MTD 2 in CCS. TBT unit in centre (blue) is a clast within the slide/slump (green). UDFD can be correlation across the moraine to SED (from Laurin et al., 2007).

4.4.2.2 MTD 3

MTD 3 extends across CCHS (~ 1 km), is up to 170 m thick, and is sharply overlain by ICC4. It is composed of rafted channel blocks and units of deformed upper division turbidites. Blocks of sand-rich channel fills that in some cases are up to ~23 m thick and 40 m wide dominate MTD 3 with subordinate blocks of thin-bedded, fine-grained turbidites (Figure 4.30A). Channel fills within these blocks are composed of very thick- to thick-bedded, normally graded, pebble- to granule-conglomerate and upper very coarse- to upper medium-grained, structureless sandstone (Ta) and uncommon beds of upper coarse- to lower medium-grained, planar-laminated sandstone are observed (Tab). Mudstone clasts are common at the base of beds. In addition, medium- to thick-bedded, upper medium- to upper fine-grained, normally graded, matrix-rich to matrix-intermediate sandstone comprise a unit (~ 31.5 m from top of MTD) that thickens from 1.3 m to 6.7 m towards the northwest. The beds within this unit contain mudstone chips, fine and thin upwards, and are typically capped by 1 - 2 cm mudstone bed. Thin-bedded, fine-grained sandstone to siltstone beds (Tbcd/Tcd) form units that are 0.3 – 11 m thick and exhibit minor ductile deformation.

An ~ 6 m thick, erosively-based slump consisting of inclined and folded beds of lower fine-grained sandstone to mudstone beds (Figure 4.30B) is observed ~ 2.5 m above the base of MTD 3 and pinches out towards the northwest. Additionally, an 11 m-thick debrite occurs 11 m above the base of MTD 3.

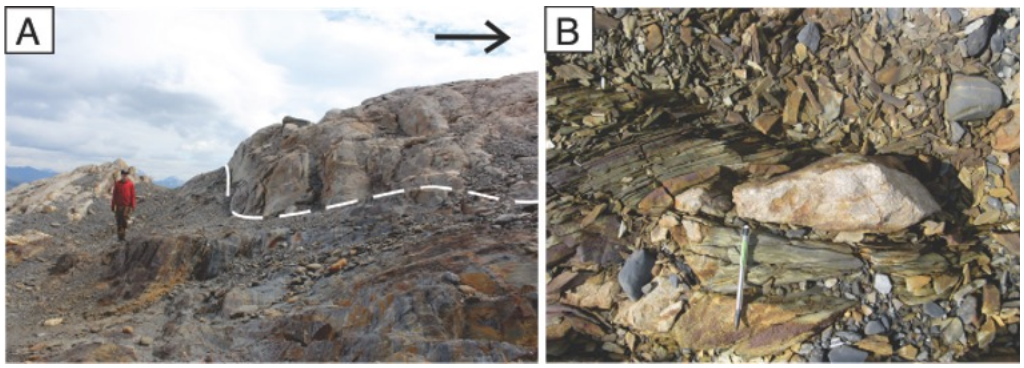

Figure 4.30. A) Rafted channel block in CCHS. Dashed line indicates contact between channel block and surrounding thin-bedded, fine-grained strata. Arrow indicates stratigraphic up, field assistant for scale. B) Ductile deformation of thin-bedded, fine-grained strata associated with slumping. Pencil is approximately 15 cm long.

4.4.2.3 MTD 4

MTD 4 is a complex succession of debrites and slides associated with ICC4.5 and is subdivided into two slides (S1-S2) and four debrites (D1-D4) (Figure 4.31A). In CCN, S1 is a 23 m-thick succession of minimally deformed upper division turbidite beds that overlies a steep irregular surface (dashed line, Figure 4.31B) that then flattens until it, and the entirety of S1, become covered by moraine.

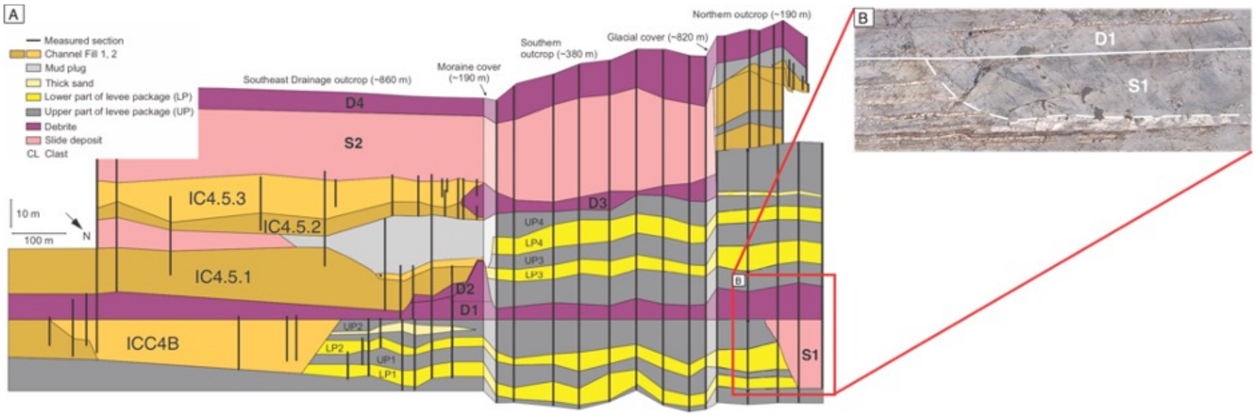

Figure 4.31. A) Debrites (D1-D4) and slides (S1-S2) associated with ICC4.5 from SED to CCN. B) Inset shows S1 truncating ~ 23 m of underlying stratigraphy (dashed line) and contact between S1 and D1 (solid line). Modified from Bergen et al. (accepted).

S2 crops out over a strike length of ~ 1.4 km in SED and CCS, but does not extend into CCN. In CCS, S2 overlies D3 and is ~ 35 m thick and in SED is 30 m thick and overlies IC4.5.5. S2 is composed of stacked units made up of two parts. The lower part is a few dm-thick and consists of a poorly sorted mixture of quartz pebbles, coarse-grained sandstone, and mudstone clasts dispersed in a silty mudstone matrix. The upper part gradationally overlies the lower part, is a few m-thick, and composed of deformed upper division turbidites that stratigraphically upwards become less deformed. Thin-bedded upper division turbidites (Tcde) beds in the upper part contain dispersed carbonate-cemented sandstone clasts.

Directly overlying S1, D1 spans the entire study area from SED to CCHS (~4 km). The basal contact is sharp and planar, and thickness ranges from 0.5 - 12.6 m (Figure 4.32A). D1 is composed of quartz pebbles, up to boulder-sized carbonate-cemented sandstone and mudstone clasts dispersed in a silty mudstone matrix (Figure 4.32B). Carbonate-cemented sandstone clasts commonly overlie the basal contact and are rare in CCS but become more common towards the northwest. Local oolite and stromatolite fragments are observed in all outcrops except CCHS.

In SED, D2 crops out between D1 and IC4.5.3 and thins over a distance of ~ 35 m from 0.5 - 6 m thick. In CCS, D2 is 42 cm thick and also overlies D1 but only crops out over a lateral distance of ~ 15 m. Across the glacier in CCN, D2 crops out in the form of isolated rafts at the top of D1 that are up to 3 m long and 1.2 m thick. Strata of D2 comprise a poorly sorted succession of abundant carbonate and mudstone clasts dispersed in an upper coarse-grained sandstone matrix (Figure 4.32C-D). Oolite and stromatolite fragments are observed in carbonate clasts.

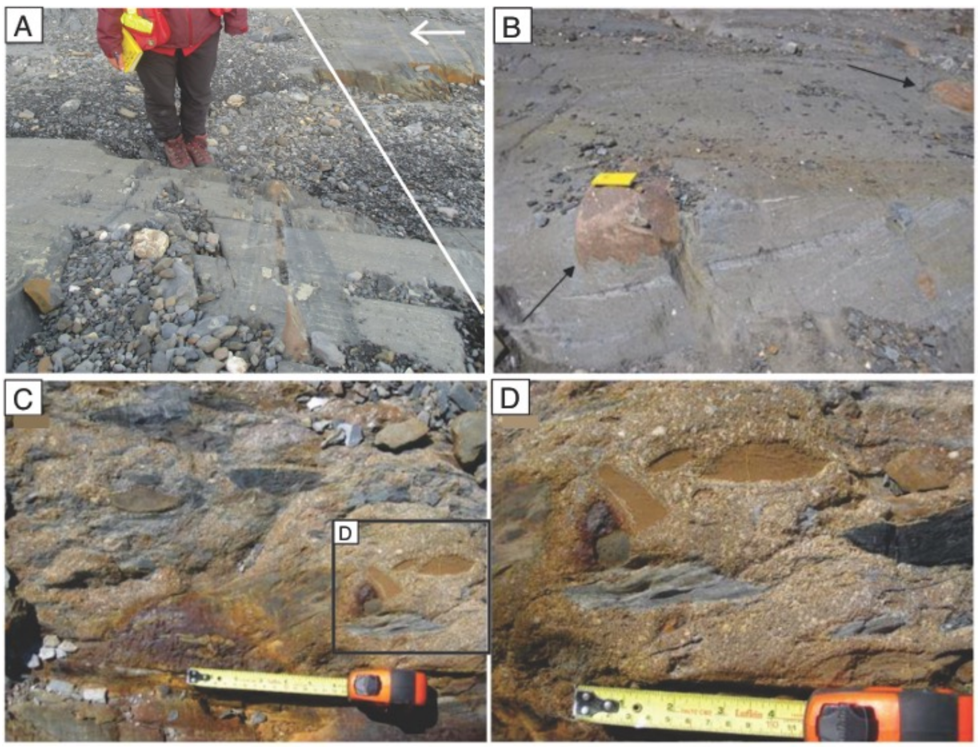

Figure 4.32. A) Base of D1 in contact with underlying stratigraphy in CCHS (solid line), arrow indicates stratigraphic up. B) Up to boulder-sized clasts of carbonate-cemented sandstone in D1. C) Carbonate-cemented sandstone and mudstone clasts in D2. D) Inset showing close up view of clasts in D2; carbonate-cemented sandstone and mudstone, dispersed granules and very coarse-grained sandstone in coarse-grained sandstone matrix. Photos B-D from Bergen (2017).

D3 is exposed in SED where it thickens to 11 m towards the northwest. In CCS thickness varies between ~ 1.4 - 9 m and has a sharp basal contact. D3 is poorly sorted and consists of very coarse-grained sand grains and clasts of mudstone, carbonate-cemented sandstone and mudstone dispersed in a matrix of a silty mudstone. At the southeast end of the outcrop, a 1.8 m-thick by 10 m-wide coarse-grained sandstone raft crops out at the base of D3. Similarly, at the northwestern end of the outcrop a 2.9 m-thick and 26 m-wide, coarse-grained sandstone raft also crops out at the base of D3 (Figure 4.33A). Carbonate-cemented sandstone clasts commonly consist of folded thin-bedded, fine-grained upper division turbidites (Figure 4.3B).

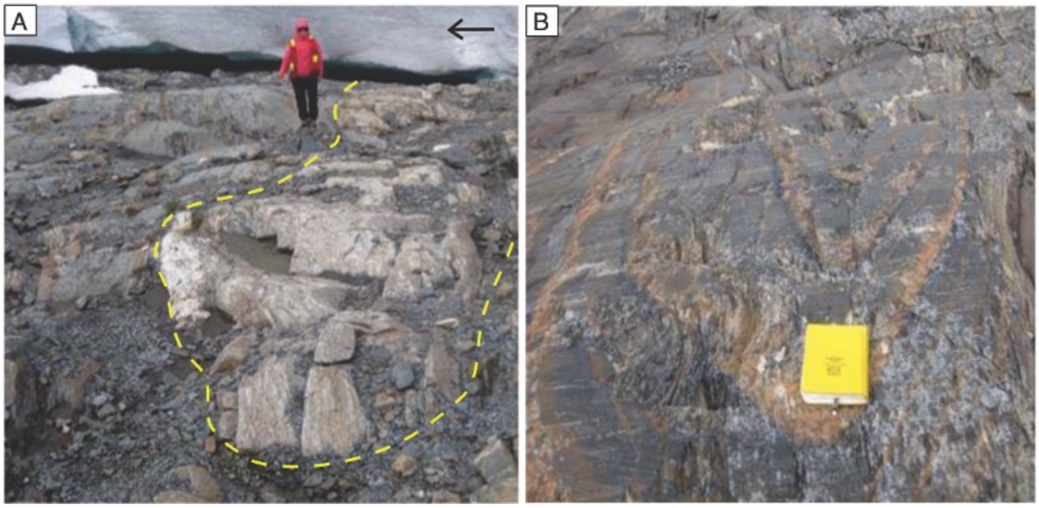

Figure 4.33. A) Coarse-grained sandstone raft at the base of D3 in CCS. B) Folded clast composed of fine-grained, thin-bedded turbidites. From Bergen (2017).

D4 sharply overlies S2 in SED and CCS and crops out again in CCN before pinching out under the moraine between CCN and CCHS. Towards the southeast D4 thins from 18 m to ~ 7.6 m. D4 is poorly sorted and is composed of quartz pebbles, upper very coarse-grained sand grains, clasts of lower medium-grained carbonate cemented sandstone, and less common mudstone and carbonate clasts all dispersed in a matrix of silty mudstone (Figure 4.34). Carbonate-cemented sandstone clasts are commonly folded and deformed.

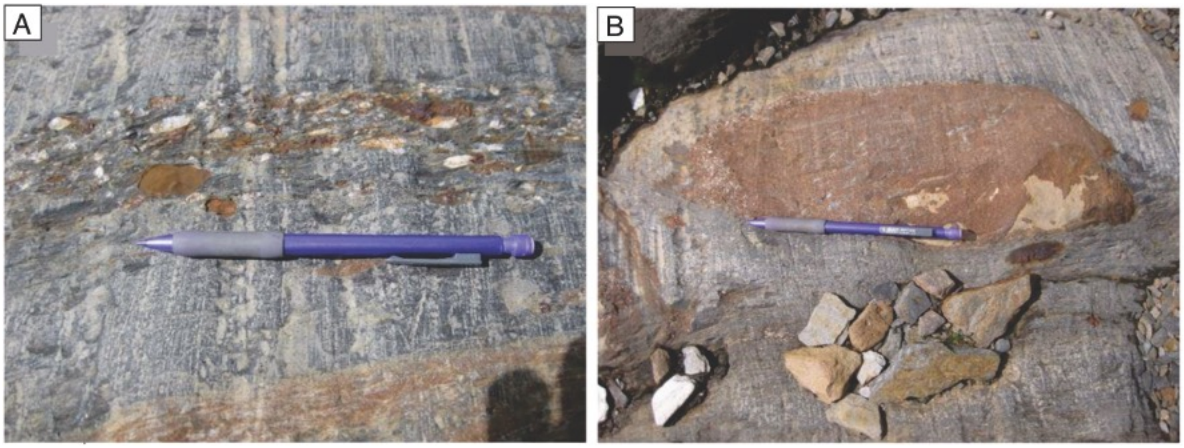

Figure 4.34. D4 in CCN. A) Carbonate-cemented sandstone clast. B) Quartz pebbles and carbonate clasts. From Bergen (2017).

4.4.3 Interpretation

In a deep-marine system, failure commonly occurs at the shelf-slope break, the upper slope, and locally on the inclined margins of levees. Early work by Posamentier and Kolla (2003) suggested that sand-prone MTDs were sourced from shelf-edge deltas whereas mud-prone MTDs consist of fine-grained sediments derived from the slope. Later work by Moscardelli & Wood (2008) proposed a two end-member classification for mass transport deposits in offshore Trinidad: attached and detached. Based on that work, in addition to a follow-up compilation of over 300 MTD worldwide, Moscardelli and Wood (2016) suggested that attached MTDs are areally expansive features that typically are > 1000 km^2, which then are further subdivided into shelf-attached and slope-attached types. Shelf-attached MTDs are related to failure of the outer shelf; these MTDs are sourced from the shelf-edge delta and controlled by fluctuations in sea level and high sedimentation rates that destabilize the outer shelf. Slope-attached MTDs are related to failure of the upper slope caused by discrete regional catastrophic events like earthquakes and volcanism, and are sourced from a collapsed part of the upper slope. Downslope, shelf- and slope-attached MTDs are geomorphologically similar, however closer to the shelf-slope break they differ. Shelf-attached MTDs (Figure 4.35B) are commonly associated with sediment-funnelling canyons and aggradational or progradational clinoforms, whereas scarps up to tens of km long and hundreds of m deep characterize the proximal area of slope-attached MTDs (Figure 4.35A). In contrast to attached MTDs, detached MTDs are 10s of km^2 in area and therefore significantly smaller than attached MTDs. These features are associated with localized gravitational instabilities resulting in the failure of part of the slope, levees, or the flanks of diapirs, and are composed of locally sourced sediment.

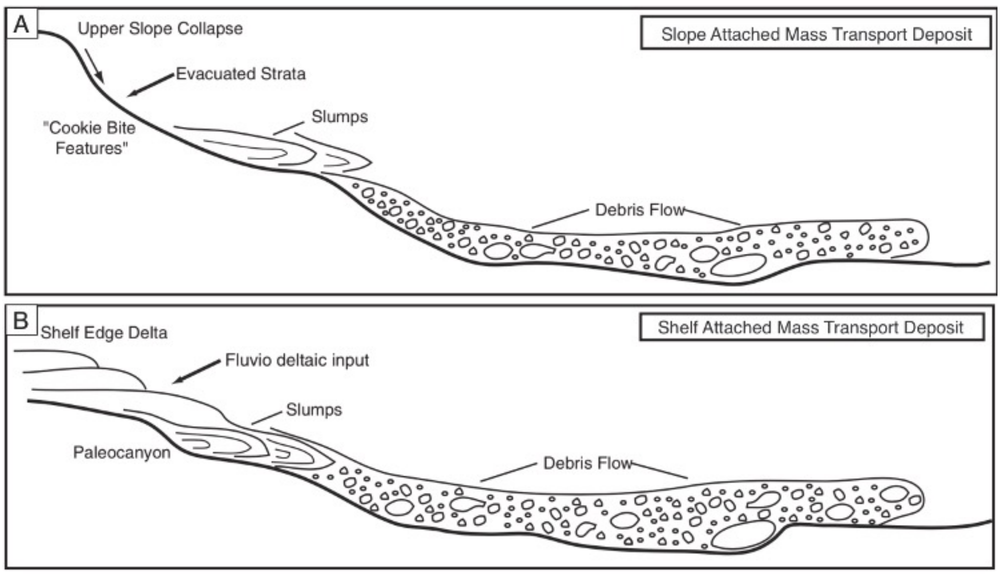

Figure 4.35. Processes associated with the two types of MTDs. A) Slope-attached MTDs are sourced from the upper slope following collapse. B) Sediment in shelf-attached MTDs is sourced directly from shelf-edge delta, failure is a result of elevated sedimentation rates and/or RSL fluctuations (Moscardelli and Wood, 2008).

MTD 2 and D1/D2/D4 of MTD 4 are interpreted to be shelf-attached mass transport deposits that coincided with mass wasting on the slope during the late falling stage and lowstand systems tracts. The mud-rich nature of these debrites imply a slope-derived sediment source, however the commonality of stromatolite and oolite fragments suggests erosion up to the shelf-edge and beyond into shallow-water (Laurin et al., 2007; Arnott et al., 2011). In addition, the anomalous abundance of quartz pebbles suggests remobilization of coarse-grained shelf edge relict sediment during relative sea level fall. Furthermore, the position of MTD 2 between ICC2 and ICC3 and D1/D2 between channel units IC4.5.2 and IC4.5.3 implies deposition immediately before lowstand (Posamentier & Kolla, 2003). An MTD that bears similarity to MTD 2 and D1/D2 was described by Pickering and Corregidor (2005) in the Ainsa Basin, Spanish Pyrenees. These authors identified three types of MTDs (I-III) that exhibit a range of facies related to flows that display properties of debris flows, slides/slumps, and turbidity currents. Type II MTDs typically consist of a basal clast-supported pebble conglomerate (e.g., MTD 2 red unit, see fig above) overlain by a chaotic, mud-rich, matrix-supported conglomerate analogous to the bulk of MTD 2 and D1/D2/D4 strata. Due the complex range of facies in type II MTDs, Pickering and Corregidor (2005) suggest deposition by a multiphase granular flow (Figure 4.36) whereby a single flow consists of three components: a basal sand- and gravel-rich layer overlain by a high-concentration mud-rich layer analogous to a debris flow, and finally an overlying dilute suspension. Type II MTDs are interpreted to represent the collapse of the upper slope and outer-shelf during sea level fall, and therefore consistent with the shelf-attached derivation of MTD 2 and D1/D2.

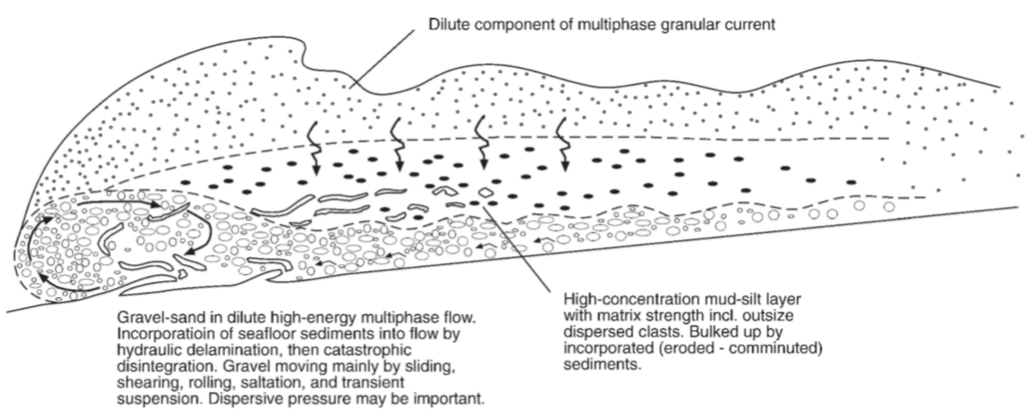

Figure 4.36. Multi-phase granular flow that deposits a bipartite bed consisting of a gravel-rich basal layer overlain sharply by a matrix-supported mud-rich layer characteristic of Type II MTDs. Multi-phase granular flows (and their deposits) exhibit attributes associated with both debris flows and turbidity currents (Pickering & Corregidor, 2005).

MTD 3, S1/S2 and D3 of MTD 4 are interpreted to be detached mass transport deposits related to gravitational instabilities along canyon or channel walls. The presence of rafted coarse-grained sandstone blocks and medium- to thin-bedded upper division turbidites suggests that a portion of the channel wall (proximal levee) or canyon wall that was composed of semi-consolidated sandy channel sediments detached and moved downslope as a slide. Failure was likely a result of down-flow erosion that over-steepened the walls, rendering it gravitationally unstable. Alternatively, slides within MTD 2 are interpreted to be associated with shelf-edge failure based on the incorporation of abundant carbonated-cemented clasts and its position within MTD2.

The common association of slides and debrites at Castle Creek, specifically the superposition of shelf-attached debrites over slides, suggests that they may occur as evolutionary stages during canyon formation. Puga-Bernabeu et al. (2011) describe two types of submarine canyons along a passive margin in north-eastern Australia (Great Barrier Reef): shelf-incised (Figure 4.37A) and slope-confined (Figure 4.37B) canyons, where canyon heads of shelf-incised type intersect the shelf-edge whereas slope-confined canyon heads do not (i.e., blind-headed). Shelf-incised canyon formation is related to extensive erosion during relative sea level fall and lowstand, whereas slope-confined canyons are the result of slope failure and subsequent headward erosion.

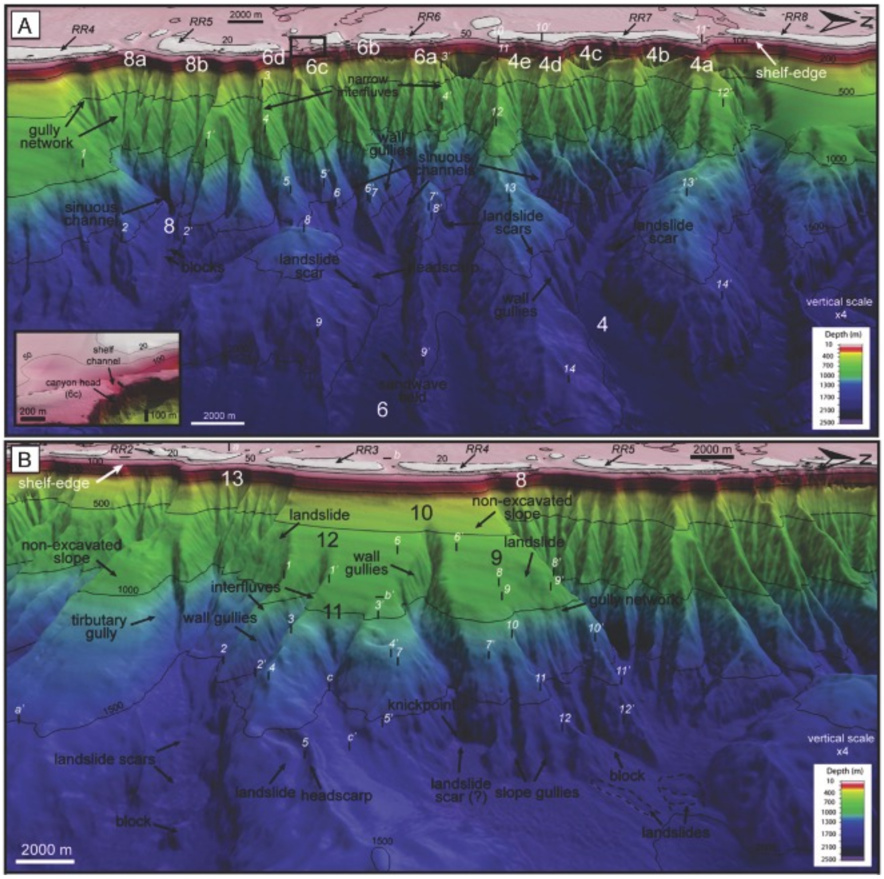

Figure 4.37. Canyons in the Ribbon Reef region of north-eastern Australia. A) Shelf-incised canyons (large white numbers). Inset depicts a close-up (5 m resolution) of a canyon incised into the shelf-slope break. B) Slope-confined canyons (large black numbers) (from Puga-Bernabeu et al., 2011).

They propose a 4-phase model for canyon formation which utilizes both shelf-incised and slope-confined canyon formation mechanisms. Initial slope failure results in formation of an incipient headscarp and translation of slide blocks downslope (phase 1a, Figure 4.38A-B. Phase 1a failures are caused by local gravitational instabilities such as oversteepening or under-consolidation of sediment (detached MTDs of Moscardelli and Wood, 2008). This is followed by a phase of headward erosion of the scarp and continued up-slope erosion by progressive destabilizing of strata (phase 1b and 2; Figure 4.38C-D). Phase 3 (Figure 4.38E) is represented by shelf-incised canyons as the headscarp reaches the shelf-edge, and sediment from the river and/or shelf-edge delta is transported to the basin floor. Here, sustained flow through the canyon results in significant erosion and canyon wall collapse (e.g., shelf-attached MTDs with incorporated shelf debris e.g., stromatolites & oolites). The final phase (phase 4; Figure 4.38F) is marked by a change in sediment supply due to partial, complete, or non-existent blocking of the canyon head by the reef (Ribbon Reef). The authors suggest that sediment dynamics of unblocked shelf-incised canyons, specifically sediment-gravity flows, will be strongly influenced by relative sea level fluctuations, similar to the shelf-attached MTDs of Moscardelli & Wood (2008). In terms of relative sea level fluctuations, transition from phase 2 to 3 requires sustained sediment supply to the shelf edge as the shelf-edge delta progrades during falling relative sea level. At this time, shelf-edge failures are likely to occur and incorporate both carbonate material and relict sediment from the staging area. This also provides an explanation for the common superposition of channel complexes over MTDs. Similarly, the phase 4 change in sediment supply may be related to highstand conditions that reduce or terminate sediment supply from the continent, rather than reef-blocking. This model, in combination with observations of stacked slides and debrites at Castle Creek, suggest an evolution from initial slide emplacement by localized failure on the slope followed by shelf-fed debris flows as a result of relative sea level fluctuations.

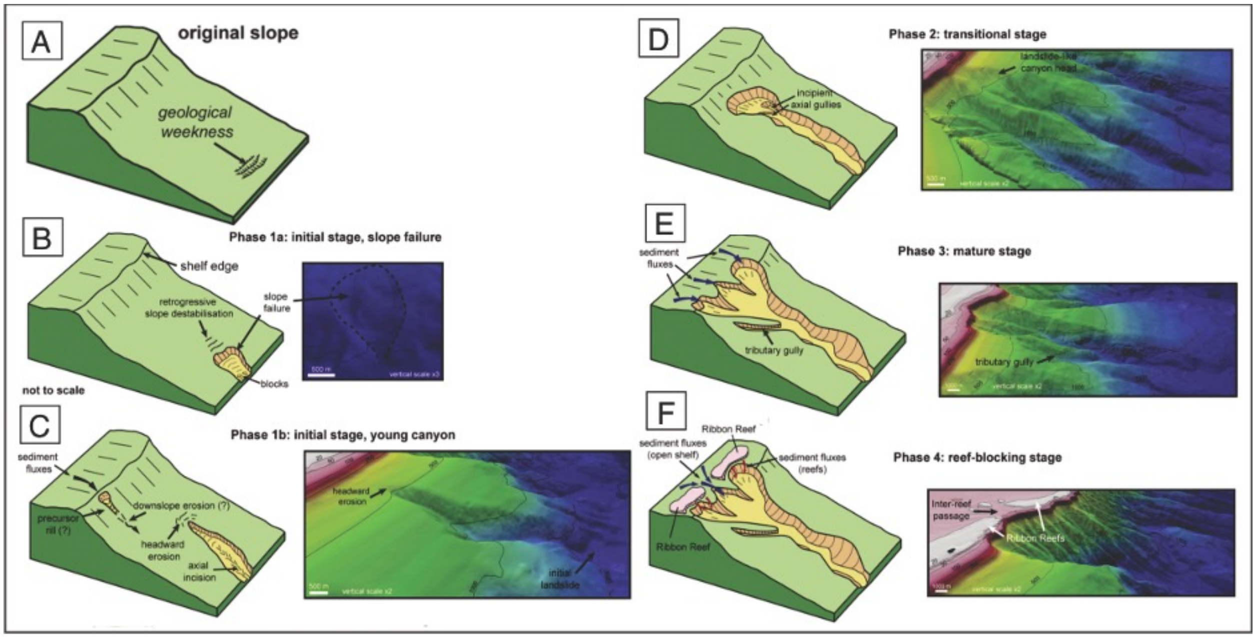

Figure 4.38. Phases of canyon formation and evolution in the Ribbon Reef area in north-eastern Australia. A-B) A weakness in the original slope results in failure during the initial phase. C) Headward erosion of the initial failure and formation of slope canyon. Concomitant down-slope erosion from sediment influx may result in canyon formation from the shelf edge. D) Canyon incises further up-slope during the transition phase. E) Canyon reaches shelf-edge during the mature phase and sediment is supplied directly from the shelf. F) Sediment supply is modified and may be partially or fully blocked by the reef. Sediment may be shelf-fed and/or reef-fed. Modified from Puga-Bernabeu, et al. (2011).

Chapter 5: Geochemical Analysis Results and Discussion

5.1 X-Ray Fluorescence Analysis Results

5.1.1 Major and Minor Elements

Mudstone samples were obtained every 10 m along an ~ 930 m vertical transect through the Hill Section (CC-HS), starting at the first Isaac Carbonate Unit (FIC) to the base of Isaac Channel Complex 6 (ICC6). If mudstone was not present in the 10-m interval, samples were taken from 1 m above or below that point, or that interval was skipped and recorded that mudstone was not present within 1 m of initial sample location. Major element abundance is presented as oxides in mass percent (Table A.1), and therefore represents a relative abundance, and minor element abundance in parts per million (ppm, Table A.2). Herein, a decrease or increase in relative abundance of major elements will be described simply as a "decrease" and "increase" in proxies in order to generalize terminology when discussing both major and minor elements in the following discussions. The molar proportions of a subset of major and minor elements were calculated to discern any possible changes in the major and minor element data set (see Equation A.1 for an example calculation), however no change in trends was observed in comparison to the original data and thus data presented in this thesis does not utilize the calculated molar proportions.

The most abundant major oxides are SiO_2 (average = 53.8%, range = 31.3 – 65.2%) and Al_2O_3 (average = 23.1%, range = 13.8 – 31.8%). MnO is the least abundant major oxide with an average of 0.038%, followed by S at 0.094% (range: 0 - 0.615%). However, CaO is typically 0% with the exception of peaks at 520 m (13.2%) and -270 m to -300 m (7.8 - 17.7%); both coincide with anomalously high LOI values of 18.8 and 16.1, respectively (average LOI in all other samples = 4.8). This peak corresponds to a similarly prominent peak in P2O5 and is associated with a Ca-rich phosphate horizon (francolite). Associated with high CaO is minimum or near minimum values in Na, Al, Si, and Ti, and similarly the Terrigenous Input (Terr. In.) proxy (Al + Ti + K + Na). Notably, Mg has a maximum at 520 m but minimum at -270 m. Fe peaks at 520 m, likely associated with pyrite and elevated levels of organic matter as evidenced by the aforementioned spike in phosphorus, but is at its lowest at -270 m. K and Mn content also peak at 520 m but are of average value at -270 m. Al, Si, Ti, K, and Terrigenous Input exhibit a cluster of peaks between 310 – 370 m. Maxima in Al, Ti, K, and Terrigenous Input are observed whereas Si is at a minimum.

The most abundant minor element is Zr with an average of 231.9 ppm (range = 113 - 491 ppm). Sr and Cr are also among the most abundant minor elements with averages of 149.7 and 140.5 ppm, respectively. Nb and Cu are the least abundant with averages of 26.5 and 30.0 ppm, respectively (ranges: Cu = 0 – 99 ppm, Nb = 15 – 40 ppm). Rb is either absent or below detection limits in all samples. Cr, Sr, and Zr exhibit the highest variability in the data set ranging 45 – 205 ppm (Cr), 66 – 682 ppm (Sr), and 113 – 491 ppm (Zr). The high degree of variability at 520 m and -270 m observed in the major element data (above) are clearly observed in Zr, Sr, and Nb as well. Zr and Nb are lowest at 520 m and -270 m and Sr is highest at 520 m. Zr and Cr exhibit a series of peaks between 310 m to 270 m, coinciding with peaks in Al, Si, Ti, K, and Terrigenous Input.

Pearson Rank Correlation Coefficients were calculated for all major and minor elements (Table 5.1) using the following equation:

$$r = \frac{\sum_i (x_i - \bar{x})(y_i - \bar{y})}{\sqrt{\sum_i (x_i - \bar{x})^2 \sqrt{\sum_I (y_i - \bar{y})^2}}}$$

Elements with the highest correlation are Zn – Fe_2O_3 (r = 0.829), Y – K_2O (r = 0.817), and Nb – Y (r = 0.806). Conversely the lowest correlations are Fe_2O_3 – P_2O_5 (r = -0.005), Y – S (r =

0.006), Y – Cr (r = -0.015), and P_2O_5 – Na_2O (r = -0.015). Elements with the strongest inverse relationship are Fe_2O_3 – K_2O (r = -589) and K_2O – Na_2O (r = -0.588).

Table 5.1. Pearson Rank Correlation Coefficients of major and minor elements. Minimum values in each row are highlighted in blue and statistically significant values (over 0.7) in green.

	Na_2O	MgO	Al_2O_3	SiO_2	P_2O_5	K_2O	CaO	TiO_2	MnO	Fe_2O_3	S	Cr	Cu	Zn	Sr	Y	Zr	Nb
Na_2O	1	0.065	0.130	0.016	-0.015	-0.588	-0.143	-0.153	-0.045	0.356	-0.088	0.310	0.305	0.548	0.325	-0.435	-0.375	-0.412
MgO		1	-0.117	-0.389	0.163	-0.385	0.198	-0.333	0.797	0.717	0.217	0.079	0.290	0.436	0.495	-0.298	-0.319	-0.421
Al_2O_3			1	-0.512	-0.106	0.483	-0.373	0.725	-0.319	0.097	-0.403	0.798	-0.157	0.141	-0.018	0.368	0.160	0.304
SiO_2				1	-0.288	-0.169	-0.521	-0.149	-0.446	-0.284	-0.217	-0.426	-0.130	-0.128	-0.668	-0.135	0.153	0.086
P_2O_5					1	-0.099	0.433	-0.208	0.282	-0.005	0.136	-0.108	0.019	-0.098	0.418	0.156	-0.030	-0.155
K_2O						1	-0.180	0.702	-0.395	-0.589	-0.072	0.081	-0.461	-0.632	-0.405	0.817	0.608	0.786
CaO							1	-0.476	0.559	-0.083	0.547	-0.344	0.210	-0.145	0.694	-0.142	-0.271	-0.300
TiO_2								1	-0.517	-0.182	-0.374	0.591	-0.275	-0.148	-0.410	0.598	0.698	0.692
MnO									1	0.453	0.405	-0.191	0.303	0.141	0.717	-0.306	-0.342	-0.484
Fe_2O_3										1	-0.027	0.416	0.388	0.829	0.299	-0.472	-0.374	-0.478
S											1	-0.364	0.237	-0.162	0.347	0.006	-0.114	-0.120
Cr												1	0.033	0.522	0.045	-0.015	0.087	-0.029
Cu													1	0.422	0.343	-0.314	-0.193	-0.325
Zn														1	0.192	-0.591	-0.371	-0.538
Sr															1	-0.288	-0.488	-0.511
Y																1	0.618	0.806
Zr																	1	0.654
Nb																		1

5.1.2 Elemental Ratios

The Si/Al, Zr/Al, and Zr/Nb ratios are used to evaluate changes in sediment supply, specifically the abundance of coarse-grained sediment — Al and Nb being a proxy for clay abundance and Si and Zr for coarse-grained detrital sediment (Table A.3) (Sano et al., 2013; Lagrange et al., 2020). Zr/Al shows the most variability with a range of 5.06 – 23.5 ppm (average = 10.2 ppm). Si/Al varies between 1.33 – 4.06 ppm with an average of 2.40 ppm and Zr/Nb has a range of 5.38 - 15.8 ppm with an average of 8.74 ppm. All three grain size proxies show an overall increasing trend, indicating a progressive increase in grain size. Ti/Al reflects the degree of continental sediment supply to the basin based on the amount of Ti-bearing heavy minerals, like rutile and ilmenite, compared to less dense minerals, like Al-bearing clay minerals, that settle more slowly, and mark times of reduced continental input (Chen et al., 2013). The

Ti/Al data varies between 0.021 – 0.056 ppm (average = 0.041 ppm) and exhibits a slight increasing upwards trend towards more sediment supplied from the continent.

5.1.3 Weathering Indices

Major element geochemistry of mudstones is strongly influenced by chemical weathering (Fedo et al., 1995). The degree of chemical weathering can be quantified using four indices of alteration (see section 5.2.2 and Table A.4 for complete results): The Chemical Index of Alteration (CIA), the Chemical Index of Weathering (CIW), the Index of Compositional Variability (ICV), and the Plagioclase Index of Alteration (PIA) (Fedo et al., 1995). The CIW and PIA have the highest average of the weathering indices at 94.0 and 92.7, respectively. The CIW ranges between 49.0 – 99.0 and the PIA between 42.5 – 98.6. The CIA has an average of 78.5 and varies between 44.2 – 84.4. The ICV, as a consequence of the variables in the calculation, is low with an average of 0.779 and range of 0.506 – 2.48. In general, the data vary little with the exception of peaks at 520 m, -270 m, and -300 m caused by anomalously high values in Ca (CIA, CIW, PIA) and Ca, Fe, Mg, and Mn (ICV) (Figure 5.1). Excluding the outliers, the CIA decreases upwards, suggesting progressively less intensely weathered sediment, up to 400 m beyond which the data remains constant. The CIW and PIA have very similar trends in which they are decreasing up until ~ -50 m, remain constant from -50 m to 50 m, increase from 50 m to 400 m, and then remain relatively constant beyond 400 m. The ICV, however, exhibits a more cyclical trend with minima at ~ -100 m and 400 m and maxima at -170 m and 530 m. The opposite trend in CIA compared to CIW and PIA likely reflect the absence of K in the CIW and PIA calculation (see equations 2 and 4 below), as K increases significantly between 50 m and 400 m (see discussion below).

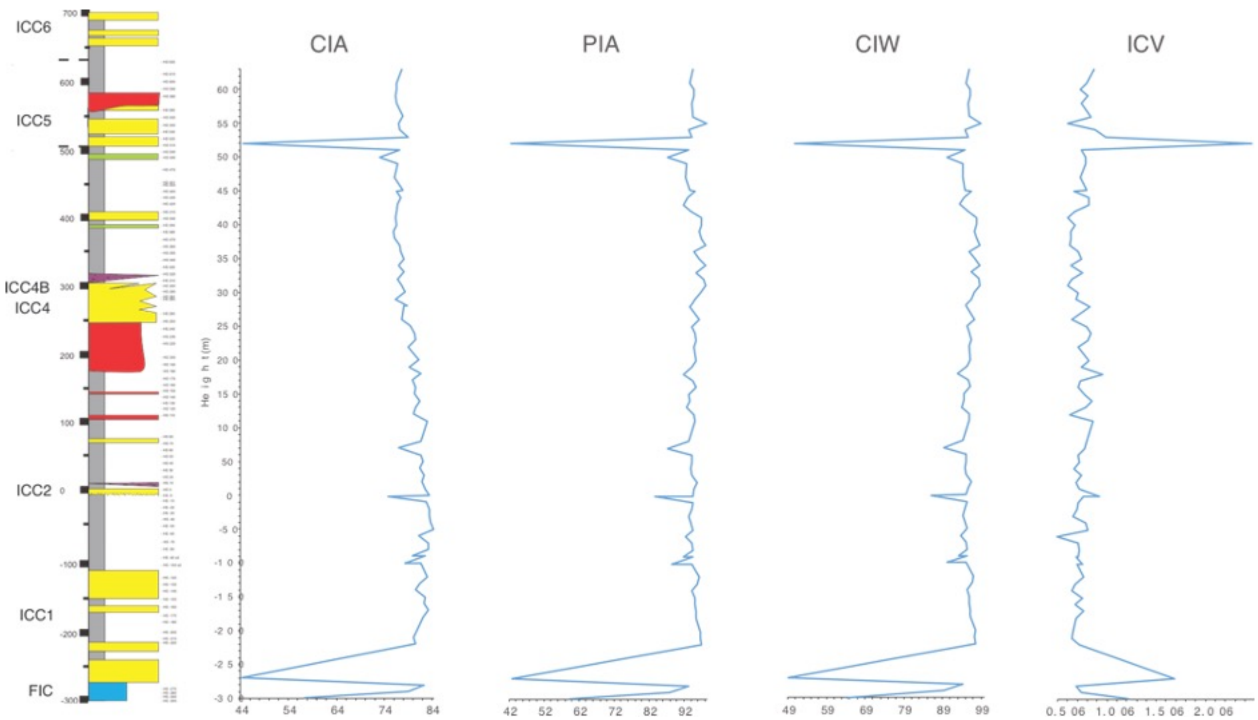

Figure 5.1. Weathering indices and stratigraphic column of CCHS. Note, the two major minima (maxima in ICV) across all four datasets correspond to elevated carbonate content associated with the first Isaac carbonate (FIC) and a Ca-rich fluorapatite horizon in ICC5.

5.2 X- Ray Fluorescence Analysis Discussion

5.2.1 Overview

Chemostratigraphic analysis has become increasingly used to study mudstones where lithological variability may be too subtle to observe without labour-intensive and time-consuming thin section analysis (e.g., Pearce et al., 1999; Sano et al., 2013; Nyhuis et al., 2015; Turner et al., 2016). The geochemistry of sediments is largely controlled by factors like provenance, tectonic setting, and depositional environment (e.g., Roser & Korsch, 1986; Armstrong-Altrin et al., 2004; Sinha et al., 2007; Zaid, 2016; Tao et al., 2017). Elements that are used to evaluate the effect of these factors include, but are not limited to, Ti, Zr, Al, Si, K, Sr, and Ca. Continentally derived sediments are commonly enriched in Ti, Zr, and Si (Lagrange et al., 2020). Zr and Ti are typically associated with detrital zircon ($ZrSiO_2$) and Ti-oxides such as rutile and ilmenite that commonly occur in the silt- to sand-size fraction and inclusions in detrital quartz (Pearce et al., 2005). Although Si is generally a measure of the abundance of all silicate minerals, Si in quartz dominates in most detrital sedimentary systems. However, Si can also be biogenic in origin (sponge spicules, diatoms, radiolaria), but due to their age (Neoproterozoic), rocks of the WSG contain no biogenic silica. K and Al are commonly associated with illite/mica and kaolinite, respectively, in addition to high Zn and Rb concentrations, which also can be associated with elevated illite and mica content (Pearce et al., 1999; 2005). Ca, Mg, and Sr have been interpreted as proxies for carbonate accumulation, and respectively, the minerals calcite, dolomite, and aragonite (Pearce et al., 2005; Sano et al., 2013; Turner et al., 2016).

Proxies for grain size include Zr/Al and Zr/Nb ratios, where Zr is contained in dense heavy minerals that settle faster than lower density, but equally important, sheetlike Al- and Nb-bearing clay minerals (Sano et al., 2013; Lagrange et al., 2020). Ti/Al ratio is also taken to be a measure of continental sediment supply and may also reflect changes in grain size, as Ti is present in heavy minerals such as rutile, ilmenite and titanite (Chen et al., 2013; Zaid, 2016). Similarly, the Si/Al ratio is commonly used as a measure of quartz versus clay, or more specifically, the amount of detrital quartz versus aluminosilicates (clay minerals being the most common aluminosilicate in the mud-size fraction) (Ratcliffe et al., 2007; Turner et al., 2016).

The use of geochemical properties, including bulk composition, element abundance, and elemental ratios allows one to distinguish and characterize stratigraphic units based on observable trends (Ramkumar et al., in press). For example, Nyhuis et al. (2016) identified depositional units based on X-Ray Fluorescence (XRF) data. These authors described a transgressive unit characterized by low Si/Al values, indicating elevated clay content, and higher Ti, Zr, and K values compared to underlying limestones, suggesting this unit is more enriched in continental detrital material and the limestones likely represent a drowned carbonate platform. Additionally, Turner et al. (2016) showed that transgressive systems tract (TST) mudstones at the base of the Woodford Shale (Oklahoma, USA) exhibit a progressive decrease in Ti upward from a sequence boundary, interpreted to reflect the progressive decrease in sediment derived from the continent. The TST is also characterized by the highest values of Ca and Sr, indicating the significant contribution from a carbonate source. The ensuing regression associated with the highstand systems tract (HST), is marked by increasing Ti, Zr, K, and Al associated with increasing input of continentally derived sediment up to the sequence boundary that caps the Woodford Shale.

5.2.2 Provenance (Weathering)

The geochemistry and mineralogy of siliciclastic sediment is affected by chemical weathering (Fedo et al., 1995). The degree of source-rock chemical weathering can be estimated based on the relative proportions of aluminum, calcium, sodium, and potassium. Nesbitt & Young (1982) suggested that because calcium, sodium, and potassium cations are removed from feldspars during weathering, the relative proportion of aluminum should increase with the intensity of chemical weathering and be reflected in the Chemical Index of Weathering (CIA), with higher values indicating more intensely weathered source rock:

(1) $CIA = [Al_2O_3/(Al_2O_3 + CaO + Na_2O + K_2O)] * 100$

In this study the CIA typically varies between 73 and 84 (Figure 5.1) suggesting a highly weathered source. Additionally, the ternary diagram for WSG mudstones (Figure 5.2A) also suggest a highly weathered source, as the samples are aluminum-rich relative to calcium, sodium, and potassium.

The Chemical Index of Weathering (CIW) (Harnois, 1988; Maynard, 1992) is identical to the CIA except that it eliminates K2O because of K-metasomatism; a diagenetic process whereby the influx of K-rich basinal fluids results in the progressive increase in K content (Ennis et al., 2000). The CIW is defined by:

(2) $CIW = [Al_2O_3/(Al_2O3 + CaO + Na_2O)] * 100$

While the CIW gives an approximation of the degree of weathering of a sample, Fedo et al. (1995) point out that, because it does not take into account aluminum in K-feldspar, the CIW gives an apparent value that is significantly higher than the CIA for K-feldspar-rich rocks. For example, unweathered potassic granite has the same CIW (80) as residual weathering products such as smectite.

The Index of Compositional Variability (ICV) was proposed by Cox et al. (1995) to measure the relative abundance of aluminum versus other common cations:

(3) $ICV = (Fe_2O3 + K_2O + Na_2O + CaO + MgO + MnO + TiO_2)/Al_2O_3$

Since Al is in the denominator rather than numerator of the ratio immature, slightly weathered rocks will have a high ICV value, whereas the CIA and CIW will be low. The ICV is a useful measure of compositional maturity that can be extended to tectonic setting; high ICV, immature mudstones associated with active tectonic settings; low ICV, mature mudstones more commonly linked to areas with active sediment recycling (i.e., passive margins) or intense chemical weathering (Cox et al., 1995).

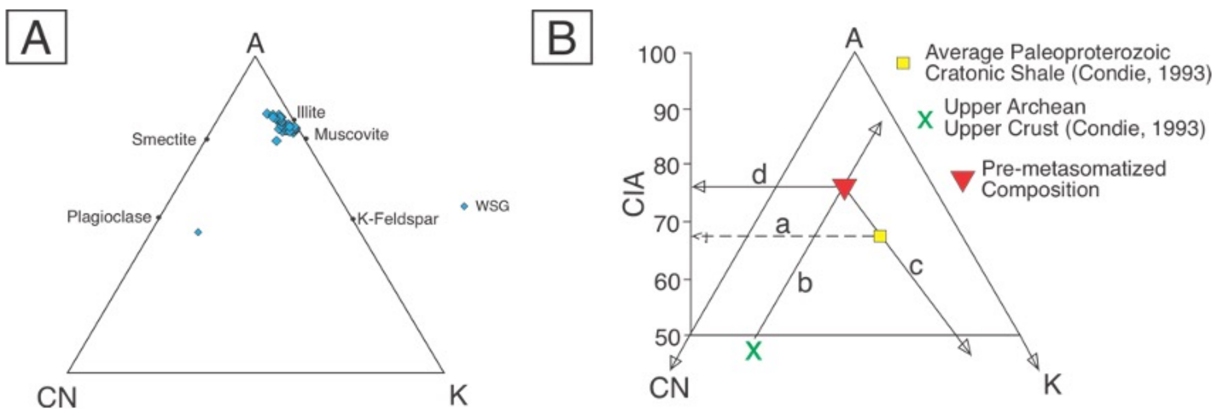

Figure 5.2. A) A-CN-K (Al_2O_3 – $CaO+Na_2O$ – K_2O) diagram of WSG samples (blue diamonds) clustering in the illite region. B) A-CN-K diagram to determine CIA of pre-metasomatized mudstones (modified from Fedo et al., 1995).

Finally, Fedo et al. (1995) modified the CIA equation to accurately measure the degree of weathering of a sedimentary rock before K-enrichment, termed the Plagioclase Index of Alteration (PIA):

(4) $PIA = (Al_2O_3 – K_2O)/(Al_2O_3 + CaO + Na_2O – K_2O) * 100$

The PIA corrects for the addition of K_2O into mudstones during K-metasomatism where aluminous clays, like kaolinite, are altered to illite or plagioclase to K-feldspar (Fedo et al., 1995). As noted above, K-rich fluids that cause K-metasomatism are likely derived from alkaline saline water within extensional basins (Chapin & Lindley, 1986), or from H-metasomatized basement rocks wherein K replaces H in circulating meteoric waters to produce low-grade metamorphic assemblages (Chapin & Glazner, 1983; Glazner, 1985). Figure 5.2B illustrates the CIA of average shale (yellow square) and continental crust (green X) before K-metasomatism. Dashed line “a” shows the CIA of shale and solid line “b” shows the weathering trend of Upper Archean crust that shifts towards the K-apex (solid line c) during K-metasomatism. The intersection between lines b and c represents the pre-metasomatism composition of the continental crust from which the CIA is determined (solid line d). In Figure 5.2A WSG mudstones plot near the end of the predicted weathering trend of continental crust suggesting intense weathering (PIA ~ 90). Notably, the lower average CIA value (78.5), suggesting less intense weathering, reflects the inclusion of total K (original + metasomatic) in the calculation. This, then, suggests that PIA may provide the best estimate of weathering (average PIA = 92.7). The consistently high CIA, PIA, CIW (~ 73 - 98) and low ICV (0.5-0.8) suggest that WSG mudstones were derived from source rocks that had undergone intense weathering. Such weathering suggests a humid, tropical climate (Nesbitt & Young, 1982; Tao et al., 2017), which is consistent with paleogeographic reconstructions that place the WSG near the equator during the Neoproterozoic (Li et al. 2013) (Figure 5.3A). Additionally, WSG samples cluster at the aluminum-rich end of the predicted weathering trend for Upper Archean crust (Figure 5.2) and in the felsic field of the TiO_2 vs. Zr plot (Figure 5.3B), where low Ti and high Zr (felsic Ti/Zr < 4 compared to mafic Ti/Zr ~19 and intermediate Ti/Zr ~12) suggest an evolved sediment source (Paulick & McPhie, 1999; Zaid, 2016).

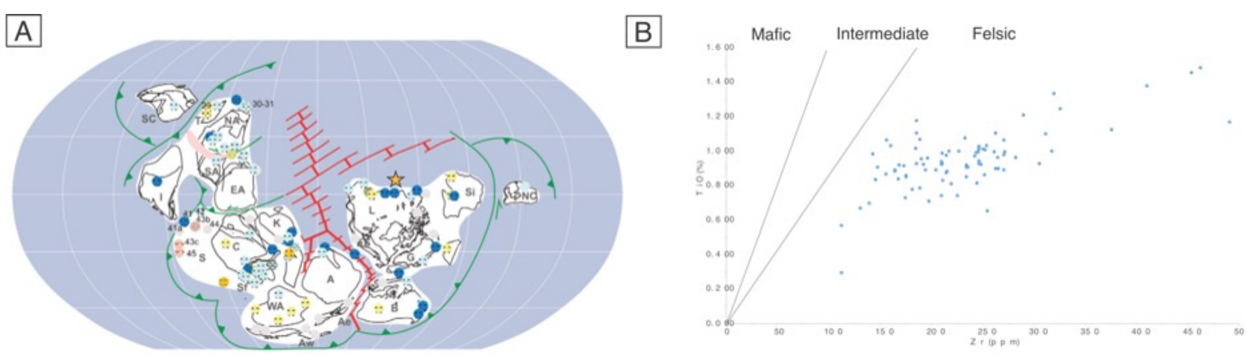

Figure 5.3. A) Location of the WSG (orange star) near the equator during the Neoproterozoic breakup of Rodinia (Li et al., 2013). B) WSG data points plot in the felsic field of the Zr vs. TiO_2 chart (after Paulick and McPhie, 1999).

5.2.3 Tectonic Setting

Deep-water strata of the WSG form a several-km-thick, upward-shoaling depositional wedge that accumulated along the passive margin of western Laurentia. More specifically, this succession is interpreted to represent the progradation of the Laurentian continent margin into the developing proto-Pacific Ocean during the break-up of supercontinent Rodinia (Ross et al., 1995; Hadlari et al., in review). Roser and Korsch (1986) showed that SiO_2 content and K_2O/Na_2O ratio in sandstones and mudstones is related to tectonic setting, based partly on observations in greywackes by Middleton (1960), where $K_2O/Na_2O > 1$ indicates more tectonically stable settings. Moreover, compositionally mature sandstones should be comparatively enriched in quartz, and according to the various weathering indices (see above), mature/weathered mudstones should be more enriched in K and lower in Na as plagioclase is converted to K-feldspar. It follows that along passive margins, sediments are sourced from mature, quartz-rich, and tectonically stable continents (Roser & Korsch, 1986). For example, the Greenland Terrane (New Zealand) consists of argillites and quartz-rich (> 65% quartz) greywackes that plot mainly in the passive-margin field of the SiO_2 vs. K_2O/Na_2O diagram (Figure 5.4A), consistent with previous interpretations of a quartzose sedimentary continental source (Nathan, 1976; Roser & Korsch, 1986). In contrast, the quartz-intermediate (15-65% quartz) schists of the Haast Schist terrane (New Zealand) and quartz-poor (< 15% quartz) sandstones of the Murihiku terrane (New Zealand) plot in the active margin and oceanic arc fields, respectively (Figure 5.4B-C; Roser & Korsch, 1986). Mudstones of the WSG generally cluster in the passive margin field (Figure 5.4D), with three outliers in the active margin field, consistent with previous interpretations of WSG deposition along a passive continental margin.

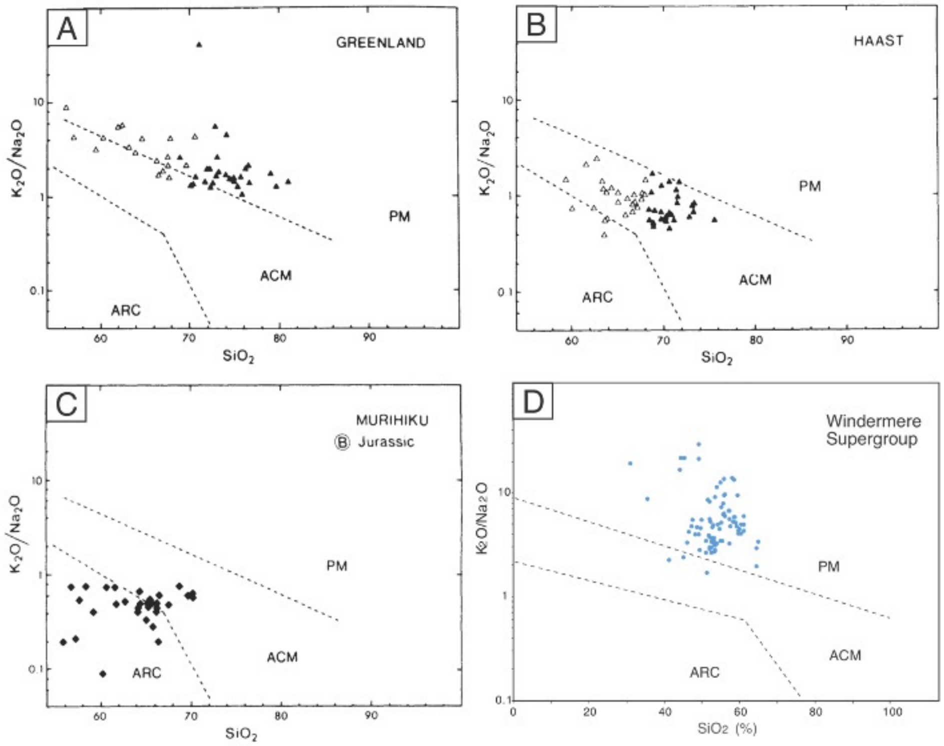

Figure 5.4. SiO_2 vs. K_2O/Na_2O diagrams from Roser and Korsch (1986). A) Greenland terrane argillites (open triangles) and greywackes (filled triangles) plot primarily in the passive margin (PM) field. B) Haast Schist terrane pelitic schists (open triangles) and psammitic schists (filled triangles) deposited in an active continental margin setting (ACM). C) Murihiku terrane sandstones deposited in magmatic island arc tectonic setting (ARC). D) Windermere Supergroup shale plot in the passive margin field.

Chapter 6: Discussion and Conclusions

6.1 Deep Marine Sequence Stratigraphy – Overview

Sediment supply to the deep-marine is dependent on the position of the shoreline and its response to changes in relative sea level (RSL). Changes in sedimentation style as a result of changes in accommodation and RSL fluctuations can be described using sequence stratigraphy; a stratigraphic tool that focuses on identifying key bounding surfaces to determine the sequence of events that build-up the pattern of stacked stratal elements (Catuneanu et al., 2009). Stacking of such elements can be described in terms of four systems tracts (Highstand, Falling Stage, Lowstand, and Transgressive Systems Tracts; HST, FSST, LST, and TST, respectively) that comprise a distinct geometry and assemblage of facies. Collectively these systems tracts make up a sequence, defined by Cantuneanu et al. (2009), as a succession of strata deposited during a cycle of change in accommodation.

With rising RSL during the HST, sediment flux outpaces the rate of accommodation increase. At this time, sediment is deposited mostly by pelagic settling resulting in the development of a condensed section (Figure 6.1). In carbonate settings, on the other hand, flooding of the shelf during transgression may establish optimal conditions for carbonate production that then becomes remobilized down the continental slope with calciturbidite deposition in the basin – a condition termed “highstand shedding” (Jorry et al., 2010; Harper et al., 2015). As RSL falls during the ensuing FSST, increased exposure and erosion of the continental shelf, in addition to shallowing of the water column and local pore-fluid overpressure, creates gravitationally unstable conditions on the outer shelf and upper slope, which commonly leads to the mobilization of large volumes of sediment and carbonate accumulated during the previous HST as cohesive sediment gravity flows, namely mud-rich debris flows, slumps, and slides (Mulder & Alexander, 2001) (Figure 6.1, point 1). Moreover, subaerial exposure of the shelf will also result in the shut-down of the carbonate factory, if present. In the late part of the FSST, sandy high-density turbidity currents deliver sediment directly from the hinterland to the deep-marine, developing extensive sand-rich frontal splays on the basin floor and aggradational leveed channels on the slope (Figure 6.1, point 2). Due to the low preservation potential of falling stage strata (e.g., instability and erosion of the outer shelf and upper slope), the term "HST" will be used hereafter to refer to both the HST and FSST, particularly in reference to gravitational instability which generally is associated with the FSST.

A sequence boundary (SB) caps the FSST and marks the beginning of the LST, after which RSL begins to rise but initially is usually outpaced by sediment flux. Aggradation within channels continues into the early LST, however deposition in the late LST is dominated by low-density turbidity currents as the rate of RSL rise accelerates and coarse-grained sediment becomes preferentially sequestered on the shelf and only finer-grained sediment is supplied to the basin by low-density turbidity currents (Figure 6.1, point 3) (Catuneanu, 2006). Consequently, the sand/mud ratio progressively decreases relative to that of the late FSST/early LST.

When the rate of accommodation increase outpaces the rate of sediment input a Major Flooding Surface (MAJFS) forms and marks the onset of the TST. Deposition by low-density turbidity currents continues from the late LST into the TST, however these turbidity currents are more dilute and increasingly finer grained (mud-rich) as coarse sediment becomes trapped on the shelf and in landward incised valleys (Catuneanu, 2006). Siliciclastic sedimentation rates decline into the late TST as the shoreline retrogrades; however, carbonate production may resume on the shelf as it becomes flooded. Mud-rich debris flows become more common as the shelf and upper slope becomes loaded by a thickening water column rendering it gravitationally unstable (Figure 6.1, point 1) (Posamentier & Kolla, 2003). The Maximum Flooding Surface (MFS) marks the base of the HST with the accumulation of fine-grained sediment and development of another condensed section.

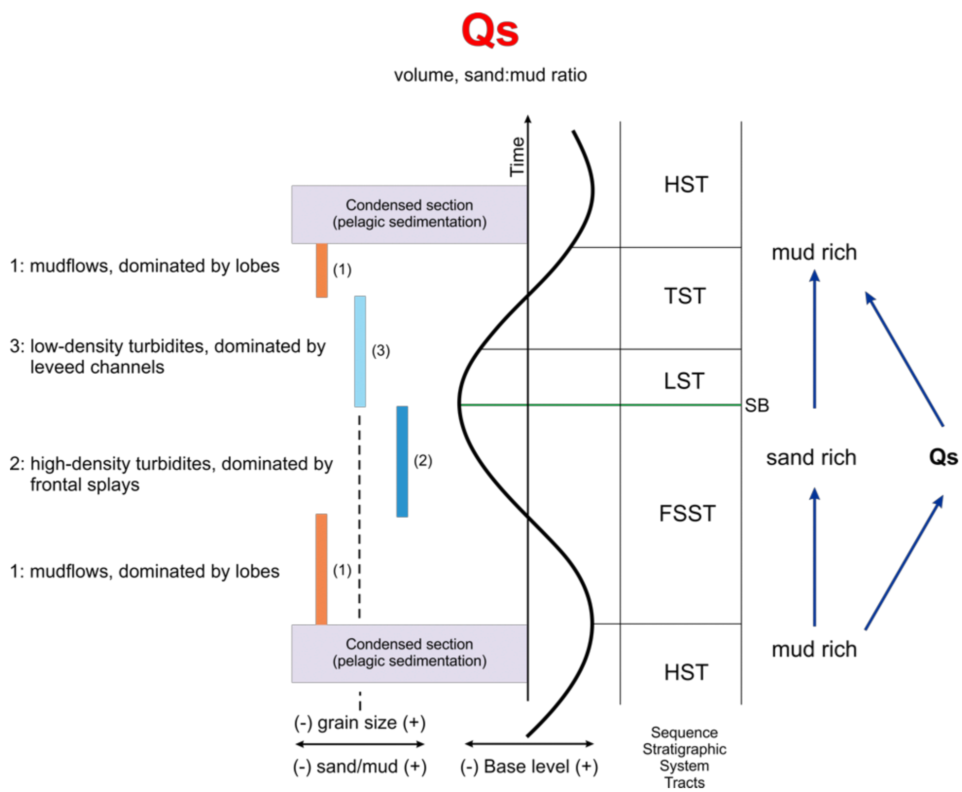

Figure 6.1. Association between sediment gravity flows, stratal elements, and systems tracts during a relative sea level cycle (Fraino, 2020 modified from Catuneanu et al., 2009).

This model relating changes in the character of deep-marine sedimentation directly, or similarly, being “in-phase”, with changes in accommodation controlled by positions of RSL, is the underpinning of existing sequence stratigraphic models for deep-marine sedimentation. However, a recent study by Fraino (2020) and Fraino et al. (accepted) suggested that instead of a single cycle of RSL change, it is the combination of long- and superimposed short-term changes of RSL that control the timing and character of the deep-marine sedimentary record. Most importantly, it is the state of the continental shelf, which during long-term rises of RSL progressively expands in area and therein the ability to more effectively sequester coarse-grained relict and palimpsest sediment. It is this sediment, in addition to the omnipresent hinterland sediment supply, that becomes mobilized to the shelf edge and then resedimented downslope during short-term falls and lowstands of RSL. This change in the granulometric make up of the sediment supply, changes the density structure of the through-going turbidity currents, which then controls the character of leveed slope channels; specifically, aggrading versus laterally accreting channels (Fraino, 2020; Fraino et al., accepted).

6.2 Depositional History of the Study Area

The mixed carbonate-siliciclastic Isaac Formation is interpreted to have been deposited on the passive continental margin of Laurentia as it prograded into the proto-Pacific Ocean during the break-up of supercontinent Rodinia (Ross et al., 1995). At the Castle Creek study area it is composed of at least seven leveed channel complexes informally termed Isaac Channel Complex 0 (ICC0) to Isaac Channel Complex 6 (ICC6) (Figure 6.2). The portion of the Isaac Formation discussed in this study extends from the base of ICC1 through ICC6 and the depositional history of this section is discussed in terms of the four main systems tracts and corresponding sequence stratigraphic surfaces described above, in addition to the lithology and stacking pattern of its component architectural elements. It is important to note that a portion of the CCS geochemical data was obtained from a previous study (FIC to base ICC3 from Milczarek, 2018). However no change in sampling interval or analytical methods occurred between the studies.

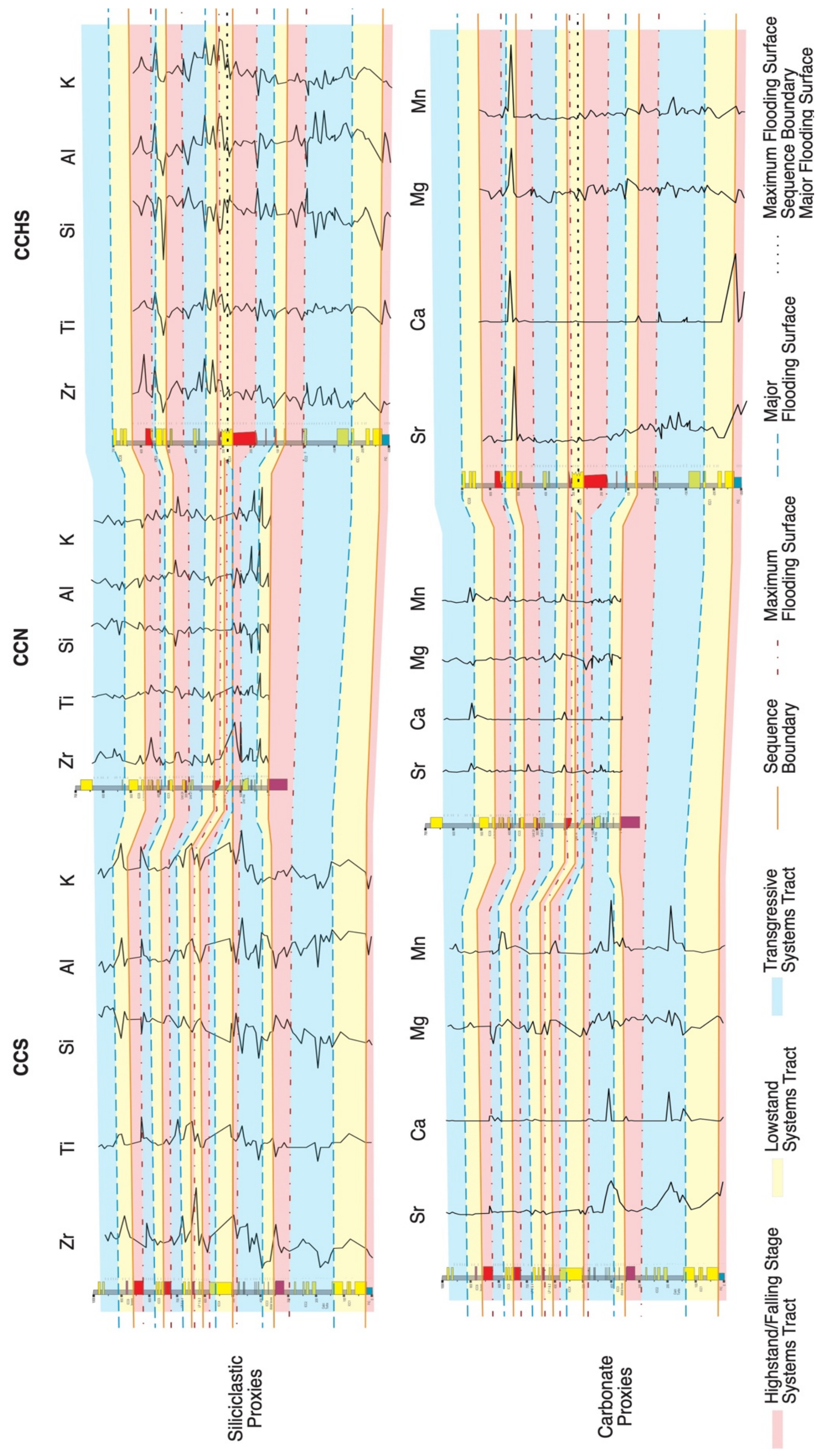

Figure 6.2. Chemostratigraphic correlation of the study area at Castle Creek.

An ~ 200-m-thick mixed siliciclastic-carbonate unit, informally named the first Isaac carbonate (FIC), crops out at the base of the study area, and in part consists of calciturbidites deposited during a RSL highstand (HST). This unit exhibits high strontium (Sr) content that declines upwards into ICC1, illustrating the significant enrichment of carbonate (aragonite) in the FIC compared to the overlying stratigraphy. Peaks in other carbonate proxies (Ca, Mg, and Mn) in this unit also suggest increased carbonate content, but the trends are less well developed. Conversely, siliciclastic proxies (Zr, Ti, Si, Al, K) are relatively low in the FIC. ICC1 overlies the FIC and marks the transition from a siliciclastic-carbonate to siliciclastic system; the contact between the two units is interpreted to be a sequence boundary (SB) and overlies a 30 m-thick pebble conglomerate horizon with abundant carbonate clasts. This horizon (LC-C1 of ICC1, see Aggradational Channel Elements discussion in Section 4.2) immediately underlies the SB and makes up the FSST, indicating intense erosion of the outer shelf and upper slope during a long-term (3rd order?) RSL fall and conditions sufficient to remobilize coarse-grained sediment (quartz pebbles) and carbonate cemented mudstone and sandstone fragments sequestered on the shelf during previous short-term sequences.

ICC1 directly overlies the SB and is composed primarily of amalgamated coarse-grained sandstone interpreted to be a stack of aggradational channel fills deposited by sandy, high-density turbidity currents (Fraino, 2020; Fraino et al., 2021). These aggradational channel elements represent deposition as sediment input outpaced accommodation increase and accordingly make up the LST. In addition, the superposition of ICC1 above FIC has been interpreted by Cochrane et al. (2019) to represent a 3rd order RSL fall correlated with the onset of the 580 Ma Gaskiers glaciation. The LST is characterized by increasing siliciclastic proxies and a decrease in carbonate proxies, further illustrating the dramatic transition from a siliciclastic-carbonate to a mostly siliciclastic system.

Notably, the lower channel units of ICC1 (LC, UC1, UC2) consist of a wide range of grain sizes (clay to pebble) in comparison to the uppermost channel unit (UC3), which is composed of moderately well-sorted, coarse- and very coarse-grained sandstone. This difference in sedimentological character of the lower part of ICC1 represents a change in the granulometric make up of the sediment supply in response to the onset of rising RSL (Fraino et al., accepted). This change manifests as the upwards transition from aggradational (LC, UC1, UC2) to laterally accreting (UC3) channel elements and correlates with the inferred position of the MAJFS. This marks the onset of TST deposition, during which the laterally accreting channel fills of UC3 and ICC2 were deposited. The TST is characterized by an initial significant increase in carbonate proxies, in addition to uncommon calciturbidites, and decrease in siliciclastic proxies. Calciturbidite deposition has been associated with abrupt rises in RSL at glacial terminations as the shelf is re-flooded (Jorry et al., 2010), and in the case of the WSG may indicate the termination of the Gaskiers glaciation that emplaced much of ICC1. Towards the end of the TST, carbonate proxies decline, and siliciclastic proxies increase with the exception of Al, which decreases.

The MFS is characterized by a peak in clay proxies Al and K, suggesting deposition of a condensed interval dominated by fine-grained (mud) sediment. The overlying HST-FSST is characterized by an up to 130 m-thick shelf-attached MTD (MTD 2, see Mass Transport Element discussion in section 4.4). This MTD suggests an episode of slope instability that triggered mass wasting of fine- to coarse-grained sediment, carbonate detritus, including stromatolite and oolite fragments, and resedimentation into the deep sea. Due to the mud-rich, poorly sorted nature of the MTD, trends within both proxy sets remain relatively constant throughout the HST-FSST.

Overlying the MTD are levee elements associated with ICC3. ICC3 crops out in CCSED, and here, like in ICC1, comprises two channel units exhibiting an upward change in channel style. Channel fills in the lower part of ICC3 are aggradational with anomalously coarse-grained sediment, specifically pebble conglomerate with abundant carbonate cemented sandstone and mudstone clasts that characterizes IC3L-C1, interpreted to have been deposited during the late stage of the FSST. These strata are then overlain by a sequence boundary, which coincides with the contact between IC3L-C1 and IC3L-C2. The following LST is characterized by aggradational channel elements and a general decrease in siliciclastic proxy and increase in carbonate proxy content in CCS and CCHS. In CCN siliciclastic proxy values peak and then decrease before the MAJFS.

The MAJFS is characterized by prominent peaks in carbonate proxies and decrease in siliciclastic proxies. Similar to the TST in ICC1, carbonate proxies exhibit an initially exhibit a significant increase in abundance followed by a marked decrease. In CCN and CCHS the trend is more poorly developed, but it is pronounced in CCS, specifically Sr. Sr content in CCS shows two major peaks that coincide with TST units associated with laterally accreting channel elements of ICC1 (UC3), ICC2 (IC2.2, IC2.3), and ICC3 (IC3U-C2) before decreasing and maintaining relatively low abundance throughout the rest of the stratigraphy. Trends in lithology and geochemistry of the FSST – LST – TST transition in ICC3, like those in ICC1, may suggest that the major rise in RSL associated with ICC3 might also be attributed to the same mechanism: glaciation. Rapid and significant rise in RSL during deglaciation initially increased carbonate production on the shelf, however the carbonate factory may have been drowned as RSL continued to rise resulting in a marked decrease in carbonate proxies towards the end of the TST. However, the lack of geochronological constraints and isotope data makes the correlation of these trends with glacial episodes equivocal (Li et al., 2013). Siliciclastic proxies generally become more abundant towards the end of this TST, corresponding to deposition of a laterally accreting channel element associated with ICC3 in CCN.

The MFS following this unit is identified by a decrease in siliciclastic proxies and a low amplitude peak in most carbonate proxies. The overlying HST-FSST is dominated by a detached MTD element (MTD 3), likely emplaced as the thickening highstand water column, in combination with the onset of falling RSL fall, caused the upper slope to become gravitationally unstable, fail and deposited an up to 170-m-thick slide. Geochemical data, therefore, reflect conditions and timing in the place of origin rather than those where and when the slide was deposited.

The SB at the top of the slide marks the onset of the LST and onset of ICC4 deposition. Aggradational channel elements in the lower part of ICC4 (IC4.1-4.3 and HS-IC4.1) comprise the LST in CCS and CCHS, however in CCN only the uppermost, laterally accreting channel unit (IC4.4) crops out. There, the TST overlies the SB due to erosion of the underlying aggradational channel units and/or associated levee deposits. Geochemical data control in ICC4 is poor due to its sand-rich composition and consequently interpretation is problematic, however siliciclastic proxies are higher at the base of ICC4 compared to the top, indicating an overall decrease in hinterland sediment supply from the base of the LST towards the TST. Additionally, the SB at the base of ICC4 marks the point where the abundance of carbonate proxies (at least within this data set) fall to minimum values and remain low through much of the overlying Isaac sediment pile. In CCHS the TST, the overlying MFS, and HST, if present, have been eroded by a younger SB (dotted line in Figure 6.2). The SB correlates with a pebble conglomerate and carbonate clast-rich horizon that crops out in CCSED and CCHS and occurs at the base of channel complex 4B (IC4B). In CCHS IC4B comprises three aggradational channel units (IC4B-1 to 3) and a mud-rich debrite containing dispersed pebbles and carbonate clasts. Here, IC4B makes up the LST and unconformably overlies aggradational channel fills of ICC4 (i.e., the preceding LST). Siliciclastic proxies, with the exception of Si, exhibit a marked increase associated with IC4B, possibly reflecting a major rejuvenation of hinterland sediment supply to the system across all grain sizes.

Notably, detrital zircons in the deep-marine part of the WSG in the SCC exhibit a consistent bimodal Archean (> 2.5 Ga) and Paleoproterozoic (1.7-1.9 Ga modal population) U-Pb age probability distribution except for a single sample at the base of IC4B where the modal age ranges from ~ 2.1-2.3 Ga (Hadlari et al, in review; Figure 6.3). This anomalous sample suggests sediment was derived from areas to the northwest of the WSG deep-marine basin in the southern Canadian Cordillera rather than to the east-southeast, and therein a dramatic, but only temporary change in the hinterland sediment supply.

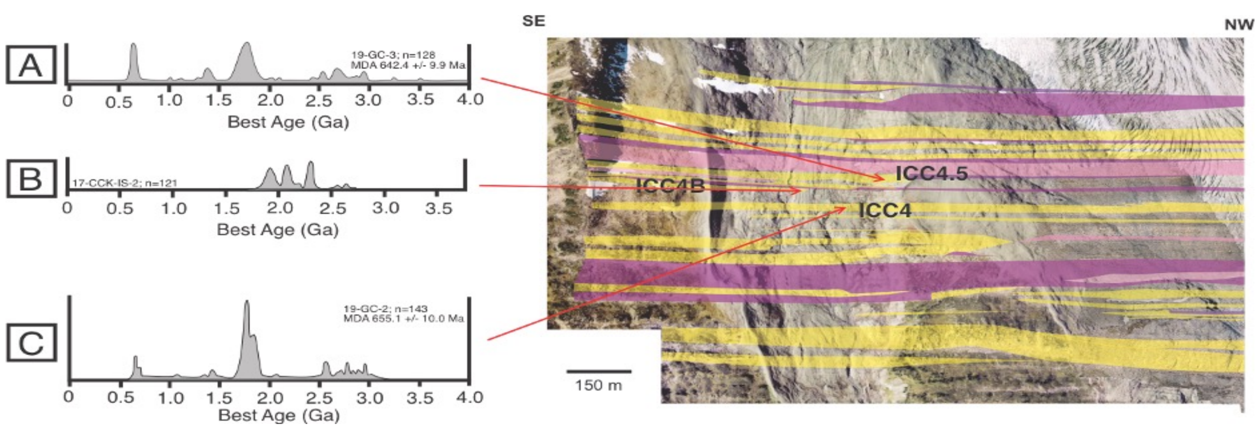

Figure 6.3. Detrital zircon age distribution illustrating the temporary change in provenance between ICC4 and ICC4.5 (B). Note bimodal age distribution in A) and C).

The investigation for a causal mechanism for the provenance change is ongoing, however a possible explanation may be a temporary modification of the continental drainage system in response to glacial advance or retreat. Montero-Serrano et al. (2009), for example, attributed re-routing of Laurentide Ice Sheet (LIS) meltwaters to ice margin instability and fluctuations in ice lobe melt during deglaciation. These authors identified four main sedimentological and geochemical units that corresponded to pulses during a single megaflood event (Figure 6.4). Unit 1 consists of coarse-grained detrital sediment that represents the initial erosive pulse delivering sediment from the Great Lakes area in the northeast (Paleozoic bedrock rich in illite and chlorite, Figure 6.4A). Unit 2 is interpreted to represent a shift in provenance to a more smectite-rich source (Figure 6.4B) derived from Cretaceous, Tertiary, and Pleistocene bedrock in the Mississippi and Missouri river watersheds in the northwest. Unit 2 is interpreted to record the most intense meltwater pulse as the northwestern margin of the LIS retreated significantly. Unit 3, on the other hand, suggests a return to provenance similar to that in Unit 1 (from the northeast), but finer grained, possibly indicating reduced erosion in the late stages of the megaflood event (Montero-Serrano et al., 2009).

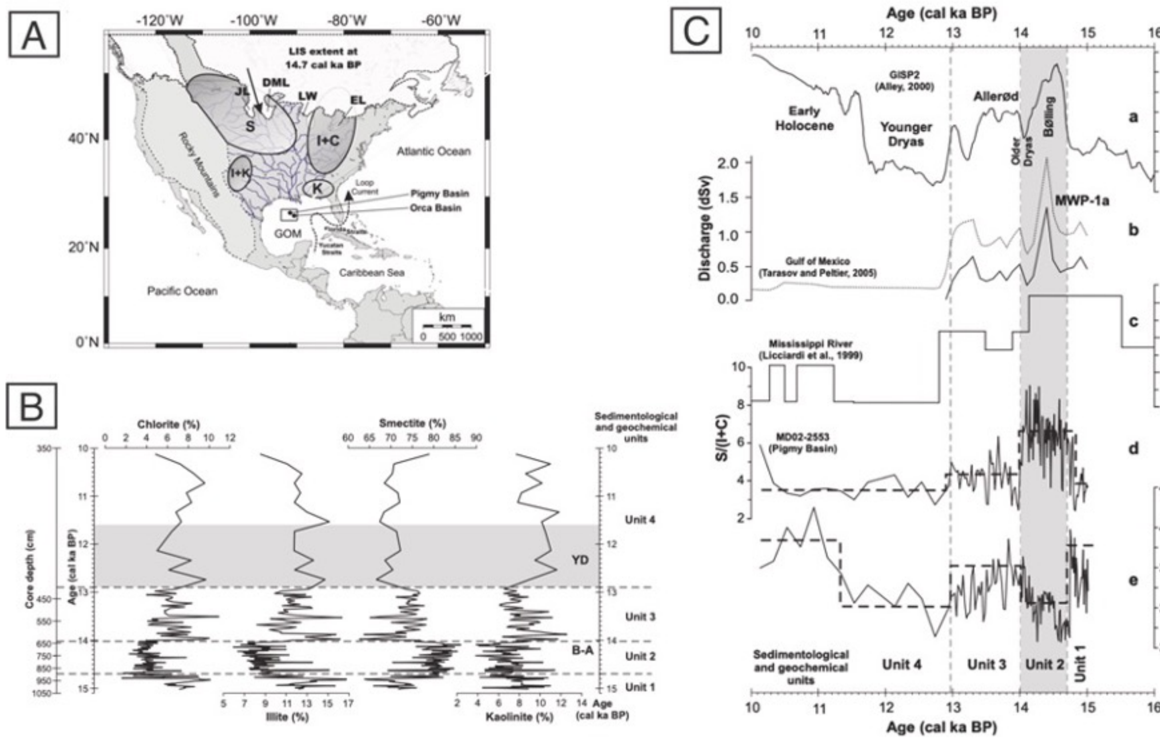

Figure 6.4. A) Map of North America illustrating the extent of the Laurentide Ice Sheet (LIS) during the last deglaciation and main clay mineral regions (at 14.7 ka). B) Variability in clay mineral abundance in a Pigmy Basin core. YD: Younger Dryas cooling period (12.9-11.6 ka, shaded), B-A: Bolling-Allerod warming period (15.4-12.9 ka). C) Sedimentological parameters of the Pigmy Basin core: a) temperature, b) discharge (dotted line includes precipitation over ice-free land), c) Mississippi River meltwater discharge curve, d) clay mineral ratio (smectite/illite + chlorite), e) modal grain size. B-A warming period is shaded. From Montero-Serrano et al. (2009).

Further, Tripsanas et al. (2013) linked peaks in Si, Al, Fe, Ti, Zr, K, and V to Mississippi River discharge events associated with differential melting of two Laurentide Ice Sheet (LIS) lobes. Based on distinct combinations of these peaks the authors determined that the origin and sediment source of four meltwater events varied depending primarily on the state of LIS retreat. Short-lived glaciations in the low latitudes are generally accepted to have occurred during the Neoproterozoic (Li et al., 2013) and may provide a plausible explanation for the temporary change in drainage of the WSG system.

Overlying IC4B is another composite surface containing MAJFS and MFS followed by HST-FSST deposition made up of MTD 4, specifically a detached MTD (S2) overlain by a shelf-attached MTD (D1). S1 is a slide deposit and D1 a debrite composed of quartz pebbles, carbonate-cemented clasts, and stromatolite and oolite fragments in a mudstone matrix. Together, S1 and D1 indicate reactivation of a mixed siliciclastic-carbonate platform followed by gravitational instability and mass wasting (e.g., Puga-Bernabeu et al., 2011). This, then, is overlain by a SB and associated peaks in siliciclastic proxy abundance in levee deposits of ICC4.5 (channel deposits crop out only in CCSED and were not analyzed for geochemistry). Nevertheless, strata at the base of ICC4.5, like ICC1 and ICC3, contain abundant quartz pebbles and carbonate-cemented sandstone and mudstone clasts that are interpreted to mark the end of the FSST and onset of ensuing LST sedimentation.

The succeeding MAJFS followed by TST are marked by a general decrease in siliciclastic proxy abundance, except for Si, in CCS and CCHS, illustrating an overall dilution in sediment input from the continent (relative to carbonate input). However, this trend is not observed in CCN where a 37 m-thick laterally accreting channel unit informally named Unit 21 crops out. Localized pebble conglomerate marks the contact between the aggradational channel element and the overlying three laterally accreting elements (Dumouchel, 2015). The top of Unit 21 corresponds to an MFS and the onset of another HST. This HST manifests differently across all three outcrops: A slide and debrite make up this unit in CCS (S2 of MTD 4), in CCN a channel unit (Unit 24) crops out above a debrite, and levee deposits of Unit 24 comprise the HST in CCHS. Unit 21 and 24 are truncated by S2 between CCS and CCN, however this contact is covered by the glacier.

Overlying S2 is D4, a mud-rich debrite with common quartz pebbles and carbonate clasts that marks a period of significant gravitational instability on the slope and falling RSL. A pebble-conglomerate horizon lies above the debrite, representing the FSST and onset of ICC5 deposition. Most of ICC5 lies above the sequence boundary that marks the base of the LST and comprises aggradational channel fills showing an increase in siliciclastic proxies suggestive of an overall increase in coarse-grained sediment supply. Maxima in the carbonate proxies are attributed to a single Ca-rich phosphate horizon (Ca-rich fluorapatite). The uppermost channel fill of ICC5 is laterally accreting and marks the transition to the TST.

The ensuing HST is characterized by a slide in CCS and CCHS; in CCN a general decrease in siliciclastic proxies is observed, with the exception of Zr that correspond to the deposition of several isolated channel fills. The HST is overlain by a pebble-conglomerate and carbonate clast-rich horizon interpreted to represent another major fall in RSL (FSST) that initiated deposition of aggradational channel fills at the base of ICC6. Finally, the top of the study area is interpreted to represent the TST, characterized by decreasing coarse-grained proxy abundance and increasing clay proxy abundance. In CCN, this TST is exhibits a peak in carbonate proxy abundance immediately following the MAJFS, suggesting that RSL rise initiated a short-lived increase in carbonate production on the shelf before drowning the carbonate factory.

6.3 Depositional Model

Litho- and chemostratigraphic data presented in this study have established a link between geochemistry and stacking of architectural elements, both controlled by changes in RSL (Table 6.1), from which the depositional history of slope channel complexes ICC1 to ICC6 in the Isaac Formation can be unravelled. This, therefore, provides the opportunity to create an idealized depositional model of leveed slope channel complexes in response to the combined effects of long- and short-term fluctuations in RSL (Figure 6.5).

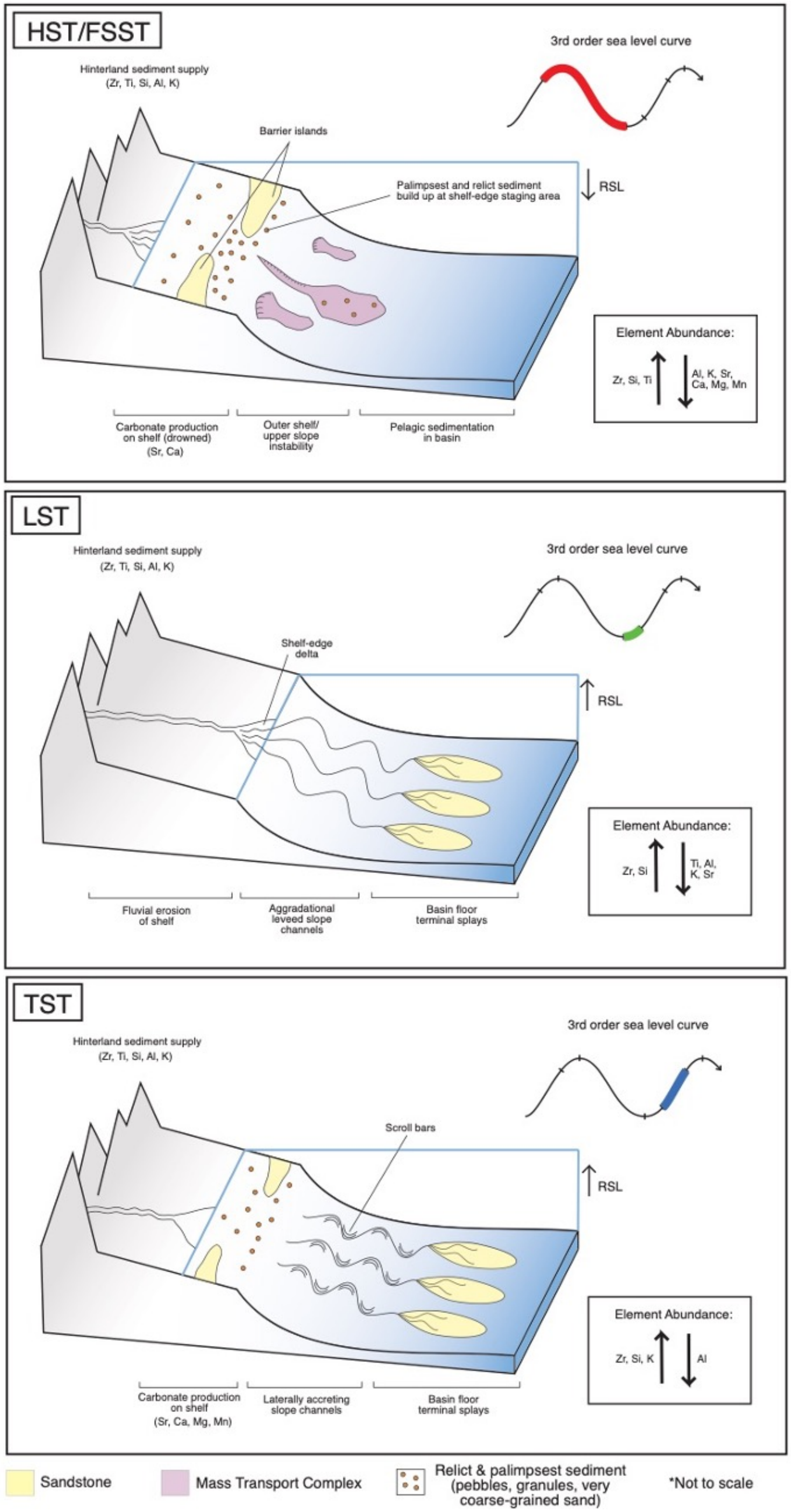
HST/FSST
3rd order sea level curve
Hinterland sediment supply (Zr, Ti, Si, Al, K)
Barrier islands
Palimpsest and relict sediment build up at shelf-edge staging area
RSL
Element Abundance:
Zr, Si, Ti
Al, K, Sr, Ca, Mg, Mn
Carbonate production on shelf (drowned) (Sr, Ca)
Outer shelf/ upper slope instability
Pelagic sedimentation in basin
LST
Hinterland sediment supply (Zr, Ti, Si, Al, K)
3rd order sea level curve
Shelf-edge delta
RSL
Element Abundance:
Zr, Si
Ti, Al, K, Sr
Fluvial erosion of shelf
Aggradational leveed slope channels
Basin floor terminal splays
TST
3rd order sea level curve
Hinterland sediment supply (Zr, Ti, Si, Al, K)
Scroll bars
RSL
Element Abundance:
Zr, Si, K
Al
Carbonate production on shelf (Sr, Ca, Mg, Mn)
Laterally accreting slope channels
Basin floor terminal splays
Sandstone
Mass Transport Complex
Relict & palimpsest sediment (pebbles, granules, very coarse-grained sand)
*Not to scale

Figure 6.5. Idealized depositional model illustrating dominant architectural elements deposited during a single RSL cycle. HST/FSST: Calciturbidite deposition during RSL highstand and subsequent drowning of the carbonate factory as RSL reaches a maximum. More commonly, the onset of RSL fall initiates a period of gravitationl instability on the outer shelf and/or upper slope, resulting in deposition of attached or detached MTDs (slides and debrites). Increase in Zr, Si, and Ti abundance as sediment becomes sourced directly from the hinterland and Al, K, Sr, Ca, Mg, Mn decrease in abundance. LST: Progradation of the shelf-edge delta delivers sediment directly from the hinterland to the basin and aggradational channel elements dominate. Coarse-grained (Zr, Ti, Si) and clay (Al, K) proxy abundance initially increase before decreasing as RSL rise increasingly inhibits sediment transport across the shelf and into the basin. TST: Laterally accreting channel elements sharply overlie aggradational elements of the previous LST; Anomalously coarse-grained, well-sorted sediment that accumulated in the shelf-edge staging area during short-term RSL falls (superimposed on long-term RSL rise) modifies the density structure of through-going turbidity currents, resulting in an increase in coarse-grained proxy abundance (Zr, Si). Carbonate proxy abundance initially increases before decreasing as rising RSL eventually shuts down the carbonate factory on the shelf.

During long-term Highstand and ensuing Falling Stage of RSL (HST/FSST) deep-marine slope deposition is dominated by calciturbidites, or more commonly, MTDs (up to 170 m thick). HST calciturbidite units indicate flooding of the continental shelf and activation of the carbonate factory. MTDs, on the other hand, indicate a period of major instability associated with RSL fall (FSST) that destabilizes the upper slope and/or outer shelf. In addition, the presence of quartz pebble conglomerates with abundant carbonate-cemented sandstone and mudstone and less common carbonate clasts, suggests periods of intense erosion of the shelf during RSL fall and remobilization of relict and palimpsest sediment previously sequestered at the shelf-edge following multiple episodes of short-term RSL fall superimposed on the long-term transgression. Geochemical characteristics of the HST/FSST include elevated carbonate proxy abundance (Sr, Ca) that sharply decrease upwards, whereas coarse-grained siliciclastic proxy abundance (Zr, Si) increases upward indicating the shutdown of the carbonate factory and concomitant rejuvenation of the hinterland sediment supply.

The ensuing LST is characterized by the presence of up to 110 m-thick aggradational channel elements (complexes), wherein sediment is delivered directly from the hinterland to the basin. The polydispersed makeup of the sediment supply causes flows to become density stratified, well-mixed, and inefficient, leading to deposition both within and outside of the channel. Geochemically, the LST typically exhibits an initial increase followed by decrease in siliciclastic proxy abundance (Zr, Ti, Si, Al, K) as RSL begins to rise beyond the SB. Carbonate proxy abundance (Sr, Ca) is generally low during the LST.

Aggradational channels are then sharply overlain by laterally accreting channel elements that mark the long-term TST. The progressive landward migration of the hinterland sediment supply, but more importantly, the gradual expansion of the shelf, results in coarse palimpsest and lesser relict sediment being moved to the shelf edge during short-term falls of RSL. The better sorted character of this coarse-sediment-enriched sediment supply causes flows to adopt a sharply bounded two-part density structure. This, then, causes flow to exhibit a secondary circulation pattern in channel bends that resembles that in sinuous fluvial systems, and ultimately, lateral accretion and deposition on the margin of the channel. Siliciclastic proxy abundance, specifically coarse-grained proxies (Zr and Si), increase whereas clay proxies (Al, K) decrease, reflecting the dominantly coarse-grained nature of laterally accreting channel elements (see section 4.2.3). Carbonate proxy abundance (Sr, Ca, Mg, Mn) initially increases and then gradually decreases towards the top of the TST, interpreted to reflect an initial period of carbonate production on the shelf (TST) followed by drowning of the carbonate platform (HST).

Table 6.1. Systems tracts and associated lithological and geochemical attributes.

SYSTEMS TRACT	LITHOLOGY	DIMENSIONS	INCREASING	DECREASING
HST/FSST	- Mass Transport elements - pebble conglomerate with carbonate-cemented sandstone and mudstone clasts	Up to 170 m thick	Zr, Ti, Si	Al, K, Sr, Ca, Mg, Mn

	- calciturbidites			
LST	- Aggradational channel elements - Grain size: granule conglomerate – clay; fills dominantly granule conglomerate – clay sandstone	Up to 110 m thick channel complexes, units and fills up to 62 m and 15 m, respectively	Zr, Si	Ti, Al, K, Sr
TST	- Laterally accreting channel elements - Grain size: very coarse – coarse sandstone, fine sandstone – clay	Up to 45 m thick complexes, units and fills up to 33 m and 15 m, respectively	Zr, Si, K	Al

6.4 Areas for Future Research

The current lack of geochronological constraints throughout the WSG is problematic when attempting to identify possible mechanisms for the unconformity at the base of ICC4B. Further research into deep-marine unconformities and detailed geochronological analyses at Castle Creek may assist in bridging this gap. Additional sampling for bulk geochemistry up to the second Isaac Carbonate (beyond ICC6) may elucidate further trends in long-term RSL changes that cannot be identified in this study. In addition, due to travel restraints at the time of this study (2020-2021 Covid pandemic) additional stratigraphic logs in the Hill Section may be useful in advancing the interpretations presented here.

References

Aalto, K.R. (1971). Glacial marine sedimentation and stratigraphy of the Toby Conglomerate (Upper Proterozoic), southeastern British Columbia, Northwestern Idaho and Northeastern Washington, *Canadian Journal of Earth Sciences, 8*: 753-787.

Abreu, V., Sullivan M., Pirmez C., Mohrig D., & Mutti E. (2003). Lateral accretion packages (LAPs); an important reservoir element in deep water sinuous channels. *Marine and Petroleum Geology, 20*, 631–648.

Aitken, J.D. (1969). Documentation of the sub-Cambrian unconformity, Rocky Mountains Main Ranges, Alberta. *Canadian Journal of Earth Sciences, 6*(2), 193-200

Allen, J.R.L. (1970). The sequence of sedimentary structures in turbidites: with special reference to dunes, *Scottish Journal of Geology, 6*, 146–161.

Armstrong-Altrin, J.S., Lee, Y.I., Verma, S.P., Ramasamy, S. (2004). Geochemistry of sandstone from the upper Miocene Kudankulam Formation, southern India: Implications for provenance, weathering, and tectonic setting, *Journal of Sedimentary Research, 74*(2), 285-297

Arnott, R.W.C. (2007). Stratal architecture and origin of lateral accretion deposits (LADs) and conterminous inner-bank levee deposits in a base-of-slope sinuous channel, lower Isaac Formation (Neoproterozoic), East-Central British Columbia, Canada, *Marine and Petroleum Geology, 24,* 515-528.

Arnott, R. W. C. (2010). Deep-marine sediments and sedimentary systems. In *Facies models 4*, 295-322. Geological Association of Canada, St. John's, Newfoundland and Labrador.

Arnott, R.W.C. (2012) Turbidites, and the case of the missing dunes, *Journal of Sedimentary Research, 82*, 379-384.

Arnott, R. W. C., and Hand, B. M. (1989). Bedforms, primary structures and grain fabric in the presence of suspended sediment rain. *Journal of Sedimentary Research, 59*(6), 1062-1069.

Arnott, R.W.C., Wallace, K., and Laurin, J., Shipp, R.C., Weimer, P., Posamentier, H.W. (2011) Stratal architecture and temporal evolution of a passive margin mass-transport deposit, Neoproterozoic Isaac Formation, Cariboo Mountains, British Columbia, Canada, *Mass-Transport Deposits in Deepwater Settings: SEPM, Special Publication, 96,* 221-234.

Arnott, R. W. C., Tilston, M., Fraino, P., Navarro, L., Dumouchel, G., & Miklovich., N. (2021) Laterally-accreting sinuous channels – the Goldilocks of deep-water slope systems: *Journal of Sedimentary Research*, *91*, p. 451-463.

Bergen, A. (2017). Vertical and lateral facies architectures of slope channels and genetically related levee deposits, Isaac Formation, Neoproterozoic Windermere Supergroup, Cariboo Mountains, B.C. M.Sc. thesis, University of Ottawa, Ottawa, ON.

Bergen, A.L., Cunningham, C.M., Terlaky, V., Arnott, R.W.C. (accepted) Influence of channelized-flow density structure on the stratal architecture of deep-marine levee sedimentation: *Journal of Sedimentary Geology*.

Bennett, S.J., Atkinson, J.F., (2013). Turbulence suppression by suspended sediment within a geophysical flow, *Environmental Fluid Mechanics, 14,* 771-794

Best, J. (1992). On the entrainment of sediment and initiation of bed defects – Insights from recent developments within turbulent boundary-layer research. *Sedimentology, 39,* 797-811

Billington, T. (2019). Sedimentologic and Petrographic Evidence of Flow Confinement in a Passive Continental Margin Slope Channel Complex, Isaac Formation, Windermere

Supergroup, British Columbia, Canada. M.Sc. thesis, University of Ottawa, Ottawa, ON.

Birman, V.K., Meiberg, E., Kneller, B. (2009). The shaoe of submarine levees: exponential or power law?. *Journal of Fluid Mechanics, 619,* 367-376.

Bond, G. C., and Kominz, M. A. (1984). Construction of tectonic subsidence curves for the early Paleozoic miogeocline, southern Canadian Rocky Mountains — implications for subsidence mechanisms, age of breakup and crustal thinning, *Geological Society of America Bulletin, 95*, 155–173.

Bouma, A.H., (1962). Sedimentology of some Flysh Deposits. A graphic approach to facies interpretation. Elsevier, Amsterdam, p.168.

Campbell, R. B. (1973). Structural cross-section and tectonic model of the southeastern Canadian Cordillera: *Canadian Journal of Earth Sciences, 10,* 1607-1620.

Cantero, M. I., Cantelli, A., Pirmez, C., Balachandar, S., Mohrig, D., Hickson, T. A., Yeh, T., Naruse, H., and Parker, G., 2012, Emplacement of massive turbidites linked to extinction of turbulence in turbidity currents: *Nature Geoscience, 5,* 42-45.

Cantero, M. I., Shringarpure, M., Balachandar, S. (2012). Towards a universal criteria for turbulence suppression in dilute turbidity currents with non-cohesive sediments, *Geophysical Research Letters, 39,* L14603.

Catuneanu, O. (2006). Principles of sequence stratigraphy: Amsterdam, Elsevier, 375

Catuneanu, O., Abreu, V., Bhattacharya, J. P., Blum, M. D., Dalrymple, R. W., Eriksson, P. G., and Giles, K. A. (2009). Towards the standardization of sequence stratigraphy: *Earth-Science Reviews, 92*(1-2), 1-33.

Chapin, C. E., & Glazner, A. F. (1983). Widespread K2O metasomatism of Cenozoic volcanic and sedimentary rocks in the southwestern United States. *Geological Society of*

America Abstracts with Programs, 15, p. 282.

Chapin, C.E., Lindley, J.I. (1986). Potassium metasomatism of igneous and sedimentary rocks in detachment terranes and other sedimentary basins: economic implications, *Arizona Geological Society Digest XVI*, 118–126

Chen, H.-F., Yeh, P. Y., Song, S. R., Hsu, S. C., Yang, T. N., Wang, Y., Chi, Z., Lee, T. Q., Chen, M. T., Cheng, C. L., Zou, J., Chang, Y. P. (2013). The Ti/Al molar ratio as a new proxy for tracing sediment transportation processes and its application in aeolian events and sea level change in East Asia, *Journal of Asian Earth Sciences, 73,* 31–38.

Clark, J. D., and Pickering, K. T. (1996). Architectural elements and growth patterns of submarine channels: application to hydrocarbon exploration: *AAPG Bulletin, 80*, 194-220.

Cochrane, D. J., Navarro, L., and Arnott, R.W.C. (2019) Sedimentological and geochemical evolution of an Ediacaran mixed carbonate-siliciclastic continental slope system, Windermere Supergroup, southern Canadian Cordillera, British Columbia, Canada: *Precambrian Research*, *327*, 47-67.

Colpron, M., Logan, J.M., and Mortensen, J.K. (2002). U-Pb zircon age constraint for late Neoproterozoic rifting and initiation of the lower Paleozoic passive margin of western

Cox, R., Lowe, D. R., Cullers, R. L. (1995). The influence of sediment recycling and basement composition on evolution of mudrock chemistry in the southwestern United States, *Geochimica et Cosmochimica Acta, 59*(14), 2919-2940.

Davis, L. (2011). Architecture of deep-marine interchannel deposits: Isaac Formation, Windermere Supergroup (Neoproterozoic), southern Canadian Cordillera, M.Sc. thesis, University of Ottawa, Ottawa, ON.

Dumouchel, I.G. (2012). Effects of relative sea-level change on the stratigraphic architecture of a passive margin deep-marine channel fill complex, Windermere Supergroup, British Columbia, Canada, B.Sc. thesis, University of Ottawa, Ottawa, ON.

Dumouchel, I.G. (2015). Stratigraphic architecture and depositional history of laterally-accreted channel fills in the Lower Isaac Formation, Windermere Supergroup, British Columbia, Canada, M.Sc. thesis, University of Ottawa, Ottawa, ON.

Ennis, D. J., Dunbar, N. W., Campbell, A. R., Chapin, C. E. (2000). The effects of K-metasomatism on the mineralogy and geochemistry of silicic ignimbrites near Socorro, New Mexico, *Chemical Geology, 167,* 285-312

Evans, K.V., Aleinikoff, J.N., Obradovich, J.D., and Fanning, C.M. (2000.) SHRIMP U-Pb geochronology of volcanic rocks, Belt Supergroup, western Montana: evidence for rapid deposition of sedimentary strata, Canadian Journal of Earth Sciences, 37, 1287-1300.

Macdonald, F. A., Schmitz, M. D., Strauss, J. V., Halverson, G. P., Gibson, T. M., Eyster, A., Cox, G., Mamrol, P., Crowley, J. L. (2018). *Precambrian Research, 319,* 114-143.

Fedo, C. M., Nesbitt, H. W., Young, G. M. (1995). Unraveling the effects of potassium metasomatism in sedimentary rocks and paleosols, with implications for paleoweathering conditions and provenance, *Geology, 23*(10), 921-924.

Fraino, P. (2020). Spatial and Temporal Stratal Evolution of an ancient deep-marine channel-levee complex, Neoproterozoic Isaac Formation, Windermere Supergroup, British Columbia, Canada, M.Sc. thesis, University of Ottawa, Ottawa, ON.

Fraino, P., Arnott, R.W.C., Navarro, L., (accepted). The influence of sediment supply on the stratigraphic evolution of an ancient passive margin deep-marine slope channel complex, Windermere Supergroup, British Columbia, Canada. *Journal of Sedimentary*

Research.

Gammon, P. R., Arnott, R. W. C., and Ross, G. M. (2007). Architectural relationships between channels, levees, and debris flows: Isaac channel 6, Castle Creek South, lower Isaac Formation, Windermere Supergroup, British Columbia, Canada, *In* Atlas of Deep-water Outcrops: AAPG Studies in Geology 56. *Edited* by Nilsen, T.H., Shew, R.D., Steffens, G. S., and Studlick, J. R. J., CD-ROM, 4 p.

Glazner, A.F. (1985). Stratigraphy, structure, and potassic alteration of Miocene volcanic rocks in the Sleeping Beauty area, central Mojave Desert, California, *Geological Society of America Bulletin, 100,* 424-435

Hadlari, T., Arnott., R.W.C., Matthews, W.A., Poulton, T.P., Root, K., and Madronich, L.I., (in review). Provenance of the incipient passive margin of NW Laurentia (Neoproterozoic): detrital zircon from continental slope and basin floor deposits of the Windermere Supergroup, southern Canadian Cordillera: *Lithosphere*.

Haflidason, H., Sejrup, H. P., Nygard, A., Mienert, J., Bryn, P., Lien, R., Forsberg, C. F., Berg, K., Masson, D. (2004). The Storegga Slide: architecture, geometry, and slide development, *Marine Geology, 213,* 201-234.

Harper, B. B., Puga-Bernabeu, A., Droxler, A. W., Webster, J. M., Gischler, E., Twiari, M., Lando-Insua, T., Thomas, A. L., Morgan, S., Jovane, L., Rohl, U. (2015). Mixed carbonate-siliciclastic sedimentation along the Great Barrier Reef upper slope: a challenge to the reciprocal sedimentation model, *Journal of Sedimentary Research, 85,* 1019-1036.

Harnois, L. (1988). The CIW index: a new chemical index of weathering. *Sedimentary geology*, *55*(3), 319-322.

Hodgson, D. M., Di Celma, C. N., Brunt, R. L., Flint, S. S. (2011). Submarine slope degradation and aggradation and the stratigraphic evolution of channel-levee systems, *Journal of the Geological Society, London, 168,* 625-628.

Huyer, G. (2016). Architecture and stratigraphy of a Neoproterozoic deep-marine slope channel-complex set, Windermere Supergroup, Castle Creek, B.C., B.Sc. thesis, University of Ottawa, Ottawa, ON.

Jobe, Z. R., Howes, N. C., and Auchter, N. C. (2016). Comparing submarine and fluvial channel kinematics: implications for stratigraphic architecture: The Geological Society of America, 44(11), p.931-934.

Jorry, S. J., Droxler, A. W., Francis, J. M. (2010). Deppwater carbonate deposition in response to re-flooding of carbonate bank and atoll-tops at glacial terminations, *Quaternary Science Reviews, 29,* 2010-2026.

Khan, Z. A., and Arnott, R. W. C. (2011). Stratal attributes and evolution of asymmetric inner- and outer-bend levee deposits associated with an ancient deep-water channel-levee complex within the Isaac Formation, southern Canada, *Marine and Petroleum Geology, 28*, 824-842.

Khan, Z.A. (2012) Origin and architecture of deep-water levee deposits: Insight from the ancient rock record and experiments, Ph.D. thesis, University of Ottawa, Ottawa, ON.

Keeley, J. A., Link, P. K., Fanning, C. M., & Schmitz, M. D. (2013). Pre-to synglacial rift-related volcanism in the Neoproterozoic (Cryogenian) Pocatello Formation, SE Idaho: New SHRIMP and CA-ID-TIMS constraints. *Lithosphere*, *5*(1), 128-150.

Kendall, B.S., Creaser, R.A., Ross, G.M., and Selby, D. (2004). Constraints on the timing of Marinoan "Snowball Earth" glaciation by 187Re-187Os dating of a Neoproterozoic, post-glacial black shale in Western Canada, *Earth and Planetary Science Letters, 222*: 729-740.

Kuenen, P. H., & Migliorini, C. I. (1950) Turbidity currents as a cause of graded bedding. *The Journal of Geology*, 58(2), 91-127.

Kuenen, P. H. (1957). Sole markings of graded graywacke beds. *The Journal of Geology*, *65*(3), 231-258.

Kneller, B.C. and Buckee, C., (2000), The structure and fluid mechanics of turbidity currents: a review of some recent studies and their geological implications. *Sedimentology, 47*(1), 62-94.

Kneller, B. C. (2003) The influence of flow parameters on turbidite channel slope Architecture. *Marine and Petroleum Geology, 20*, p.901–910.

LaGrange, M.T., Konhauser, K.O., Catuneanu, O., Harris, B.S., Playter, T.L., and Gingras, M.K. (2020). Sequence stratigraphy in organic-rich marine mudstone successions using chemostratigraphic datasets: *Earth Science Reviews, 203*, 103-137.

Laurin, J. (2005). Depositional history and sequence stratigraphic context of a Neoproterozoic mass transport deposit, Isaac Formation, east-central B.C., B.Sc. thesis, University of Ottawa, Ottawa, ON.

Le Roux, J. P. (2003). Can dispersive pressure cause inverse grading in grain flows? – Discussion, *Journal of Sedimentary Research, 73*(2), 333-334.

Li, Z.X., Evans, D.A.D., and Halverson, G.P. (2013). Neoproterozoic glaciations in a revised global palaeogeography from the breakup of Rodinia to the assembly of Gondwanaland, *Sedimentary Geology, 294*: 219-232.

Liu, H. K. (1957). Mechanics of sediment-ripple formation, *American Society of Civil Engineers,* *83*(HY2).

Lowe, D.R. (1982). Sediment gravity flows: II. Depositional models with special reference to the deposits of high-density turbidity currents: *Journal of Sedimentary Petrology, 52*, p.279-297.

Lowe, D. R. (1988). Suspended-load fallout rate as an independent variable in the analysis of current structures: *Sedimentology, 35*, p.765-776.

Lund, K., Aleinikoff, J.N., Evans, K.V., and Fanning C.M. (2003). SHRIMP U-Pb geochronology of Neoproterozoic Windermere Supergroup, central Idaho: Implications for rifting of western Laurentia and synchroneity of Sturtian glacial deposits, Geological Society of America Bulletin, 115: 349-372. Hoffman, P.F. 1991. Did the breakout of Laurentia turn Godwanaland inside-out?, Science, 525: 1409-1412.

Macauley, R. V., and Hubbard, S. M. (2012). Slope channel sedimentary processes and stratigraphic stacking, Cretaceous Tres Pasos Formation slope system, Chilean Patagonia: *Marine and Petroleum Geology, 41*, p.146-162.

Marion, C. (2005) Architecture and sedimentology of a channel and slide complex in the Neoproterozoic Isaac Formation, British Columbia: B.Sc. thesis, University of Ottawa, ON.

Mayall, M., Jones, E., & Casey, M. (2006). Turbidite channel reservoirs – Key elements in facies prediction and effective development. *Marine and Petroleum Geology, 23*(8), 821-841

Maynard, J. B. (1992). Chemistry of modern soils as a guide to interpreting Precambrian paleosols. *The Journal of Geology*, *100*(3), 279-289.

Mcdonough, M. R., and Parrish, R., R. (1991). Proterozoic gneisses of the Malton Complex, near Valemount, British Columbia: U-Pb ages and Nd isotopic signatures, *Canadian Journal* *of Earth Science, 28,* 1202-1216.

McHargue, T., Pyrcz, M. J., Sullivan, M. D., Clark, J. D., Fildani, A., Romans, B. W., Covault, J.A., Levy, M., Posamentier, H.W., and Drinkwater, N. J. (2011). Architecture of turbidite channel systems on the continental slope: patterns and predictions: *Marine and Petroleum Geology, 28*, 728-743.

Middleton, G. V. (1960). Chemical composition of sandstones, *Geological Scoiety of America Bulletin, v. 71,* p.1011-1026.

Middleton, G. V. (1966a). Experiments on density and turbidity currents: I. Motion of the head. *Canadian Journal of Earth Sciences*, *3*(4), 523-546.

Middleton, G. V. (1966b). Experiments on density and turbidity currents: II. Uniform flow of density currents. *Canadian Journal of Earth Sciences*, *3*(5), 627-637.

Middleton, G. V. (1967). Experiments on density and turbidity currents: III. Deposition of sediment. *Canadian Journal of Earth Sciences*, *4*(3), 475-505.

Middleton, G.V. and Hampton, M.A. (1973). Sediment Gravity Flows: mechanics of flow and deposition, in Middletong, G.V and A.H Bouma, eds., *Turbidites and Deep Water Sedimentation. Short Course Notes*, No 1, SEPM (Pacific Section), Los Angeles, p. 1-38.

Middleton, G. V., and Hampton, M. A. (1976). Subaqueous sediment transport and deposition by sediment gravity flows *In* Marine sediment transport and environment management *edited by* Stanley, D. J. and Swift, D. J. P., 197-218.

Miklovich, N. (2018). Stratigraphic Architecture and Depositional Evolution of Laterally-Accreting Deep-Marine Channel Deposits in the Isaac Formation, Windermere Supergroup, Canada, B.Sc. thesis, University of Ottawa, Ottawa, ON.

Milczarek, G. (2018). Chemostratigraphic analysis of mudrocks and its implication on provenance and sequence stratigraphy in the Isaac Formation, Windermere turbidite system, Castle Creek, B.C., Canada, B.Sc. thesis, University of Ottawa, Ottawa, ON.

Monger, J. W. H., & Price, R. A. (1979). Geodynamic evolution of the Canadian Cordillera—progress and problems. *Canadian Journal of Earth Sciences*, *16*(3), 770-791.

Montero-Serrano, J. C., Bout-Roumazeilles, V., Tribovillard, N., Sionneau, T., Riboulleu, A., Bory, A., Flower, B. (2009). Sedimentary evidence of deglacial megafloods in the northern Gulf of Mexico (Pigmy Basin), *Quaternary Science Reviews, 28,* 3333-3347.

Moscardelli, L., Wood, L., Mann, P. (2006). Mass-transport complexes and associated process in the offshore area of Trinidad and Venezuela, *AAPG Bulletin, 90*(7), 1059-1088.

Moscardelli, L., Wood, L. (2008). New classification system for mass transport complexes in offshore Trinidad, *Basin Research, 90,* 73-98.

Moscardelli, L., Wood, L. (2016). Morphometry of mass-transport deposits as a predictive tool, *Geological Society of America Bulletin, 128*(1-2), 47-80.

Mulder, T., and Alexander, J. (2001). The physical character of subaqueous sedimentary density flows and their deposits: *Sedimentology, 48*, 269-299.

Murphy, D.C., (1987). Suprastructure/infrastructure transition, east-central Cariboo Mountains, British Columbia; geometry, kinematics and tectonic implications, *Journal of Structural Geology, 9*: 13-29.

Mussa-Caleca, M. (2008). Architecture and depositional history of a Neoproterozoic deep-water slope channel complex in a passive margin setting: Isaac Formation, Windermere Supergroup, southern Canadian Cordillera, M.Sc. thesis, University of Ottawa, Ottawa, ON.

Mutti, E., & Normark, W. R. (1987). Comparing examples of modern and ancient turbidite systems: problems and concepts, in J. R. Leggett, and G. G. Zuffa, eds., Marine Clastic Sedimentology: Concepts and Case Studies: London, Graham and Trotman, p.1–37.

Mutti, E., & Normark, W. R. (1991) An integrated approach to the study of turbidite systems, in P. Weimer, and M. H. Link, eds., Seismic facies and sedimentary processes of submarine fans and turbidite systems: New York, Springer-Verlag, 75–106.

Mutti, E., Ricci Lucchi, F. (1972). Le torbidite dell'Apennino Settentrionale: introduzione all'analisi di facies: Societa Geologica Italiana, *Memoir 11,* 161-199

Mutti, E., Ricci Lucchi, F. (1975). Turbidite facies and facies associations *In* Examples of turbidite facies and facies associations from selected formation in the Northern Appenines: Field trip guide book A-11, *IX International Congress Sedimentology, Nice,* 21-36

Mutti, E., Ricci Lucchi, F. (1978). Turbidites of the northern Apennines: introduction to facies analysis, *International Geology Review, 20*(2), 125-166.

Nathan, S. (1976). Geochemistry of the Greenland Group (Early Ordovician), New Zealand, *New Zealand Journal of Geology and Geophysics, 19*(5), 683-706.

Navarro, L. (2006). Depositional architecture and evolution of deep-water base-of-slope and slope channel complexes in a passive margin setting: Isaac Formation, Windermere Supergroup (Neoproterozoic) southern Canadian Cordillera, M.Sc. thesis, University of Ottawa, Ottawa, ON.

Navarro, L., Z. Khan, and R. W. C. Arnott, (2007). Depositional architecture and evolution of a deep-marine channel-levee complex: Isaac Formation (Windermere Supergroup), Southern Canadian Cordillera., in T. H. Nilsen, R.D. Shew, G. S. Steffens, and J. R. J. Studlik, eds., Atlas of Deep-water Outcrops., v. CD-ROM: Tulsa, AAPG Studies in

Geology 56, CD- ROM, p.22.

Navarro, L., Arnott, R. W. C. (2019). Stratal architecture and evolution of a slope mass-transport complex, Isaac Formation, Neoproterozoic Windermere Supergroup, southern Canadian Cordillera, British Columbia, Canada, *In* Lintern, D. G., Mosher, D. C., Moscardelli, L. G., Borrowsky, P. T., Campbell, C., Chaytor, J. D., Clague, J. J., Georgiopoulou, A., Lajeunesse, P., Normandeau, A., Piper, D. J. W., Schierwath, M., Stacey, C., Turmel, D. (eds) 2019. *Subaqueous Mass Movements. Geological Society, London, Special Publications, 477,* 265–276.

Nesbitt, H. W., Young, G. M. (1982). Early Proterozoic climates and plate motions inferred from major element chemistry of lutites, *Nature, 299,* 715-717.

Nyhuis, C. J., Riley, D., Kalasinska, A. (2016). Then section petrography and Chemostratigraphy: Integrated evaluation of an upper Mississippian mudstone dominated succession from the southern Netherlands, *Netherlands Journal of Geosciences, 95*(1), 3-22.

Peakall, J., McCaffrey, B., and Kneller, B. (2000). A process model for the evolution, morphology, and architecture of sinuous submarine channels: *Journal of Sedimentary Research, 70*, p. 434-448.

Pearce, T. J., Besly, B. M., Wray, D. S., Wright, D. K. (1999). Chemostratigraphy: a method to improve interwell correlation in barren sequences – a case study using onshore Duckmantian/Stephanian sequences (West Midlands, U.K.), *Sedimentary Geology, 124,* 197-220.

Pearce, T. J., Wray, D., Ratcliffe, K., Wright, D. K., Moscariello, A. (2005). Chemostratigraphy of the Upper Carboniferous Schooner Formation, southern North Sea, *In* Carboniferous hydrocarbon geology the southern North Sea and surrounding onshore areas, *Edited by* Collinson, J. D., Evans, D. J., Holliday, D. W., Jones, N. S., v. 7, p.147-164.

Pickering, K. T., Corregidor, J. (2005). Mass-transport complexes (MTCs) and tectonic control on basin-floor submarine fans, middle Eocene, south Spanish Pyrenees, *Journal of Sedimentary Research, 75,* 761-783.

Piper, D. J., & Normark, W. R. (1983). Turbidite depositional patterns and flow characteristics, Navy submarine fan, California Borderland. *Sedimentology*, *30*(5), 681-694.

Posamentier, H. W., and Kolla, V. (2003). Seismic geomorphology and stratigraphy of depositional elements in deep-water settings, *Journal of Sedimentary Research, 73*, p. 367-388.

Posamentier, H. W., and Martinesen, I. J. (2010). The character and genesis of submarine mass-transport deposits: Insights from outcrop and 3D seismic data, *Mass-Transport Deposits in Deepwater Settings SEPM Special Publication 95.*

Price, R.A. (2000). The southern Canadian Rockies: Evolution of a foreland thrust and fold belt. GeoCanada 2000.

Puga-Bernabeu, A., Webster, J. M., Beaman, R. J., Guillbaud, V. (2011). Morphology and controls on the evolution of a mixed carbonate-siliciclastic submarine canyon system, Great Barrier Reef margin, north-eastern Australia. *Marine Geology, 289,* 100-116.

Ramkumar, M., Nagarajan, R., Santosh, M. (in press). Advances in sediment geochemistry and chemostratigraphy for reservoir characterization, *Energy Geoscience.*

Ratcliffe, K. T., Morton, A. C., Ritcey, D. H., Evenchick, C. A. (2007). Whole-rock geochemistry and heavy mineral analysis as petroleum exploration tools in the Bowser and Sustut basins, British Columbia, Canada, *Bulletin of Canadian Petroleum Geology,* *55*(4), 320-336.

Reid, L. F., Simony, P. S., & Ross, G. M. (2002) Dextral strike-slip faulting in the Cariboo Mountains, British Columbia: a natural example of wrench tectonics in relation to Cordilleran tectonics. *Canadian Journal of Earth Sciences*, *39*(6), 953-970.

Reid, L. F. (2003). Stratigraphy, structure, petrology, geo- chronology and geochemistry of the Hobson Lake area (Cariboo Mountains, British Columbia) in relation to the tectonic evolution of the southern Canadian Cor-dillera, Ph.D. thesis, University of Calgary, Calgary, Alberta, Canada, 221 p.

Roser, B.P. and Korsch, R.J. (1986) Determination of Tectonic Setting of Sandstone-Mudstone Suites Using SiO2 Content and K2O/Na2O Ratio. *The Journal of Geology, 94*, 635-650.

Ross, G.M., and Bowring, S.A. (1990). Detrital zircon geochronology of the Windermere Supergroup and the tectonic assembly of the southern Canadian Cordillera: *Journal of Geology, 98*, p. 879-893

Ross, G.M. (1991). Tectonic setting of the Windermere Supergroup revisited: *Geology, 19*, p. 1125-1128.

Ross, G.M., and Parrish, R.R. (1991). Detrital zircon geochronology of metasedimentary rocks in the southern Omineca Belt, Canadian Cordillera: *Canadian Journal of Earth Sciences, 28*, 1254-1270

Ross, G.M., Bloch, J.D., and Krouse, H.R. (1995). Neoproterozoic strata of the southern Canadian Cordillera and the isotopic evolution of seawater sulfate: *Precambrian Research, 73*, 71-99.

Ross, G.M., and Arnott, R.W.C. (2007). Regional Geology of the Windermere Supergroup, Southern Canadian Cordillera and Stratigraphic Setting of the Castle Creek Study Area, Canada. *In* Atlas of deep-water outcrops, AAPG Studies in Geology 56. *Edited by* T. H. Nilsen, R. D. Shew, G. S. Steffens, and J. R. J. Studlick, CD-ROM, 16 p.

Sano, J. L., Ratcliffe, K., Spain, D. R. (2013). Chemostratigraphy of the Haynesville Shale *In* Geology of the Haynesville Gas Shale in East Texas and West Louisiana, *edited by* Hammes, U. and Gale, J., *AAPG Memoir 105*, 137-154.

Schwarz, E., and Arnott, R.W.C. (2007a). Anatomy and evolution of a slope channel-complex set (Neoproterozoic Isaac Formation, Windermere Supergroup, southern Canadian Cordillera): implications for reservoir characterization, *Journal of Sedimentary Research, 77*, 89-109.

Schwarz, E., and Arnott, R.W.C. (2007b). Outcrop characterization of a passive- margin channel- complex set: Isaac Channel 5, Neoproterozoic Isaac Formation, British Columbia, Canada. *In* Atlas of deep-water outcrops: AAPG Studies in Geology 56. *Edited by* T. H. Nilsen, R. D. Shew, G. S. Steffens, and J. R. J. Studlick, CD-ROM, 15 p.

Shanmugam, G. (2006). Deep-water processes and facies models: Implications for sandstone petroleum reservoirs. Elsevier, New York, U.SA.

Sinha, S., Islam, R., Ghosh, S. K., Kumar, R., Sangode, S. J. (2007). Geochemistry of Neogene Siwalik mudstone along Punjab re-enrant, India: Implications for source-area weathering, provenance and tectonic setting, *Current Science, 92*(8), 1103-1113.

Smith, M.D. (2009). Stratigraphic and geochemical evolution of the Old Fort Point Fm., southern Canadian Cordillera: The deep-marine perspective of Ediacaran post-glacial environmental change, Ph.D. thesis, University of Ottawa, Ottawa, ON.

Smith, M. D. S., Arnoud, E., Arnott, R. W. C., Ross, G. M. (2011). The record of Neoproterozoic glaciation in the Windermere Supergoup, southern Canadian Cordillera, *In* Arnoud, E., Halverson, G. P. and Shields-Zhou, G. (eds). The Geological Record of Neoproterozoic Glaciations. *Geological Society of London, Memoirs 36*, 413-423.

Smith, M.D., Arnott, R.W.C., and Ross, G.M. (2014). Physical and geochemical controls on sedimentation along an ancient continental margin: The deep-marine Old Fort Point Formation (Ediacaran), southern Canadian Cordillera, *Bulletin of Canadian Petroleum Geology, 62*: 14-36.

Sohn, Y. K. (1997). On traction-carpet sedimentation, *Journal of Sedimentary Research, 67*(3), 502-509.

Stow, D. A., and Bowen, A. J. (1980). A physical model for the transport and sorting of fine-grained sediment by turbidity currents, *Sedimentology, 27,* 31-46.

Stow, D. A., & Shanmugam, G. (1980). Sequence of structures in fine-grained turbidites: comparison of recent deep-sea and ancient flysch sediments. *Sedimentary Geology*, *25*(1-2), 23-42.

Sumner, E. J., Amy, L. A., & Talling, P. J. (2008) Deposit structure and processes of sand depositing from decelerating sediment suspensions. *Journal of Sedimentary Research*, *78*, 529-547.

Sylvester, Z., Pirmez, C., and Cantelli, A. (2011). A model of submarine channel-levee evolution based on channel trajectories: implications for stratigraphic architecture, *Marine and Petroleum Geology, 28*, 716-727.

Talling, P. J., D. G. Masson, E. J. Sumnet, and G. Malgesini, (2012). Subaqueous sediment density flows: Depositional processes and deposit types*: Sedimentology, 59*, 1937-2003.

Tao, H., Sun, S., Wang, Q., Yang, X., Jiang, L. (2014). Petrography and geochemistry of lower carboniferous greywacke and mudstone in Northeast Junggar, China: Implications for provenance, source weathering, and tectonic setting, *Journal of Asian Earth Sciences, 87,* 11-25.

Terlaky, V. (2014). Sedimentology, stratigraphy, architecture and origin of deep-water, basin-floor deposits: Middle and upper Kaza Group, Windermere Supergroup, B.C., Canada, Ph.D. thesis, University of Ottawa, Ottawa, ON.

Terlaky, V., Rochealeau, J., and Arnott, R.W.C. (2016). Stratal composition and stratigraphic organization of stratal elements in an ancient deep-marine basin-floor succession, Neoproterozoic Windermere Supergroup, British Columbia, Canada, *Sedimentology, 63*, 136-175.

Tilston, M., Arnott, R.W.C., Rennie, C.D., and Long, B. (2015). The influence of grain size on the velocity and sediment concentration profiles and depositional record of turbidity currents, *Geology, 43*: 839-842.

Tripsanas, E. K., Karageorgis, A. P., Panagiotopoulos, I. O., Koutsopoulou, E., Kanellopoulos, T. D., Bryant, W., Slowey, N. C. (2013). Paleoenvironmental and peloclimatic implcations of enhanced Holocene discharge from the Mississippi River based on the sedimentology and geochemistry of a deep core (JPC-26) from the Gulf of Mexico, *Palaios, 28,* 623-636.

Turner, B. W., Tréanton, J. A., & Slatt, R. M. (2016). The use of chemostratigraphy to refine ambiguous sequence stratigraphic correlations in marine mudrocks. An example from the Woodford Shale, Oklahoma, USA. *Journal of the Geological Society*, *173*(5), 854–868.

Venditti, J.G., Church, M., and Bennett, S.J. (2005). Bed form initiation from a flat sand bed, *Journal of Geophysical Research, 110*: F01009, 1-19.

Venditti, J.G., Church, M., and Bennett, S.J. (2006). On interfacial instability as a cause of transverse subcritical bed forms, *Water Resources Research, 42*: W07423.

Van de Lageweg, W. I., van Dijk, W. M., Baar, A. W., Rutten, J., & Kleinhans, M. G. (2014). Bank pull or bar push: What drives scroll-bar formation in meandering rivers?. *Geology, 42*(4), 319-322

Vrolijk, P. J., and Southard, J. B. (1997). Experiments on rapid deposition of sand from high-velocity flows, *Geoscience Canada, 24*(1), 45-54.

Williams, P. B., & Kemp, P. H. (1971) Initiation of ripples on flat sediment beds. *Journal of the Hydraulics Division*, 97(4), 502-522.

Walker, R.G. (1965). The origin and significance of the internal sedimentary structures of turbidites. *Yorkshire Geological Society, Proceedings, 35*, p. 1–29.

Wynn, R.B., Cronin, B.T., and Peakall, J. (2007). Sinuous deep-water channels: Genesis, geometry, architecture, *Marine and Petroleum Geology, 24*, p.341-387.

Zaid, S. M. (2016). Geochemistry of shales from the Upper Miocene Samh Formation, north Marsa Alam, Red Sea, Egypt: implications for source area weathering, provenance, and tectonic setting. *Arabian Journal of Geosciences*, *9*(12), 1–15.

Appendix

Table A.1. Major element abundances in mass percent.

		LOI (input)	Na2O	MgO	Al2O3	SiO2	P2O5	K2O	CaO	TiO2	MnO	Fe2O3	S
Sample #	Height (m)	mass%	mass%	mass%	mass%	mass%	mass%	mass%	mass%	mass%	mass%	mass%	mass%
HSTOC_630	630	4.097	0.834	2.799	19.691	58.713	0.146	4.786	0.000	0.900	0.053	7.873	0.047
HSTOC_610	610	4.203	0.872	2.658	21.736	56.123	0.363	5.509	0.217	0.991	0.041	7.216	0.000
HSTOC_600	600	4.536	0.778	2.565	24.859	51.906	0.365	6.568	0.208	1.095	0.021	7.018	0.000
HSTOC_590	590	4.485	0.840	1.876	20.904	57.380	0.088	5.576	0.000	1.162	0.023	7.479	0.093
HSTOC_580	580	3.810	0.877	2.113	19.782	61.423	0.173	5.181	0.000	1.005	0.017	5.542	0.019
HSTOC_560	560	4.229	0.891	2.706	20.669	57.549	0.132	4.971	0.000	0.935	0.031	7.804	0.027
HSTOC_550	550	5.012	0.278	2.147	28.207	49.368	0.102	8.064	0.000	1.374	0.013	5.280	0.070
HSTOC_540	540	4.165	0.894	2.597	18.468	60.658	0.125	4.362	0.132	0.859	0.070	7.392	0.218
HSTOC_530	530	4.679	0.762	3.155	17.939	59.203	0.124	3.932	0.073	0.737	0.047	9.095	0.195
HSTOC_520	520	18.797	0.204	6.603	13.818	31.331	1.139	3.870	13.232	0.288	0.396	9.607	0.615
HSTOC_510	510	4.007	1.094	2.484	20.388	60.074	0.081	4.900	0.000	0.780	0.014	6.045	0.079
HSTOC_500	500	4.356	1.010	2.068	18.982	61.327	0.095	4.942	1.045	0.737	0.018	5.195	0.164
HSTOC_490	490	3.866	1.178	2.073	19.591	60.749	0.115	4.735	0.000	0.893	0.016	6.581	0.136
HSTOC_470	470	4.062	0.959	2.354	22.483	56.279	0.516	5.633	0.398	0.995	0.016	6.232	0.000
HSTOC_451	451	3.933	1.068	2.788	20.004	59.860	0.102	4.585	0.000	0.847	0.031	6.708	0.014
HSTOC_450	450	4.567	0.882	2.176	23.672	55.453	0.124	6.351	0.000	0.976	0.012	5.418	0.304
HSTOC_440	440	4.053	1.127	2.781	19.611	59.984	0.105	4.535	0.000	0.885	0.026	6.767	0.063
HSTOC_430	430	3.888	1.153	2.066	16.836	65.160	0.064	3.896	0.000	0.703	0.032	5.974	0.172
HSTOC_420	420	4.128	0.976	2.161	21.612	59.078	0.186	5.612	0.029	0.922	0.008	4.954	0.270
HSTOC_410	410	4.848	0.572	1.927	24.702	55.095	0.128	7.076	0.000	1.057	0.004	4.470	0.058
HSTOC_400	400	5.433	0.484	1.745	22.713	56.068	0.113	6.474	0.000	1.028	0.003	5.710	0.176
HSTOC_390	390	4.425	0.472	1.537	22.363	58.266	0.389	6.494	0.122	1.118	0.011	4.612	0.117
HSTOC_380	380	4.425	0.487	1.591	22.180	58.809	0.084	6.405	0.000	0.917	0.006	4.909	0.127
HSTOC_370	370	5.357	0.400	2.589	30.531	44.610	0.082	8.539	0.000	1.476	0.005	6.316	0.000
HSTOC_360	360	4.588	0.946	2.464	23.054	55.784	0.129	5.767	0.000	0.992	0.008	6.202	0.000
HSTOC_350	350	4.473	0.606	2.578	22.464	56.045	0.094	5.658	0.000	0.912	0.009	6.993	0.105
HSTOC_340	340	5.348	0.376	2.298	27.600	49.323	0.062	7.879	0.000	1.450	0.014	5.512	0.046
HSTOC_330	330	5.138	0.782	2.482	21.162	57.441	0.151	5.154	0.000	1.012	0.009	6.549	0.057
HSTOC_320	320	5.743	0.511	2.442	30.055	44.286	0.183	8.504	0.000	1.240	0.004	6.770	0.186
HSTOC_310	310	5.509	0.387	2.623	30.268	45.689	0.047	8.281	0.000	1.327	0.015	5.772	0.000
HSTOC_300	300	4.282	0.550	2.489	20.843	59.773	0.069	5.152	0.000	0.869	0.017	5.786	0.113
HSTOC_290	290	5.249	0.568	1.901	23.460	54.248	0.486	6.397	0.316	1.070	0.005	6.010	0.228
HSTOC_281	281	3.909	0.977	2.646	18.991	61.488	0.117	4.136	0.000	0.894	0.029	6.721	0.029
HSTOC_280	280	3.916	0.957	2.753	19.771	59.382	0.260	4.474	0.081	0.806	0.038	7.467	0.034
HSTOC_260	260	4.960	0.634	1.747	23.433	56.268	0.079	6.076	0.000	1.023	0.007	5.688	0.026
HSTOC_250	250	4.427	1.059	2.996	22.442	54.854	0.118	4.750	0.000	1.007	0.026	8.206	0.043
HSTOC_240	240	4.519	0.905	3.145	22.033	54.483	0.097	4.461	0.000	0.901	0.053	9.110	0.221
HSTOC_230	230	4.824	0.856	3.193	23.450	52.274	0.106	4.783	0.000	0.955	0.038	9.288	0.163
HSTOC_220	220	4.324	1.003	2.376	23.413	55.357	0.179	5.180	0.000	1.097	0.017	6.980	0.002
HSTOC_200	200	4.876	0.895	3.192	22.685	53.245	0.170	4.329	0.000	0.885	0.037	9.309	0.308
HSTOC_190	190	5.263	1.101	2.284	23.527	53.106	0.073	5.059	0.000	1.004	0.022	8.119	0.371
HSTOC_180	180	3.825	1.212	2.722	15.941	64.690	0.043	2.372	0.000	0.648	0.040	8.350	0.094
HSTOC_170	170	5.092	1.158	2.588	25.618	49.883	0.083	5.257	0.000	1.205	0.030	8.744	0.254
HSTOC_160	160	4.732	0.965	2.841	24.751	52.635	0.106	4.990	0.000	0.909	0.026	7.927	0.049
HSTOC_150	150	4.368	1.242	2.641	21.263	57.603	0.071	3.960	0.000	0.771	0.037	7.883	0.097
HSTOC_140	140	5.652	1.258	3.340	22.375	52.186	0.194	3.758	0.022	0.920	0.036	9.862	0.320
HSTOC_130	130	5.115	1.237	3.175	23.924	51.447	0.397	4.256	0.266	0.917	0.037	8.939	0.214
HSTOC_120	120	4.747	0.990	1.858	22.887	57.693	0.074	4.640	0.000	0.691	0.023	6.199	0.140
HSTOC_110	110	5.020	0.986	3.782	22.707	52.264	0.120	3.629	0.000	0.855	0.063	10.431	0.070
HSTOC_80	80	4.906	1.283	3.157	23.278	52.701	0.271	3.783	0.100	0.985	0.044	9.323	0.087
HSTOC_70	70	4.590	1.208	2.710	23.190	52.662	1.349	4.072	1.589	0.826	0.031	7.696	0.003
HSTOC_60	60	4.434	1.196	2.675	23.386	55.158	0.105	4.055	0.000	0.920	0.084	7.884	0.032
HSTOC_50	50	4.948	1.232	2.925	23.937	53.393	0.152	3.928	0.000	0.972	0.055	8.380	0.005
HSTOC_40	40	6.765	1.471	2.716	27.773	46.433	0.075	4.781	0.000	0.981	0.040	8.608	0.267
HSTOC_30	30	4.910	1.238	2.955	23.607	53.666	0.076	3.785	0.000	0.847	0.047	8.677	0.118
HSTOC_20	20	4.185	0.779	2.509	22.010	58.508	0.080	4.062	0.000	0.664	0.051	7.094	0.000
HSTOC_10	10	4.792	1.092	2.948	24.146	53.478	0.061	3.966	0.000	0.885	0.061	8.479	0.017
HSTOC_0	0	3.686	0.823	2.825	16.321	64.645	0.052	2.401	0.000	0.808	0.045	8.287	0.040
HSTOC-0	-1	4.440	1.119	2.204	22.902	52.897	1.928	3.938	2.620	0.921	0.023	6.888	0.032
HSTOC-10	-10	4.792	1.076	2.923	24.455	53.057	0.244	3.903	0.098	0.915	0.034	8.432	0.000
HSTOC-20	-20	4.802	1.274	2.813	24.119	53.778	0.092	3.518	0.000	0.863	0.032	8.568	0.070
HSTOC-30	-30	6.062	1.938	3.431	31.384	41.597	0.095	4.296	0.000	1.097	0.037	9.970	0.000
HSTOC-40	-40	4.995	1.265	3.070	23.502	52.740	0.110	3.294	0.000	0.959	0.085	9.804	0.089
HSTOC-50	-50	4.954	1.104	3.108	22.660	53.686	0.050	3.078	0.000	0.959	0.121	10.126	0.068
HSTOC-60	-60	6.469	2.167	2.010	31.799	45.429	0.139	5.106	0.000	1.026	0.026	5.745	0.000
HSTOC-70	-70	5.171	1.298	2.872	24.635	52.408	0.119	3.668	0.000	0.834	0.042	8.874	0.007
HSTOC-80	-80	4.811	1.121	2.845	23.680	54.193	0.092	3.605	0.000	0.879	0.066	8.599	0.023
HSTOC-90	-90	4.761	1.149	2.643	24.800	51.996	0.656	4.402	0.674	0.887	0.059	7.869	0.028
HSTOC-90-2	-90	4.842	1.181	2.698	24.322	53.496	0.222	3.916	0.000	0.995	0.039	8.169	0.038
HSTOC-100	-100	5.063	1.502	2.687	25.046	49.746	1.098	4.195	1.242	0.937	0.034	8.264	0.098
HSTOC-100-2	-100	4.317	1.179	2.574	23.338	55.659	0.093	4.060	0.000	0.990	0.047	7.650	0.012
HSTOC-120	-120	5.001	0.804	3.085	25.177	50.081	0.198	4.366	0.000	0.903	0.054	10.261	0.000
HSTOC-128	-130	5.299	0.974	2.654	27.896	47.730	0.083	5.306	0.000	0.978	0.040	8.973	0.000
HSTOC-140	-140	5.136	1.160	2.477	28.429	47.605	0.330	5.451	0.210	1.059	0.031	8.036	0.000
HSTOC-150	-150	5.976	1.107	3.042	25.809	48.529	0.096	4.351	0.000	1.063	0.072	9.881	0.000
HSTOC-160	-160	12.352	0.988	2.485	24.180	46.727	0.124	4.171	0.000	0.829	0.043	8.033	0.000
HSTOC-170	-170	5.118	1.041	3.173	25.574	49.517	0.078	4.129	0.000	0.951	0.067	10.277	0.000
HSTOC-180	-180	5.432	1.040	2.757	26.745	48.985	0.117	4.801	0.000	1.010	0.060	8.980	0.000
HSTOC-200	-200	4.649	0.671	2.399	25.828	52.176	0.104	5.444	0.000	0.996	0.014	7.652	0.000
HSTOC-210	-210	4.418	0.668	2.290	23.902	55.901	0.066	5.244	0.000	0.968	0.010	6.465	0.000
HSTOC-220	-220	4.511	0.579	2.601	24.127	53.661	0.090	5.186	0.000	0.918	0.023	8.234	0.000
HSTOC-270	-270	16.107	0.440	1.515	17.409	35.887	0.681	3.839	17.659	0.562	0.074	5.404	0.346
HSTOC-280	-280	4.804	1.518	2.779	25.752	51.414	0.117	3.976	0.000	1.172	0.032	8.330	0.017
HSTOC-290	-290	5.478	1.281	2.645	23.303	53.494	0.071	3.439	1.481	0.878	0.044	7.755	0.042
HSTOC-300	-300	8.834	1.916	1.987	17.450	51.594	0.077	3.216	7.799	0.724	0.043	5.833	0.439
	MAX	**18.797**	**2.167**	**6.603**	**31.799**	**65.160**	**1.928**	**8.539**	**17.659**	**1.476**	**0.396**	**10.431**	**0.615**
	MIN	**3.686**	**0.204**	**1.515**	**13.818**	**31.331**	**0.043**	**2.372**	**0.000**	**0.288**	**0.003**	**4.470**	**0.000**
	AVERAGE	**5.189**	**0.978**	**2.627**	**23.126**	**53.771**	**0.210**	**4.831**	**0.584**	**0.944**	**0.038**	**7.535**	**0.094**

Table A.2. Minor element concentration in parts per million (ppm).

		Cr	Cu	Zn	Rb	Sr	Y	Zr	Nb
Sample #	**Height (m)**	**ppm**	**ppm**	**ppm**	**ppm**	**ppm**	**ppm**	**ppm**	**ppm**
HSTOC_630	**630**	99	30	89	0	82	45	235	27
HSTOC_610	**610**	108	40	86	0	120	70	246	31
HSTOC_600	**600**	128	37	71	0	119	97	312	36
HSTOC_590	**590**	141	41	101	0	66	65	491	31
HSTOC_580	**580**	87	13	53	0	89	57	251	31
HSTOC_560	**560**	101	15	81	0	79	53	210	31
HSTOC_550	**550**	157	6	67	0	86	82	411	34
HSTOC_540	**540**	100	12	85	0	88	49	252	29
HSTOC_530	**530**	82	27	101	0	89	41	226	27
HSTOC_520	**520**	45	52	53	0	682	50	113	15
HSTOC_510	**510**	93	14	86	0	83	46	189	22
HSTOC_500	**500**	90	33	84	0	136	49	210	25
HSTOC_490	**490**	107	56	80	0	82	50	266	27
HSTOC_470	**470**	114	0	64	0	110	77	318	33
HSTOC_451	**451**	111	28	83	0	76	46	235	25
HSTOC_450	**450**	122	0	55	0	109	70	271	27
HSTOC_440	**440**	102	25	94	0	74	49	271	27
HSTOC_430	**430**	104	23	78	0	67	51	198	23
HSTOC_420	**420**	95	53	71	0	76	64	247	33
HSTOC_410	**410**	130	5	51	0	83	64	271	30
HSTOC_400	**400**	104	0	36	0	66	59	254	33
HSTOC_390	**390**	110	0	32	0	97	82	376	36
HSTOC_380	**380**	79	35	37	0	69	81	249	33
HSTOC_370	**370**	204	0	72	0	86	92	463	37
HSTOC_360	**360**	133	25	73	0	84	60	262	30
HSTOC_350	**350**	128	25	78	0	75	63	235	29
HSTOC_340	**340**	190	30	61	0	80	78	454	33
HSTOC_330	**330**	130	2	73	0	82	52	247	28
HSTOC_320	**320**	133	2	63	0	89	108	326	40
HSTOC_310	**310**	205	26	74	0	87	67	320	32
HSTOC_300	**300**	121	0	84	0	69	57	215	23
HSTOC_290	**290**	102	20	44	0	110	95	233	36
HSTOC_281	**281**	115	16	74	0	86	49	263	27
HSTOC_280	**280**	91	45	88	0	82	60	220	28
HSTOC_260	**260**	113	4	55	0	85	64	247	29
HSTOC_250	**250**	160	39	114	0	90	48	247	27
HSTOC_240	**240**	146	58	107	0	86	49	236	24
HSTOC_230	**230**	164	55	113	0	98	49	197	27
HSTOC_220	**220**	183	0	87	0	112	60	263	25
HSTOC_200	**200**	147	56	119	0	114	47	195	22
HSTOC_190	**190**	177	7	100	0	115	46	253	26
HSTOC_180	**180**	93	37	102	0	85	30	255	17
HSTOC_170	**170**	205	56	109	0	125	60	290	29
HSTOC_160	**160**	145	51	115	0	140	56	174	28
HSTOC_150	**150**	141	36	99	0	119	42	182	25
HSTOC_140	**140**	175	41	122	0	139	46	211	25
HSTOC_130	**130**	163	34	110	0	177	54	193	27
HSTOC_120	**120**	121	24	79	0	169	50	140	21
HSTOC_110	**110**	156	24	147	0	143	47	176	27
HSTOC_80	**80**	156	49	111	0	178	52	244	25
HSTOC_70	**70**	140	15	97	0	215	58	212	23
HSTOC_60	**60**	145	31	99	0	173	41	186	26
HSTOC_50	**50**	168	0	107	0	177	42	215	24
HSTOC_40	**40**	192	73	109	0	220	57	211	23
HSTOC_30	**30**	149	48	109	0	199	47	176	23
HSTOC_20	**20**	119	24	90	0	156	40	131	23
HSTOC_10	**10**	158	19	105	0	191	36	205	27
HSTOC_0	**0**	131	39	100	0	99	27	245	22
HSTOC-0	**-1**	160	30	99	0	222	60	306	21
HSTOC-10	**-10**	169	10	105	0	184	49	169	23
HSTOC-20	**-20**	158	46	103	0	183	37	156	23
HSTOC-30	**-30**	205	43	124	0	285	52	186	25
HSTOC-40	**-40**	152	66	114	0	190	53	265	23
HSTOC-50	**-50**	152	71	119	0	171	39	283	23
HSTOC-60	**-60**	186	18	80	0	312	52	161	24
HSTOC-70	**-70**	160	24	108	0	203	39	168	21
HSTOC-80	**-80**	166	99	110	0	196	45	216	25
HSTOC-90	**-90**	151	36	100	0	228	49	165	21
HSTOC-90-2	**-90**	174	38	102	0	196	67	227	26
HSTOC-100	**-100**	162	50	101	0	245	58	247	26
HSTOC-100-2	**-100**	157	33	103	0	171	49	272	25
HSTOC-120	**-120**	167	24	125	0	162	47	148	23
HSTOC-128	**-130**	185	4	110	0	169	34	143	21
HSTOC-140	**-140**	200	0	102	0	195	64	157	28
HSTOC-150	**-150**	191	0	113	0	179	47	189	25
HSTOC-160	**-160**	150	44	94	0	166	42	146	22
HSTOC-170	**-170**	157	48	122	0	178	40	191	21
HSTOC-180	**-180**	162	0	105	0	193	53	185	27
HSTOC-200	**-200**	154	19	100	0	108	55	218	24
HSTOC-210	**-210**	151	15	96	0	105	44	243	26
HSTOC-220	**-220**	154	44	108	0	106	56	210	27
HSTOC-270	**-270**	90	57	75	0	375	35	113	21
HSTOC-280	**-280**	186	58	101	0	294	41	186	27
HSTOC-290	**-290**	150	72	113	0	344	33	165	23
HSTOC-300	**-300**	87	48	98	0	402	44	175	24
	MAX	**205.000**	**99.000**	**147.000**	**0.000**	**682.000**	**108.000**	**491.000**	**40.000**
	MIN	**45.000**	**0.000**	**32.000**	**0.000**	**66.000**	**27.000**	**113.000**	**15.000**
	AVERAGE	**140.518**	**30.035**	**91.259**	**0.000**	**149.706**	**54.235**	**231.929**	**26.459**

Table A.3. Proxy ratios. Major elements are presented as oxide ratios (mass %), minor elements as elemental ratios (ppm).

Sample #	Height (m)	Si/Al	Zr/Nb	Zr/Al	Ti/Al	K/Al	K/Na
HSTOC_630	**630**	2.98171754	8.7037037	11.9343863	0.04570616	0.2430552	5.73860911
HSTOC_610	**610**	2.58202981	7.93548387	11.3176297	0.04559257	0.2534505	6.31766055
HSTOC_600	**600**	2.08801641	8.66666667	12.5507864	0.04404843	0.26421015	8.44215938
HSTOC_590	**590**	2.7449292	15.8387097	23.4883276	0.05558745	0.26674321	6.63809524
HSTOC_580	**580**	3.10499444	8.09677419	12.6883025	0.05080376	0.26190476	5.90763968
HSTOC_560	**560**	2.78431467	6.77419355	10.1601432	0.04523683	0.2405051	5.57912458
HSTOC_550	**550**	1.75020385	12.0882353	14.5708512	0.04871131	0.28588648	29.0071942
HSTOC_540	**540**	3.28449209	8.68965517	13.6452242	0.04651289	0.23619233	4.87919463
HSTOC_530	**530**	3.3002397	8.37037037	12.5982496	0.04108367	0.21918725	5.16010499
HSTOC_520	**520**	2.26740483	7.53333333	8.17773918	0.02084238	0.28006947	18.9705882
HSTOC_510	**510**	2.94653718	8.59090909	9.27015892	0.0382578	0.24033745	4.47897623
HSTOC_500	**500**	3.2307976	8.4	11.0631124	0.03882626	0.26035191	4.89306931
HSTOC_490	**490**	3.10086264	9.85185185	13.5776632	0.04558216	0.24169261	4.01952462
HSTOC_470	**470**	2.50318018	9.63636364	14.1440199	0.04425566	0.25054486	5.8738269
HSTOC_451	**451**	2.99240152	9.4	11.7476505	0.04234153	0.22920416	4.29307116
HSTOC_450	**450**	2.34255661	10.037037	11.4481244	0.04123015	0.26829165	7.20068027
HSTOC_440	**440**	3.05869155	10.037037	13.8187752	0.04512773	0.23124777	4.02395741
HSTOC_430	**430**	3.87027798	8.60869565	11.7605132	0.04175576	0.23140889	3.37901127
HSTOC_420	**420**	2.73357394	7.48484848	11.4288358	0.04266148	0.25967055	5.75
HSTOC_410	**410**	2.2303862	9.03333333	10.9707716	0.04279006	0.28645454	12.3706294
HSTOC_400	**400**	2.46854224	7.6969697	11.1830229	0.04526042	0.285035	13.3760331
HSTOC_390	**390**	2.60546438	10.4444444	16.8134866	0.04999329	0.29039038	13.7584746
HSTOC_380	**380**	2.65144274	7.54545455	11.22633	0.04134355	0.28877367	13.1519507
HSTOC_370	**370**	1.46113786	12.5135135	15.1649143	0.04834431	0.27968295	21.3475
HSTOC_360	**360**	2.41971025	8.73333333	11.3646222	0.04302941	0.25015182	6.0961945
HSTOC_350	**350**	2.4948807	8.10344828	10.4611823	0.04059829	0.25186966	9.33663366
HSTOC_340	**340**	1.78706522	13.7575758	16.4492754	0.05253623	0.28547101	20.9547872
HSTOC_330	**330**	2.71434647	8.82142857	11.6718647	0.04782157	0.24354976	6.59079284
HSTOC_320	**320**	1.47349859	8.15	10.8467809	0.04125769	0.28294793	16.6418787
HSTOC_310	**310**	1.50948196	10	10.5722215	0.04384168	0.27358927	21.3979328
HSTOC_300	**300**	2.86777335	9.34782609	10.3152137	0.04169265	0.24718131	9.36727273
HSTOC_290	**290**	2.31236147	6.47222222	9.93179881	0.04560955	0.2726769	11.2623239
HSTOC_281	**281**	3.23774419	9.74074074	13.8486652	0.04707493	0.21778737	4.23336745
HSTOC_280	**280**	3.00348996	7.85714286	11.1274088	0.04076678	0.22629103	4.67502612
HSTOC_260	**260**	2.40122904	8.51724138	10.5406905	0.04365638	0.25929245	9.58359621
HSTOC_250	**250**	2.44425631	9.14814815	11.0061492	0.04487122	0.21165672	4.48536355
HSTOC_240	**240**	2.47279081	9.83333333	10.7112059	0.04089321	0.20246902	4.92928177
HSTOC_230	**230**	2.22916844	7.2962963	8.40085288	0.04072495	0.20396588	5.58761682
HSTOC_220	**220**	2.36437022	10.52	11.2330756	0.04685431	0.22124461	5.16450648
HSTOC_200	**200**	2.34714569	8.86363636	8.59598854	0.03901256	0.19083095	4.83687151
HSTOC_190	**190**	2.25723637	9.73076923	10.7536022	0.04267437	0.21502954	4.59491371
HSTOC_180	**180**	4.0580892	15	15.996487	0.0406499	0.1487987	1.95709571
HSTOC_170	**170**	1.94718557	10	11.3201655	0.04703724	0.20520728	4.53972366
HSTOC_160	**160**	2.12658074	6.21428571	7.03001899	0.03672579	0.20160802	5.17098446
HSTOC_150	**150**	2.7090721	7.28	8.5594695	0.03626017	0.18623901	3.1884058
HSTOC_140	**140**	2.3323352	8.44	9.4301676	0.04111732	0.16795531	2.9872814
HSTOC_130	**130**	2.15043471	7.14814815	8.06721284	0.03832971	0.17789667	3.44058205
HSTOC_120	**120**	2.52077599	6.66666667	6.11700966	0.03019181	0.20273518	4.68686869
HSTOC_110	**110**	2.30166909	6.51851852	7.75091382	0.03765359	0.15981856	3.68052738
HSTOC_80	**80**	2.26398316	9.76	10.4820002	0.04231463	0.16251396	2.94855807
HSTOC_70	**70**	2.27089263	9.2173913	9.1418715	0.0356188	0.17559293	3.37086093
HSTOC_60	**60**	2.35859061	7.15384615	7.95347644	0.03933978	0.17339434	3.39046823
HSTOC_50	**50**	2.23056356	8.95833333	8.98191085	0.04060659	0.16409742	3.18831169
HSTOC_40	**40**	1.67187556	9.17391304	7.59730674	0.03532208	0.17214561	3.25016995
HSTOC_30	**30**	2.27330876	7.65217391	7.45541577	0.03587919	0.1603338	3.05735057
HSTOC_20	**20**	2.65824625	5.69565217	5.95184007	0.03016811	0.18455248	5.21437741
HSTOC_10	**10**	2.21477677	7.59259259	8.49001905	0.03665203	0.16425081	3.63186813
HSTOC_0	**0**	3.96084799	11.1363636	15.0113351	0.04950677	0.14711108	2.91737546
HSTOC-0	**-1**	2.30971094	14.5714286	13.3612785	0.04021483	0.17195005	3.51921358
HSTOC-10	**-10**	2.16957677	7.34782609	6.91065222	0.03741566	0.15959926	3.62732342
HSTOC-20	**-20**	2.22969443	6.7826087	6.46792985	0.03578092	0.14586011	2.76138148
HSTOC-30	**-30**	1.3254206	7.44	5.9265868	0.03495412	0.13688504	2.21671827
HSTOC-40	**-40**	2.24406433	11.5217391	11.2756361	0.04080504	0.14015828	2.60395257
HSTOC-50	**-50**	2.36919682	12.3043478	12.4889673	0.04232127	0.13583407	2.78804348
HSTOC-60	**-60**	1.42862983	6.70833333	5.0630523	0.03226517	0.16057109	2.35625288
HSTOC-70	**-70**	2.12737974	8	6.81956566	0.03385427	0.14889385	2.82588598
HSTOC-80	**-80**	2.28855574	8.64	9.12162162	0.03711993	0.15223818	3.21587868
HSTOC-90	**-90**	2.0966129	7.85714286	6.65322581	0.03576613	0.1775	3.83115753
HSTOC-90-2	**-90**	2.19949017	8.73076923	9.33311405	0.04090946	0.1610065	3.31583404
HSTOC-100	**-100**	1.98618542	9.5	9.86185419	0.03741116	0.16749182	2.79294274
HSTOC-100-2	**-100**	2.38490873	10.88	11.6548119	0.04242009	0.17396521	3.44359627
HSTOC-120	**-120**	1.98915677	6.43478261	5.87838106	0.03586607	0.17341224	5.43034826
HSTOC-128	**-130**	1.71099799	6.80952381	5.12618297	0.03505879	0.19020648	5.4476386
HSTOC-140	**-140**	1.67452249	5.60714286	5.52252981	0.03725069	0.19174083	4.69913793
HSTOC-150	**-150**	1.88031307	7.56	7.32302685	0.04118718	0.1685846	3.93044264
HSTOC-160	**-160**	1.93246485	6.63636364	6.03804797	0.03428453	0.17249793	4.22165992
HSTOC-170	**-170**	1.93622429	9.0952381	7.46852272	0.0371862	0.16145304	3.96637848
HSTOC-180	**-180**	1.8315573	6.85185185	6.91718078	0.03776407	0.17951019	4.61634615
HSTOC-200	**-200**	2.02013319	9.08333333	8.44045222	0.0385628	0.210779	8.11326379
HSTOC-210	**-210**	2.33875826	9.34615385	10.1665133	0.0404987	0.21939587	7.8502994
HSTOC-220	**-220**	2.22410577	7.77777778	8.70394164	0.03804866	0.21494591	8.95682211
HSTOC-270	**-270**	2.06140502	5.38095238	6.49089551	0.03228215	0.22051812	8.725
HSTOC-280	**-280**	1.99650513	6.88888889	7.22273998	0.04551103	0.15439578	2.61923584
HSTOC-290	**-290**	2.29558426	7.17391304	7.08063339	0.03767755	0.14757757	2.68462139
HSTOC-300	**-300**	2.95667622	7.29166667	10.0286533	0.04148997	0.18429799	1.67849687
	MAX	4.058	15.839	23.488	0.056	0.290	29.007
	MIN	1.325	5.381	5.063	0.021	0.136	1.678
	AVERAGE	2.394	8.738	10.180	0.041	0.210	6.319

Table A.4. Indices of alteration. Values are dimensionless.

Sample #	Height (m)	CIA	ICV	PIA	CIW	Terr. In.
HSTOC_630	**630**	77.7962151	0.87578081	94.7010611	95.9366626	26.211
HSTOC_610	**610**	76.7134891	0.80529996	93.7110187	95.2289157	29.108
HSTOC_600	**600**	76.6945361	0.73426123	94.8850962	96.1849487	33.300
HSTOC_590	**590**	76.5153734	0.81113662	94.8045522	96.1368653	28.482
HSTOC_580	**580**	76.5557276	0.74486907	94.3338933	95.7548768	26.845
HSTOC_560	**560**	77.9050922	0.83884078	94.628971	95.8673469	27.466
HSTOC_550	**550**	77.1758461	0.60821782	98.6386563	99.0240477	37.923
HSTOC_540	**540**	77.4144869	0.88293264	93.2196669	94.7368421	24.583
HSTOC_530	**530**	79.0055492	0.99230726	94.3740736	95.5523596	23.370
HSTOC_520	**520**	44.3966071	2.47503257	42.541909	50.7008146	18.180
HSTOC_510	**510**	77.2799636	0.75127526	93.4024846	94.9073643	27.162
HSTOC_500	**500**	73.0667077	0.79101254	87.2320596	90.2314969	25.671
HSTOC_490	**490**	76.8154015	0.78995457	92.6531121	94.3280851	26.397
HSTOC_470	**470**	76.283378	0.73775742	92.5468227	94.3078859	30.070
HSTOC_451	**451**	77.9670265	0.80118976	93.522169	94.9316629	26.504
HSTOC_450	**450**	76.5960201	0.66808888	95.1546448	96.4079172	31.881
HSTOC_440	**440**	77.5966446	0.82203865	93.0444979	94.5655319	26.158
HSTOC_430	**430**	76.9294037	0.82109765	91.8186334	93.5905275	22.588
HSTOC_420	**420**	76.5595664	0.6784194	94.0899735	95.5564398	29.122
HSTOC_410	**410**	76.3585781	0.61152943	96.8567975	97.7368046	33.407
HSTOC_400	**400**	76.5494928	0.67996302	97.1057825	97.9135233	30.699
HSTOC_390	**390**	75.9329055	0.64240039	96.3919091	97.4125539	30.447
HSTOC_380	**380**	76.2933407	0.64540126	97.0052884	97.8515022	29.989
HSTOC_370	**370**	77.3524196	0.63296322	98.2136477	98.706799	40.946
HSTOC_360	**360**	77.4481809	0.71046239	94.8116053	96.0583333	30.759
HSTOC_350	**350**	78.1954887	0.74590456	96.5196416	97.373212	29.640
HSTOC_340	**340**	76.9767118	0.6351087	98.129074	98.6559908	37.305
HSTOC_330	**330**	78.0943243	0.75550515	95.3424658	96.4363835	28.110
HSTOC_320	**320**	76.9260302	0.64784562	97.6838002	98.3282078	40.310
HSTOC_310	**310**	77.7378262	0.60806793	98.2703138	98.7375632	40.263
HSTOC_300	**300**	78.5194952	0.71309312	96.613509	97.4290656	27.414
HSTOC_290	**290**	76.315019	0.69339301	95.0743857	96.3687151	31.495
HSTOC_281	**281**	78.7877531	0.8110684	93.828954	95.1071715	24.998
HSTOC_280	**280**	78.1987897	0.83839968	93.6455464	95.0117738	26.008
HSTOC_260	**260**	77.739442	0.647591	96.4760158	97.3656875	31.166
HSTOC_250	**250**	79.437896	0.80402816	94.3523012	95.4938088	29.258
HSTOC_240	**240**	80.4153436	0.8430536	95.1020187	96.0545819	28.300
HSTOC_230	**230**	80.6146653	0.8150533	95.615428	96.4782358	30.044
HSTOC_220	**220**	79.1086633	0.71127152	94.7858183	95.892038	30.693
HSTOC_200	**200**	81.2820237	0.82199691	95.3508909	96.2044105	28.794
HSTOC_190	**190**	79.2501768	0.74760913	94.3737544	95.5294786	30.691
HSTOC_180	**180**	81.6440461	0.9625494	91.8002841	92.9341806	20.173
HSTOC_170	**170**	79.973777	0.74096339	94.618709	95.6752316	33.238
HSTOC_160	**160**	80.6063961	0.71342572	95.3440124	96.2474724	31.615
HSTOC_150	**150**	80.3438504	0.77759488	93.302777	94.4812264	27.236
HSTOC_140	**140**	81.6218582	0.85792179	93.5668694	94.5888818	28.311
HSTOC_130	**130**	80.5983223	0.78695034	92.900666	94.0889606	30.334
HSTOC_120	**120**	80.2573903	0.62922183	94.8536674	95.8537505	29.208
HSTOC_110	**110**	83.10885	0.86959968	95.0857257	95.8384333	28.177
HSTOC_80	**80**	81.8379975	0.80225964	93.3758023	94.3919549	29.329
HSTOC_70	**70**	77.1482751	0.78188875	87.2370522	89.2369262	29.296
HSTOC_60	**60**	81.6635821	0.71897717	94.1735275	95.1346514	29.557
HSTOC_50	**50**	82.266213	0.73075156	94.1998964	95.1050896	30.069
HSTOC_40	**40**	81.6252755	0.66960717	93.9868373	94.9699084	35.006
HSTOC_30	**30**	82.4554663	0.7433812	94.1215575	95.0171061	29.477
HSTOC_20	**20**	81.9708763	0.68873239	95.8402307	96.5816841	27.515
HSTOC_10	**10**	82.6804547	0.72190011	94.8664912	95.6731912	30.089
HSTOC_0	**0**	83.5047327	0.9306415	94.4176898	95.1994867	20.353
HSTOC-0	**-1**	74.8945355	0.7734259	83.5308109	85.9652415	28.880
HSTOC-10	**-10**	82.8084789	0.710734	94.5963362	95.4192516	30.349
HSTOC-20	**-20**	83.4249939	0.70765786	94.176	94.9828693	29.774
HSTOC-30	**-30**	83.4281461	0.66177033	93.3232275	94.1840226	38.715
HSTOC-40	**-40**	83.7532518	0.78618841	94.1088809	94.8923971	29.020
HSTOC-50	**-50**	84.4199389	0.81624007	94.6630571	95.3543175	27.801
HSTOC-60	**-60**	81.385647	0.50567628	92.4913375	93.6200907	40.098
HSTOC-70	**-70**	83.2235397	0.71394358	94.1702223	94.9947943	30.435
HSTOC-80	**-80**	83.3626699	0.72276182	94.7112663	95.480021	29.285
HSTOC-90	**-90**	79.9355359	0.71302419	91.7960488	93.1525373	31.238
HSTOC-90-2	**-90**	82.6744621	0.69887345	94.5291147	95.3691723	30.414
HSTOC-100	**-100**	78.3054557	0.75305438	88.3704175	90.1259446	31.680
HSTOC-100-2	**-100**	81.6670749	0.70700146	94.2366916	95.1910919	29.567
HSTOC-120	**-120**	82.9637196	0.77344402	96.2803609	96.9054309	31.250
HSTOC-128	**-130**	81.6245318	0.67841268	95.8665761	96.6262556	35.154
HSTOC-140	**-140**	80.6496454	0.64807063	94.3732545	95.4025303	36.099
HSTOC-150	**-150**	82.5438961	0.75617033	95.0941724	95.8872046	32.330
HSTOC-160	**-160**	82.4158969	0.6844086	95.2945659	96.0743802	30.168
HSTOC-170	**-170**	83.1837106	0.76788926	95.3704527	96.0886718	31.695
HSTOC-180	**-180**	82.0751243	0.69725182	95.4751131	96.2569732	33.596
HSTOC-200	**-200**	80.8565257	0.66501471	96.8131085	97.467829	32.939
HSTOC-210	**-210**	80.1703897	0.65454774	96.5435165	97.2812373	30.782
HSTOC-220	**-220**	80.7139034	0.72702781	97.0338115	97.6564397	30.810
HSTOC-270	**-270**	44.2447963	1.69412373	42.8494742	49.028388	22.250
HSTOC-280	**-280**	82.4169494	0.69148027	93.4833004	94.4334433	32.418
HSTOC-290	**-290**	78.9825108	0.75196327	87.7928047	89.4034145	28.901
HSTOC-300	**-300**	57.437214	1.23312321	59.4346319	64.2370698	23.306
	MAX	84.420	2.475	98.639	99.024	40.946
	MIN	44.245	0.506	42.542	49.028	18.180
	AVERAGE	78.514	0.779	92.717	93.983	29.879

Equation A.1. Example calculation of molar proportion of Al in Al_2O_3 from mass percent.

$$moles\ Al = \frac{wt\ \%\ Al_2O_3}{(molar\ mass\ Al * 2) + (molar\ mass\ O * 3)}$$

$$moles\ Al = \frac{19.691}{(26.982 * 2) + (15.999 * 3)}$$

$$moles\ Al = 0.193$$

wt% Al measured by XRF – 19.691%

calculated molar proportion Al – 19.3%

the difference of 0.391% was considered insignificant and therefore measured wt% XRF data were used for data analysis and interpretation. Also, trends in the data based on measured XRF or calculated molar proportions showed little difference.